การศึกษาการวิบัติเฉพาะที่ของดินทรายด้วยคลื่นแรงเฉือน

นายพูลพงษ์ พงษ์วิทยภานุ

วิทยานิพนธ์นี้เป็นส่วนหนึ่งของการศึกษาตามหลักสูตรปริญญาวิศวกรรมศาสตรดุษฎีบัณฑิต
สาขาวิชาวิศวกรรมโยธา ภาควิชาวิศวกรรมโยธา
คณะวิศวกรรมศาสตร์ จุฬาลงกรณ์มหาวิทยาลัย
ปีการศึกษา 2553
ลิขสิทธิ์ของจุฬาลงกรณ์มหาวิทยาลัย

STUDY OF LOCALIZATION IN SANDY SOIL
USING SHEAR WAVE LOGGING

Mr. Pulpong Pongvithayapanu

A Dissertation Submitted in Partial Fulfillment of the Requirements
for the Degree of Doctor of Philosophy Program in Civil Engineering
Department of Civil Engineering
Faculty of Engineering
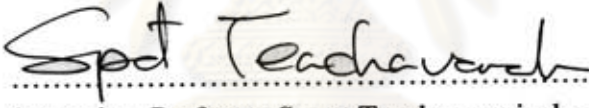Chulalongkorn University
Academic year 2010

Thesis Title	STUDY OF LOCALIZATION IN SANDY SOIL USING SHEAR WAVE LOGGING
By	Mr. Pulpong Pongvithayapanu
Field of Study	Civil Engineering
Thesis Advisor	Associate Professor Supot Teachavorasinskun, D. Eng.

Accepted by the Faculty of Engineering, Chulalongkorn University in Partial Fulfillment of the Requirements for the Doctoral Degree

.... Dean of the Faculty of Engineering

(Associate Professor Boonsom Lerdhirunwong, Dr. Ing.)
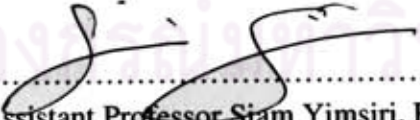
THESIS COMMITTEE

.... Chairman

(Assistant Professor Thavee Thanacharoengit, Dr. Ing.)

.... Thesis Advisor

(Associate Professor Supot Teachavorasinskun, D. Eng.)

.... Examiner

(Associate Professor Tirawat Boonyatee, D. Eng.)

.... Examiner

(Associate Professor Suched Likitlersuang, D. Phil.)

.... External Examiner

(Assistant Professor Siam Yimsiri, Ph. D.)

พูลพงษ์ พงษ์วิทยภานุ : การศึกษาการวิบัติเฉพาะที่ของดินทรายด้วยคลื่นแรงเฉือน.
(STUDY OF LOCALIZATION IN SANDY SOIL BY SHEAR WAVE LOGGING)
อ. ที่ปรึกษาวิทยานิพนธ์หลัก : รศ.ดร. สุพจน์ เตชวรสินสกุล, 140 หน้า.

การศึกษาการเกิดปรากฏการณ์ Localization ในมวลดินเป็นหัวข้อหนึ่งที่สำคัญใน
งานวิจัยทางวิศวกรรมปฐพีมากว่า 50 ปี แม้ว่าการศึกษาวิจัยโดยอาศัยทฤษฎีและการจำลองทาง
คณิตศาสตร์จะสามารถทำให้ทราบถึงพฤติกรรม Localization ได้ดีในระดับหนึ่ง แต่เนื่องจาก
ความไม่ต่อเนื่องของมวลดินภายในบริเวณดังกล่าวนั้นมีความซับซ้อนมาก การศึกษาจากการ
ทดสอบดินในห้องปฏิบัติการจะทำให้รู้ถึงพฤติกรรมของความไม่ต่อเนื่องดังกล่าวได้มากยิ่งขึ้น
โดยอาศัยเครื่องมือทดสอบแบบดั้งเดิมและที่พัฒนาใหม่ เช่น การใช้รังสีแกมม่า การใช้
ภาพตัดขวางจากรังสีเอ็กซเรย์ และการวิเคราะห์ภาพถ่าย เป็นต้น แต่การทดสอบโดยใช้
เครื่องมือดังกล่าว ผู้ทดสอบจำเป็นต้องมีความเชี่ยวชาญและประสบการณ์ด้านเทคนิคในการ
ติดตั้งเครื่องมือ การใช้เครื่องมือ และการวิเคราะห์ผล ซึ่งในปัจจุบันการทดสอบโดยใช้ Bender
Element ได้รับความนิยมอย่างแพร่หลายเนื่องจากความง่ายในการทดสอบและราคาไม่แพง
การทดสอบโดยใช้ Bender Element นี้ส่วนใหญ่ใช้ในการวัดค่าความเร็วคลื่นแรงเฉือนเพื่อใช้
คำนวณหาค่าโมดูลัสแรงเฉือนที่ระดับความเครียดต่ำ โดยตัวแปรหลายตัวที่มีผลกระทบต่อการ
เคลื่อนที่ของคลื่นแรงเฉือนผ่านตัวอย่างดินนี้มีผลกระทบต่อพฤติกรรมของการเกิด
Localization ด้วยเช่นเดียวกัน เช่น ค่าอัตราส่วนช่องว่างและสภาวะความเค้น เป็นต้น
ในงานวิจัยฉบับนี้จึงได้ทำการทดสอบตัวอย่างดินทรายท้องถิ่นและทรายซิลิกาใน
เครื่องทดสอบแรงอัดสามแกนที่มีการติดตั้งอุปกรณ์ตัว Bender Element ไว้เพื่อทำการตรวจวัด
คลื่นแรงเฉือนระหว่างการกดทดสอบตัวอย่าง เพื่อใช้ศึกษาพฤติกรรมในเกิด Localization ใน
ดิน โดยผลการทดสอบพบว่าเทคนิคการใช้คลื่นแรงเฉือนเพื่อดูพฤติกรรมการเกิดปรากฏการณ์
Localization นั้นสามารถอธิบายกระบวนการเกิดได้ดีในระดับหนึ่ง โดยความเร็วของคลื่นแรง
เฉือนจะเริ่มลดลงจากค่าสูงสุด ณ ตำแหน่งความเครียดที่ประมาณ 0.5 – 3% ขึ้นอยู่กับสภาวะ
ความเค้นและค่าความหนาแน่นเริ่มต้นของตัวอย่างดินนั้น การลดลงของค่าความเร็วคลื่นแรง
เฉือนนี้อธิบายได้ว่าเป็นจุดเริ่มต้นของการเกิดปรากฏการณ์ Localization ขึ้นในมวลดิน

ภาควิชา .....วิศวกรรมโยธา.... ลายมือชื่อนิสิต ....
สาขาวิชา....วิศวกรรมโยธา.... ลายมือชื่อ อ.ที่ปรึกษาวิทยานิพนธ์หลัก ....
ปีการศึกษา ....2553...........

4971821521 : MAJOR CIVIL ENGINEERING

KEYWORDS : LOCALIZATION / BENDER ELEMENT / SHEAR WAVE

PULPONG PONGVITHAYAPANU : STUDY OF LOCALIZATION IN SANDY SOIL USING SHEAR WAVE LOGGING. THESIS ADVISOR : ASSOCIATE PROFESSOR SUPOT TEACHAVORASINSKUN, D.ENG, 140 pp.
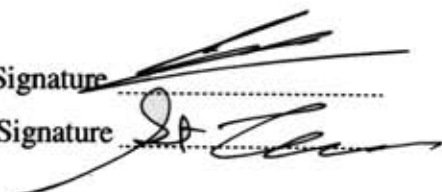
Strain localization phenomenon in soils has been one of the main research topics in geotechnical engineering for more than 50 years ago. Though investigations by theoretical and numerical studies can expose some of the strain localization characteristics but are impeded because of the complexity inside that localized zones. On the other hand, the experimental studies can obviously investigate that particular behavior in more details. Both conventional and new apparatuses, i.e. Gamma-ray, X-ray Computed Tomography and Digital Image Analysis, have been adopted in the strain localization analyses. However, those techniques require technical proficiency and experience in the installation, operation and result interpretation. The bender element test nowadays is becoming quite popular in geotechnical engineering because of its simplicity, relatively low cost and nondestructive test. A pair of bender elements has been extensively used to measure shear wave velocity for the determination of small strain shear modulus inside the soil sample. This shear wave propagation throughout the soil specimen influences in the same way by several of the same factors, e.g. void ratio and state of stress, compared to localization mechanism.

A series of compression triaxial tests implemented by bender element installation was performed to investigate the occurrence of strain localization in sand of various types, i.e. local and Silica sand. The results showed that this shear wave propagation technique can describe to some extent some characteristics of localization mechanism. The shear wave velocity tends to decrease from its maximum value at a certain strain level, i.e. 0.5 - 3% of global axial strain, depending on the state of stress as well as the initial packing condition of the sample. This diminution of shear wave velocity is the initiation of soil non-uniformity deformation or the onset of strain localization inside the sand specimen.

Department : ___Civil Engineering___   Student's Signature _____

Field of Study : ___Civil Engineering___   Advisor's Signature _____

Academic Year : _____2010_____

ACKNOWLEDGEMENTS

CONTENTS

LIST OF TABLES

ศูนย์วิทยทรัพยากร

จุฬาลงกรณ์มหาวิทยาลัย

LIST OF FIGURES

Page

LIST OF SYMBOLS

V_s shear wave velocity

σ_c failure stress in compression

σ_t failure stress in tension

τ_{ult} failure stress in pure shear

τ_f shear strength per unit area

c cohesion

σ_n normal stress

ϕ angle of shearing resistance

σ_c normal stress at failure

τ_c shear stress at failure

θ_c angle between the major principal stress direction and shear band

θ_R inclination angle between shear band and the major principal strain increment direction

θ_A inclination angle of the shear bands which include the effects of friction angle and angle of dilatancy.

σ_1 major principle stress

σ_3 minor principle stress

$d\varepsilon_1$ major principal strain increment

$d\varepsilon_3$ minor principal strain increment

ψ angle of dilatancy

d_{50} mean grain size

U uniformity coefficient

ρ_d dry density

γ_d^{max} maximum specific weight

γ_d^{min} minimum specific weight

e void ratio

e_{min} minimum void ratio

e_{max} maximum void ratio

D_r relative density

G_s specific gravity

t/s' stress ratio

ε_v volumetric strain

ε_1 axial strain

ε_a global axial strain

G_{max} small strain stiffness

L, L_{tr} tip-to-tip distance between transmitter and receiver of bender element

t travel time of the shear wave from transmitter to receiver

t_0 first time of arrival

t_{pp} time between first peak to peak

t_{cc}, τ time shift

$CC_{yx}(t)$ cross-correlation function

T total duration of the time record

dt change in time-of-flight in seconds

$d\theta$ change in phase angle in degrees

f frequency of the driving wave in Hertz

L_{tt} wave path length

λ wavelength

H/D slenderness ratio

σ'_c confining pressure

q' deviator stress

σ'_1 effective stress in the direction of shear wave propagation

σ'_3 effective stress in the direction of particle motion

σ'_{mean} mean state of stress

σ'_0 isotropic loading

$\alpha,\ \beta$ parameters include contact effects, void ratio, coordination number,

        fabric change and the loading history

A effect of grain properties

$F(e)$ influence of packing properties

C_n coordination number

$\Omega,\ \Theta$ void ratio of the arrangement at constant fabric as well as the packing property

$\theta,\ \delta,\ \zeta,\ \psi$ contact effect and the influence of fabric change

Ψ effect of void ratio

φ exponent parameter reflecting the contact behavior under anisotropic loading

q'/p' principal stress ratio

CHAPTER I

Introduction

1.1 Introduction

The occurrence of strain localization in soils is one of the significant matters in geotechnical engineering problems. This phenomenon leads to an instability within the soil mass. When the strain localization or zone of shear bands occurs, the discontinuity within soil mass will present and result in the change in the physical properties of soil, e.g. the low density of soil particles and relatively high strain within the zone of shear band. Furthermore, the load carrying capacity of soil is slightly decreased after failure because of this emergence of shear band zones. Although strain localization has been observed for a long time both by theoretical studies and laboratory experiments, it is only during the last 20 – 40 years that many scholars have conducted the in-situ and laboratory tests as well as the numerical studies to investigate strain localization in soils, especially in sand. Those studies started from the seventies by Roscoe (1970), Arthur *et al.* (1977) and Vardoulakis *et al.* (1978). These investigates had provided valuable details and innovate concepts concerning shear band characteristics in sand. Later, various theoretical, numerical and experimental studies have been continuously carried out. The results of these systematic studies reveal that the principal characteristics of strain localization, i.e. thickness and orientation of shear bands, and the strain level at which a shear band forms, depend primarily on a number of factors including the initial state of the material (mean effective stress and void ratio), grain particle characteristic (grain size, uniformity, contact surface, etc.) and size and slenderness of the specimen. Moreover, among the experimental studies of these past works, e.g. Lee (1970) and Peter *et al.* (1988), they indicated that strain localization can be visually observed through shear bands under plane strain than under conventional triaxial compression. Hence, it can also be noted that shear band formation is highly dependent on loading condition or boundary condition.

To obviously explore strain localization characteristics, additionally from plane strain and conventional triaxial test devices, complicated instrumentation techniques have been used, for example, Gamma-rays, Stereophotogrammetry, X-ray Computed Tomography, Digital Image Analysis (DIA) and Digital Image Correlation (DIC). These techniques can used to explore the strain field pattern inside the specimen during the entire test. This capacity of the modern apparatuses, as a result, can characterized the crucial features of strain localization, i.e. the pattern of shear band formation, time and evolution of strain localization.

Roesler (1979) reported that the shear wave velocity (V_s) of sand depends on the stresses in the direction of wave propagation and particle motion, and that the velocity is independent of the stress normal to the plane of shear. Many studies on shear wave velocity and determination of small strain shear modulus of soils from various researchers, e.g. Stokoe *et al*. (1995) and Bellotti *et al.* (1996), also confirm Roesler's finding. In addition to the confining stresses, the shear wave velocity also depends on the void ratio. Void ratio functions are proposed to express the effect of void ratio dependence on shear wave velocity and shear modulus (Hardin and Drnevich, 1972 and Iwasaki *et al.* (1978). Moreover, stress history, degree of saturation, grain characteristics, frequency, aging effects and soil structure also affect shear wave velocity (Richart *et al*., 1970). A few studies in the past also indicated a sudden drop (deviation from the general accepted elastic shear modulus path) of the elastic shear modulus before and after the failure of clayey soils (Teachavorasinskun and Akkarakun, 2004 and Teachavorasinskun and Amornwithayalax, 2002). However, these phenomena, though clearly observed in the laboratory tests and theoretically confirmed by the theory of elastic wave propagation, have not been investigated in details.

As mentioned above, from the literature of strain localization and shear wave propagation in soil, we may imply that the strain localization and shear wave velocity (V_s) of soils primarily influence by the same dominant parameters; e.g. void ratio, confining pressure and grain characteristics. A brief introduction to this study is that the propagation of shear wave through the body of localized sandy sample will be

adopted to characterize the mechanism of shear band formation using the laboratory tests; i.e. conventional triaxial test. The main assumptions of this method are that;

1) There must exist clear shear bands (rupture surfaces) after peak stress level and the thickness of shear bands is uniform,

2) The densities of the intact and localized zones should be distinctly different and

3) Since the velocity of shear wave is dependent on both void ratio and stress state, it is therefore necessary to carry out a detailed investigation on the stress state and void ratio dependency characteristics of shear wave velocity.

1.2 Objective of the Study

1) To observe the shear wave propagation inside the sandy soil under isotropic consolidation and triaxial compression test

2) To investigate the mechanism and the evolution of strain localization of sandy soil sample under triaxial compression test using shear wave propagation technique and Digital Image Analysis (DIA)

1.3 Scope of the Study

To clarify the problems, a literature study will be conducted including several topics. These topics consist of;

1) The ideas of strain localization and shear band of granular materials

2) The factors affecting strain localization and shear band

3) The shear wave propagation technique for geotechnical applications

4) The factors affecting shear wave propagation inside granular materials

5) The bender element testing within triaxial apparatus

After the systematic review, the experimental study to examine the correlation between shear wave velocity, void ratio and stress state of sandy soil sample by the modified triaxial apparatus will be performed. The correlation between shear wave velocity, void ratio and stress state should be established and the identification as well as the evolution of strain localization within the soil mass should also be evaluated.

CHAPTER II

Literature Review

The present localization theory is established and developed from the Mohr's strength theory published in the year 1900. This original theory of stress analysis has given a fundamental and crucial knowledge to various disciplines of engineers particularly in civil engineering. Mohr's theory describes the stress at a point by using the graphical illustration of circle. The drawing of this stress circle provide a clear understanding of stress conditions at failure. To explain the stress failure criterion, Mohr used the example of cast iron which was tested to failure in compression (σ_c), in tension (σ_t) and in pure shear (τ_{ult}). He then drew the linear lines contacting the compression and tension circles. These lines are extensively called "Failure envelopes" as illustrates in Figure 2.1.
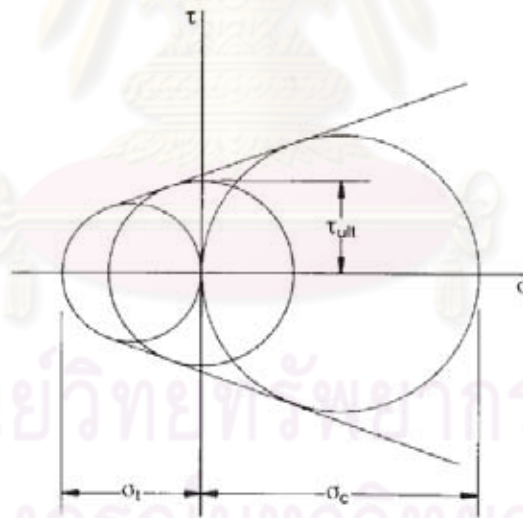
Figure 2.1 Mohr's stress circles and strength envelopes for cast iron (Parry, 1995)

Previously in 1773, Coulomb proposed various topics relating the strength properties of materials, i.e beams, earth pressure and shear strength of soils. A well-known equation concerning a shear resistance of soils was presented;

$$\tau_f = c + \sigma_n tan\phi \tag{2.1}$$

where τ_f is the shear strength per unit area; c is the soil cohesion; σ_n is the normal stress on the shear plane and ϕ is the shear resistance angle.

Although there are some differences of idea between Mohr and Coulomb failure criterion, however, the important conclusion is identical. Namely, both of original theories implied that the shear resistance of the materials will depend on its state of stress. This stress-dependent criterion is widely known as the "*Mohr – Coulomb failure criterion*". The stress analysis by the use of Mohr stress circle and the Mohr – Coulomb failure criterion can reveal an explicit view of stress conditions at failure in geotechnical engineering.

In the classical paper of Mohr in 1900, he finally summarized his findings by pointing to the following general property of localized deformation: " ... *The deformations observed in a homogeneous body after the elasticity limit [is reached] are not confined in the smallest domains of the body. They consist more or less in the fact that parts of the body of finite dimensions, displace with respect to each other on two sets of slip bands ...* " (Vardoulakis and Sulem, 1995).

2.1 Strain Localization in Granular Soils

In granular materials, when the applied load is high enough, the occurrence of strain localization will present. The inter-particle slip and rotation between particle surfaces will be generated which turn to strong dilatancy as well as high deformations of the material inside the localized zone. Because of the stability and deformation of the soil mass will be primarily influenced by the development of strain localization, therefore a research on strain localization problem in soils has been carried out in the field of geotechnical engineering for many years ago by theoretical, numerical as well as experimental works. As mentioned above, the basic concept of strain localization in sand has been evolved from a theoretical approach, i.e. Mohr - Coulomb criteria, then following by a numerical approach. In addition to the main developments of soil modeling in strain localization by theoretical and numerical approaches, various kinds of experimental studies have been attempted to clarify the crucial behaviors of strain

localization. These investigations have provided physical features, i.e. shear band orientation and thickness, as well as localization initiation time and evolution to the geotechnical engineers. Those research results also evidenced some influences of parameters affecting the nature of strain localization in sand, for example, an initial stress state, initial packing condition, grain characteristics of soil particle, specimen geometry and property of microstructure. The literature reviews of these investigations are as follows:

2.1.1 Theoretical and numerical approach

The theory of strain localization is an original work of Mohr to analyze strain localization in materials. It was applied to investigate the orientation of shear bands, i.e. inclination angle of shear band zone, within various types of materials, including elasto-plastic soils and rocks. A number of theories by many scholars have been proposed to make clear understanding about strain localization phenomena. Those theories can be liberalized as follows:

2.1.1.1 Theory of shear band inclination

Currently, There are two well-known theories in soil mechanics that can explain the physical property of strain localization, e.g. inclination of shear band. Those are Mohr - Coulomb theory and Roscoe theory.

- Mohr - Coulomb Theory

The Mohr - Coulomb theory, which is merely based on engineering static, can explicitly describe the orientation of the shear band in terms of inclination angle. This inclination angle of the shear band primarily depends on the mobilized frictional angle between grain particles. The Mohr - Coulomb theory states that the shear band plane of strain localization will parallel to the surface which passes through the failure stresses (σ_c, τ_c) on the Mohr - Coulomb failure envelope. The calculation of this classical theory can be displayed as in equation 2.2

$$\theta_c = \frac{\pi}{4} - \frac{\phi}{2} \qquad (2.2)$$

where θ_c is the angle between the major principal stress direction and shear band, ϕ is the value of the mobilized friction angle at failure. By definition, the mobilized friction angle, ϕ, is calculated from the major and minor principle stress, σ_1 and σ_3

$$sin\phi = \frac{\sigma_1 - \sigma_3}{\sigma_1 + \sigma_3} \qquad (2.3)$$

Figure 2.2 shows the inclination angle (θ_c) between the idealized plane of shear band and the plane of major principal stress. In should be noted that this concept excludes some parameters affecting strain localization mechanisms.
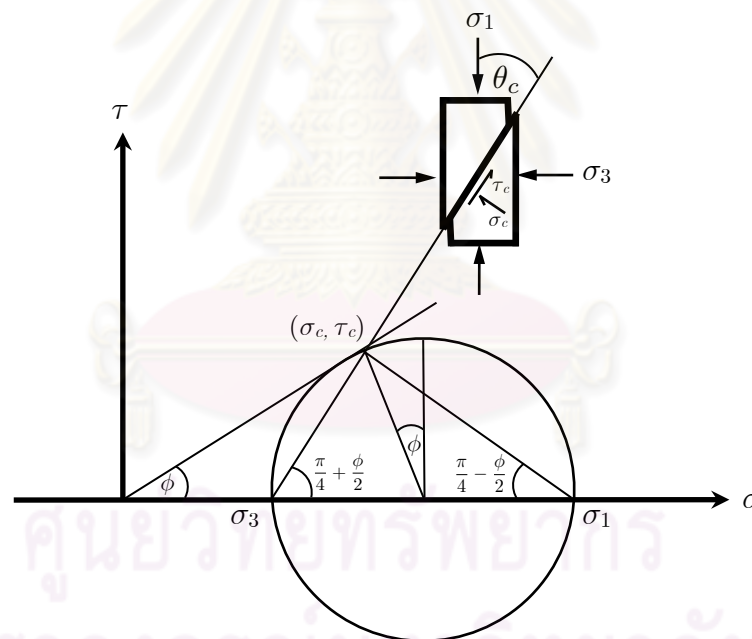
Figure 2.2 Mohr - Coulomb solution to shear orientation

- Roscoe Theory

Roscoe (1970), unlike Mohr's theory, proposed the strain circle on failure. He related the inclination angle of shear band with the angle of dilatancy as well as the major and minor principal strain increments. The expressions of these

correlations as well as the graphical explanation of Roscoe's finding can be displayed in equations 2.4, 2.5 and Fig. 2.3, respectively.

$$\theta_R = \frac{\pi}{4} - \frac{\psi}{2} \tag{2.4}$$

where θ_R is the inclination angle between the idealized shear band plane and the major principal strain increment direction, $d\varepsilon_1$, and ψ is the angle of dilatancy at failure. By definition, the dilatancy angle, ψ, is obtained from the major and minor principal strain increments $d\varepsilon_1$ and $d\varepsilon_3$:

$$sin\psi = -\frac{d\varepsilon_1 + d\varepsilon_3}{d\varepsilon_1 - d\varepsilon_3} \tag{2.5}$$
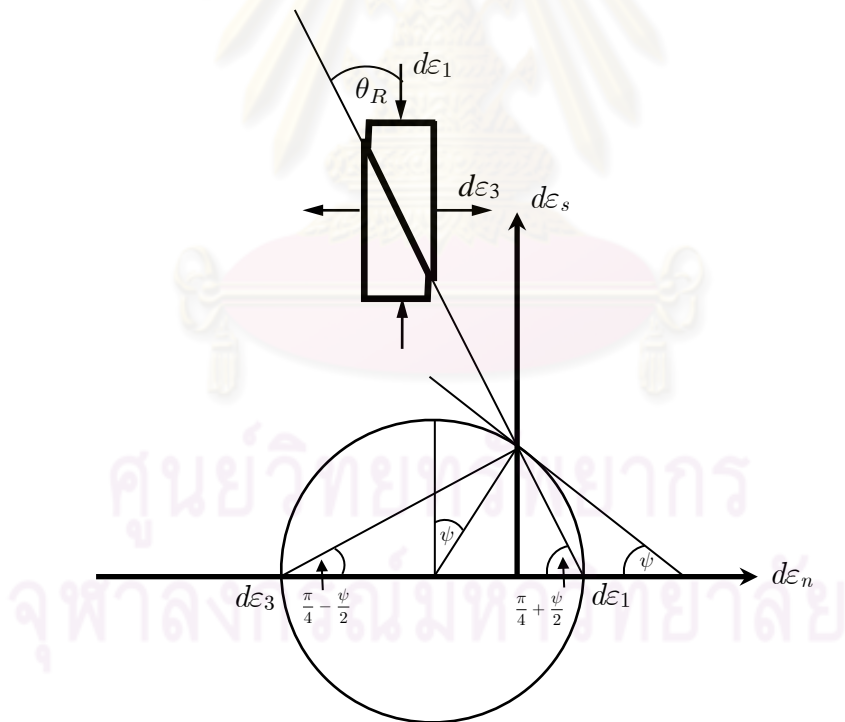
Figure 2.3 Roscoe solution to shear band orientation

- Arthur findings

Arthur *et al.* (1977) proposed the empirical equation concerning both parameters mentioned by Mohr and Roscoe, i.e. frictional angle and angle of dilatancy to comprehensibly explain the angle of inclination of shear band. His expression is as follows;

$$\theta_A = \frac{\pi}{4} - \frac{\phi}{4} - \frac{\psi}{4} \qquad (2.6)$$

where θ_A is the inclination angle of the shear bands which include the effects of friction angle and angle of dilatancy. This equation was verified by theoretical and experimental study by Vermeer (1982) and Alshibli (1995), respectively.

Bardet (1990) compared experimental results of shear band inclination angle of various researchers, i.e. Arthur *et al.* (1977), Vardoulakis (1980) and Desrues *et al.* (1985), with the theoretical calculation of Mohr - Coulomb and Roscoe theory. He inferred that Mohr - Coulomb estimation underestimates the shear band orientation and this orientation does not vary in function of ψ as stipulated by the Roscoe theory. In contrast to the Mohr - Coulomb theory, Arthur's equation overestimates the shear band inclination angle. The use of the local dilatancy, ψ, established by Desrues *et al.* (1985) by using stereophotogrammetric technique, instead of the global dilatancy, ψ, slightly improves the prediction of shear band inclination angle. Finally he concluded that the theory of Arthur *et al.* (1977) and Mohr - Coulomb give an upper and lower bound value, respectively, for the shear band inclination angles which are more accurate than the prediction from the Roscoe theory. However, neither Mohr - Coulomb nor Arthur's equation accounts for the orientation of shear bands in all circumstances. It is therefore necessary to utilize a modern theory of strain localization to describe the emergence, orientation and mechanism of strain localization.

2.1.1.2 Theory of strain localization

- Theory of bifurcation

The theory of bifurcation has been established for more than 40 years ago in order to investigate the discontinuity inside the material body to study the behavior of strain localization in the post-bifurcation circumstance. The main idea of bifurcation theory is that the deformation inside the material will progress from a continuous mode to both continuous and discontinuous modes. When the localization initiates to present inside the mass body, the material will be divided into three main parts; the localization zone and two of intact zones. The mathematical concept of this bifurcation theory can properly describe the discontinuity inside the continuum. The unambiguous detail of these studies can be found in Vardoulakis (1979, 1983), Sulem and Vardoulakis (1990), and Vardoulakis and Sulem (1995). The bifurcation theory can be applied to the frictional and cohesive materials. It can be employed to simulate various modes of failure, i.e. necking, bulging, splitting and shear banding, inside the material. However, the failure mode of theory is yet influenced by many factors such as the loading conditions, boundary conditions as well as the constitutive model. As a result, a careful attention should be paid to avoid an undesired outcome from the analysis. It is also crucial to noted that this theory of bifurcation contains three important limitations: 1) it can only simulate the emergence of strain localization but cannot analyze its progression and development, 2) There is no warranty that during the analysis the strain localization will be manifested or not and 3) the determination of shear band thickness is not possible because of some limitations, i.e. no length scale, of continuum mechanic concepts.

- Cosserat continuum or Micropolar continumm

According to an ordinary continuum theory, the materials are ideally assumed as the continuum media. This assumption requires only translation degree of freedom of the particles. Therefore, this hypothesis is solely valid when the material response does not exhibit any discontinuity inside the body. It is widely recognized, however, that a non-homogeneous deformation inside the body will present after

reaching a peak state of stress. This discontinuity will take to an intense deformation within a finite zone of localization. Very high strain gradient variation followed by grain rotation, sliding and dilation will be observed within this zone. Due to the lacking ability of a conventional continuum and the complexity of strain localization, the Cosserat or Micropolar continuum can transcend those limitations by incorporating the rotational degree of freedom together with couple stresses in the analysis. The Cosserat theory can perfectly describe the grain rotation in addition to grain translation for the study of strain localization. Since the grain particles will rotate and translate when subjected to a substantial amount of pressure, for an analysis in the Cosserat continuum of a single grain, six degrees of freedom will be analyzed. The widely known studies of strain localization by using Cosserat continuum approach can be found in Kanatani (1979), Mühlhaus and Vardoulakis (1987), Vardoulakis and Sulem (1995) and Oda and Iwashita (1999).

- Strain gradient theory

Due to lack of some capacities of the conventional continuum mechanics to explain a complete behavior of strain localization, various researchers have proposed many new calculation techniques. One of these new approaches is the strain gradient theory. The advantages of this method are for example the capability to solve the mesh dependency in numerical simulation and the micro-scale of size effects. Aifantis (1984, 1987), Zbib and Aifantis (1988) included the length scale coefficient in their gradient plasticity model with shear band width to interpret size effects in metals. Vardoulakis and Aifantis (1989) used the second-order gradient theory in studying the heterogeneous deformation in the granular media. They had also modified a flow theory to incorporate high-order gradients and investigate the liquefaction problem in granular materials. During 1991, Vardoulakis and Aifantis had extended their works in 1989 to integrate the second-order gradients into the flow rule and the yield function, they were able to calculate the shear band thickness. Oka *et al.* (2001) used gradient dependent viscoplastic constitutive models to study the localizations in saturated soils. They had used the second-order strain gradient in the hardening function and found that strain localization is highly dependent on the strain

gradient. It may be implied that the results of strain localization simulation will be more accurate if strain gradient theory is combined with Micropolar theory in the analysis.

2.1.2 Experimental approach

Experimental studies of strain localization in granular materials have been performed by a series of researchers: Vardoulakis and co-workers (Vardoulakis *et al.,* 1978; Vardoulakis and Graf, 1985; Han and Vardoulakis, 1991), Tatsuoka and co-workers e.g. (Tatsuoka *et al.,* 1986; Tatsuoka *et al.,* 1990), Arthur (Arthur *et al.,* 1977; Arthur and Dunstan, 1982), Finno and co-workers (Finno *et al.,* 1996; Finno *et al.,* 1997), Desrues and co-workers (Desrues *et al.,* 1985; Desrues, 1990; Desrues *et al*., 1996; Mokni and Desrues, 1999; Desrues and Viggiani, 2004). These researchers experimentally clarify many helpful answers relating to strain localization in geomaterials. The conclusions among them are as follows:

- Strain localization inside the geomaterials, i.e. sand, can be observed in the conventional and modern laboratory tests for example triaxial test, plane strain test, direct shear test and hollow cylindrical test

- The complex localization patterns might be the result of size and slenderness ratio of the specimens as well as loading conditions. In a short specimen, when test in a compression triaxial device, the complex pattern of shear band zones might be emerged due to the effect of boundary condition. However, those intricate shear bands will be vanished in a long specimen.

- At peak stress in stress-strain curve, many researchers, using various detection techniques, reported full establishment of strain localization or shear band zones. Plane strain experiments on sand performed by Desrues *et al.* 2004, using stereophotogrammetry to detect graphically the onset of strain localization, showed that the initiation time of strain localization is always observed at or before the peak stress-strain curve.

Besides the conventional tests in geotechnical engineering, i.e. plane strain and triaxial tests, various experimental techniques have been performed to help in studying the emergence and evolution of strain localization. Those techniques can quantify shear band volumetric, capture density variations quantitatively within shear band, measure physical characteristics, i.e. inclination angle and thickness, within shear band. The complete review of those testing methods are detailed in the following sections.

2.1.2.1 Plane strain test

Plane strain test or biaxial test is an ordinary test in geotechnical engineering to simulate the in-situ cases of soil behavior, i.e. strip footing and slope stability analysis. Several researchers, e.g. Lee (1970), Arthur *et al.* (1977), Vardoulakis (1977 and 1980), Vardoulakis *et al.* (1978), Peters *et al.* (1988), Finno *et al.* (1997), Desrues (1998) and Alshibli *et al.* (2003), have conducted the plane strain tests in many types of testing conditions to observe the localized deformation inside the soil sample. The higher peak value of stress followed by strain softening of stress-strain relation has been documented for sand of various packing conditions. The stress value also increases as the confining pressure increases. Moreover, the difference in a mode of failure between plane strain compression test and triaxial compression test can be evidently observed. The failure pattern of specimen in plane strain test is really uniform and distinct whereas in triaxial compression test the complex pattern of shear band can be detected. However, a unique and uniform width of shear band might be perceived in a long height of specimen under triaxial test. The emergence time of strain localization is also influenced by the condition of loading. Namely, strain localization under plane strain test occurs faster than that of triaxial test.

The experiment works of Vardoulakis (1977 and 1980) and Vardoulakis *et al.* (1978) at Karlsruhe University can show clearly an idea of plane strain compression test. In the apparatus shown in Fig. 2.4, wherein a sample $4 \times 8 \times 14$ cm^3 was wrapped into a rubber mould of 0.3 mm thickness. A so-called Karlsruhe dry sand was used. The index properties of sand were: mean grain diameter $d_{50} = 0.45$ -

0.50 mm, grain size among 0.08 mm and 1.8 mm, uniformity coefficient $U = 2$, maximum specific weight $\gamma_d^{max} = 17.4$ kN/m^3, minimum void ratio $e_{min} = 0.53$, minimum specific weight $\gamma_d^{min} = 14.6$ kN/m^3 and maximum void ratio $e_{max} = 0.84$. Two side plates used for the condition of plane strain; they carried polished stainless steel plate and a silicone grease to prevent boundary friction. The base and top plates were also polished and lubricated and carried 10 mm diameter porous stone to keep the sample in the center position. The base plate was placed on a movable roller bearing. In some tests, Fig. 2.4, the specimen did not include any artificial imperfection. In some other tests, Fig. 2.5, a small artificial initial imperfection (side notch or loose sand inclusion) was included. The test results showed that an internal shear zone was formed at the peak of the stress-strain curve. The thickness of the shear zone was about 3-5 mm, i.e., $(10 - 15) \times d_{50}$, and the inclination angle of the shear zone was approximately 52 - 67°. This inclination angle was in accordance with the formula by Arthur *et al.* (1977). The shear zones were less steep in initially looser samples than in dense samples. The shape of the shear zone was influenced by the type of the imperfection (shear zones with a notch were slightly curved). Looser sands were more sensitive than dense ones. The maximum angle of internal friction decreased almost linearly with increasing void ratio.

(a)   (b)
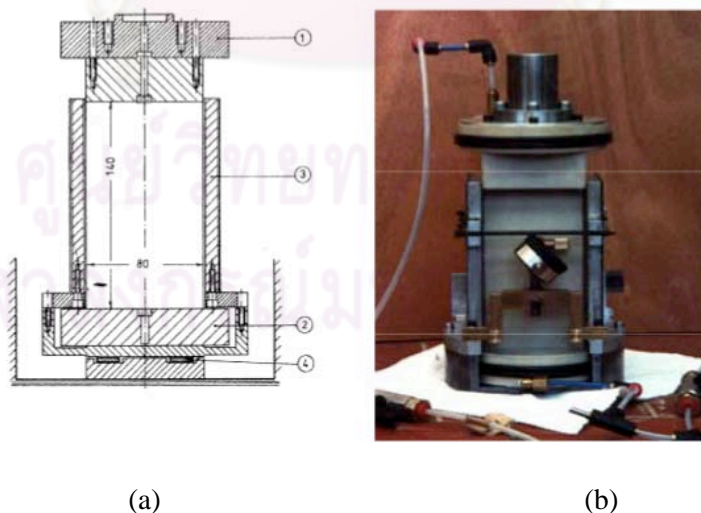
Fig. 2.4 Plane strain compression apparatus: (a) System 1) top plate, 2) base plate, 3) side plates and 4) roller bearing, and (b) Photograph (Vardoulakis, 1977)

(a)   (b)
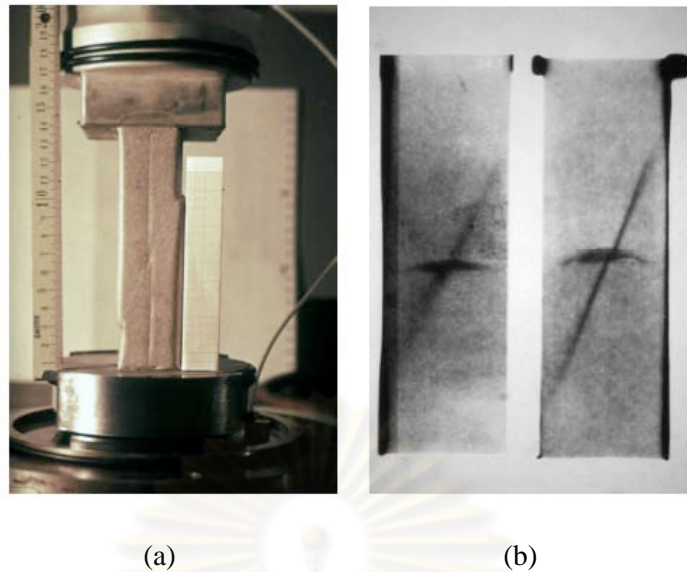
Fig. 2.5 Formation of shear zone in dense specimen (a) without initial (b) with initial
imperfection in the form of loose sand inclusion on the basis of X-rays radiographs
(Vardoulakis, 1977)

Other well-known plane strain compression tests to study localization
in sands are perform by Desrues (1985) and later modified by Hammad (1991) at
Grenoble University. The Schematic diagram of a plane strain apparatus can be shown
in Fig. 2.6. The results of their works showed that various patterns of shear zones
were observed including even parallel and crossing shear zones depending on
boundary conditions and slenderness of the specimen. The onset of shear localization
took place slightly before the peak of the stress ratio. The inclination angle of shear
zone decreased with increasing pressure. The shear zone thickness decreased as the
confining stress and initial density increased. The reduction of the specimen size or its
slenderness delayed the onset of strain localization. For higher slenderness ratio, other
bifurcation modes, e.g. buckling, were more likely to occur. The shear zone thickness
increased with increasing particle size and its inclination angle was not affected by the
mean grain size and non-uniformity of sand grading. The inclusion of material
imperfection dictated the location of the shear zone and acted as a trigger for the onset
of shear localization.
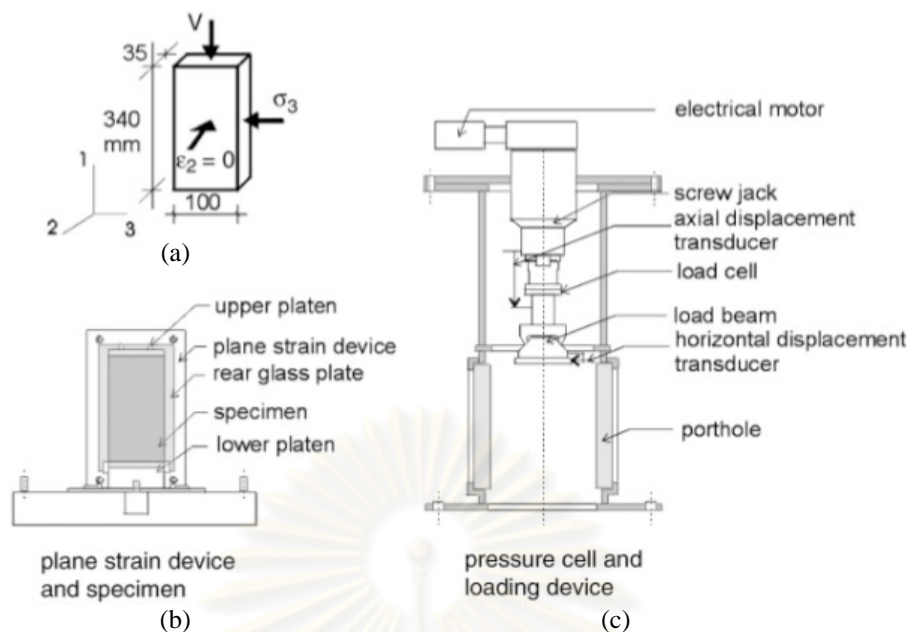
Fig. 2.6 Schematic diagram of a plane strain apparatus at the University of Grenoble:
(a) specimen geometry, (b) plane strain device and specimen,
(c) pressure cell and loading device
(Desrues and Viggiani, 2004)

2.1.2.2 Triaxial test

Two types of conventional triaxial test, i.e. triaxial extension and triaxial compression test, have been performed continuously since 1970 to investigate the behavior of strain localization within soil samples in laboratory. Roscoe *et al.* (1963) demonstrated that the conventional triaxial extension test has substantially more problems associated with strain localization than the triaxial compression test. Yamamuro and Lade (1995) investigated the behavior of granular materials in triaxial extension test both drained and undrained test of cylindrical specimens to study the influence of plastic strain localization in granular materials. They found that the failure was rapidly occurred in all conventional extension tests and the strain localization appeared to begin very early during the shearing process. They also concluded that the conventional extension test is inherently unstable and exhibits the high scattered testing results. The axisymmetric conventional triaxial compression test, CTC, is the most common experiment used by geotechnical engineers to observe the strength and deformation responses of soils. However, in the CTC experiments

localization patterns are more difficult to detect and describe. In CTC, there are two modes of failure that can be occurred, localized shear plane mode or bulging diffuse mode, depending on the density and geometry of the specimen and the confining pressure. Alshibli *et al.* (2003) indicated that the confining pressure and specimen packing condition have a profound influence on the behavior of CTC specimens. Specimens show a very high-peak friction angle followed by severe softening for specimens tested under very low-confining pressures and the amount of softening decreases as the confining pressure increases. All CTC specimens show nearly the same residual stress regardless of the confining pressure value.

Desrues *et al.* (1996) performed the axisymmetric CTC tests. The diameter of the sand specimen was 100 mm and the height was 100 or 200 mm. A special anti-friction system was used. The shear zones were detected using X-ray tomography. The tests were carried out on dense and loose sand with lubricated and non-lubricated specimens. In initially dense specimens, localization of deformation was observed to depend greatly on test conditions. In a dense specimen with non-lubricated ends, the slightly curved shear zone was created (Fig. 2.7). When the specimen was short, the localized deformation was initiated with a single rigid cone attached only to one of the platens but the other platen did not generate any cone (Fig. 2.8).

(a)   (b)
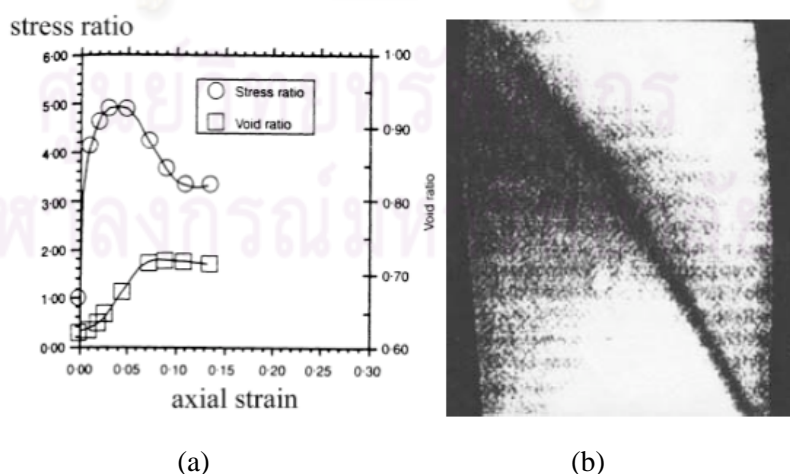
Fig. 2.7 (a) Evolution of the stress ratio and void ratio (b) formation of a shear zone during the experiment with a high dense specimen and non-lubricated ends

(Desrues *et al.,* 1996)

(a)   (b)
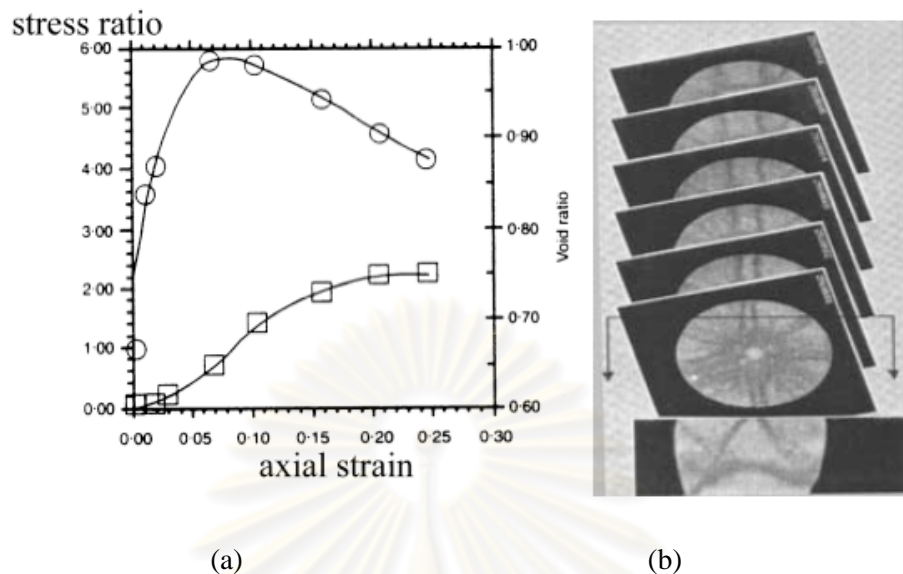
Fig. 2.8 (a) Evolution of the stress ratio and void ratio (b) formation of shear zones

during the experiment with a low dense specimen and lubricated ends

(Desrues *et al*., 1996)

2.1.2.3 X-ray imaging techniques

The visual investigations of strain localization mechanisms have been carried out over the years. These techniques are for example X-ray radiography, Computerized Tomography and Digital Image Analysis (DIA). Roscoe (1970) performed experimental studies on plane strain models of different geotechnical structures such as retaining walls. He used an X-ray technique to measure the displacement of small lead shot distributed in the sand mass. He could observe the dark bands on the radiographs, then stated that, "*this dark band represents the rupture surface in which the sand has dilated to the critical state*". The same observation was made using the same X-ray technique by other researchers in triaxial test, plane strain biaxial test, simple shear apparatus, and directional shear cell. Though, these X-ray measurements have given most valuable qualitative information on localization patterns in sand specimens, but they generally contain three limitations: the lack of quantitative data on the observed density changes, the limitation to plane strain

experiments, and the lack of providing the 3-D radiograph or images. Fig. 2.9 shows the result of the X-ray photography acquired from plane strain test.
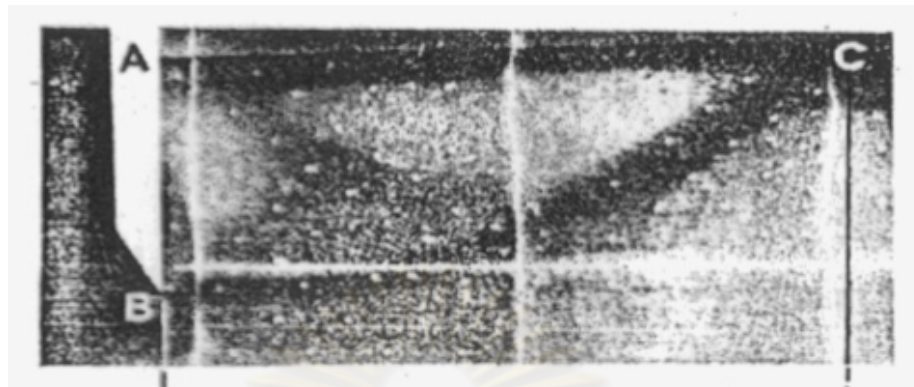
Fig. 2.9 X-ray photography used on plane strain models allowed Roscoe and his collaborators to show the large dilatancy taking place in shear zones in the modeling of retaining wall (Roscoe *et al.*, 1970)

2.1.2.4 Stereophotogrammetric method

Stereophotogrammetry, firstly applied to soil mechanics experiments by Butterfield *et al.* (1970), provides the measurement of local volumetric strain increment in sand. This method had been further developed and extensively used by many scholars, i.e. Vardoulakis (1979, 1980) in Karlsruhe and Desrues *et al.* (1985). Desrues and Viggiani (2004) explained in their paper that the advantage of this technique was an ability to capture non-homogeneous strain throughout the test. The method of "False Relief Stereophotogrammetry" (*FRS*) is based on the analysis of photographs taken from a fixed viewpoint at different times during the loading process. An essential feature of *FRS* is that the deformation can be directly perceived as a fictitious relief by using the well-known stereoscopic effect on successive pairs of photographs. In the application of *FRS* to observe strain localization of sand, the difference of deformation between successive images will be calculated and recorded. When these two photographs are viewed in stereo, displaced regions appear elevated, with the elevation proportional to the magnitude of displacement. In the presence of a shear band, the deforming specimen appears as two planes of different elevation connected by a slope. For a given pair of photographs and thus a given increment of the global axial strain, the shear band can be therefore completely characterized, in

terms of both width and orientation. These systematic analysis of successive photographs of the deformed specimen allowed for observing the evolution of localized deformations throughout the test. The use of stereophotogrammetry as a quantitative tool can use to present the evolution of localized deformation in terms of incremental strain fields. Fig. 2.10 shows the stereophotogrammetry-based incremental fields of shear strain intensity and volumetric strain. Although digital image correlation software nowadays becomes a competitive method to study strain localization. This numerical image correlation is easier to use and requires less efforts in the analysis. However stereophotogrammetry has some benefits especially when strong discontinuities present in the body.
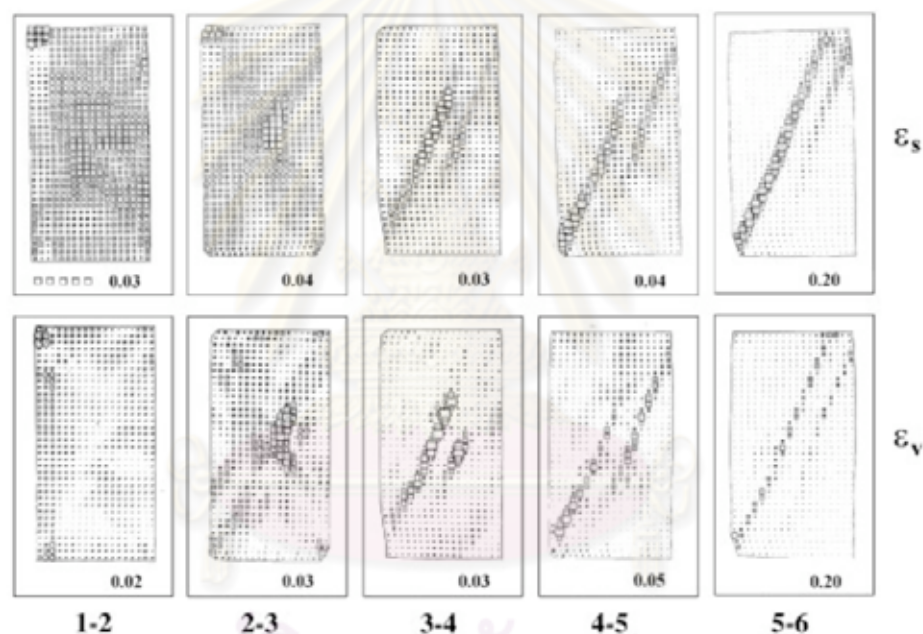
Fig. 2.10 Stereophotogrammetry-based incremental fields of shear strain intensity (top row)

and volumetric strain (bottom row)

(Desrues, 1985)

2.1.2.5 Gammametry techniques

Gammametry technique is used for local density measurements. This conventional technique has been used by several authors for many years. In the studies of strain localization, this technique was used in Grenoble by Desrues (1984), and Desrues *et al.* (1985) to perform quantitative measurements of mass density

changes in the localized shear zones of sand specimens subjected to plane strain loading (Fig. 2.11).
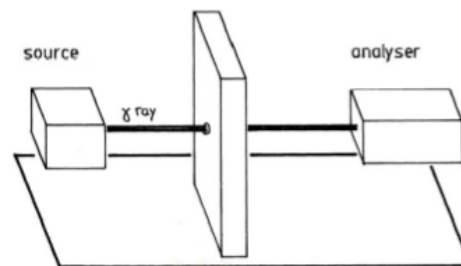
Fig. 2.11 Gamma-ray device used to measure the local density in shear bands

in plane strain specimens (Desrues, 1984)

The studies by Desrues was performed on both plane strain and true triaxial tests. In both cases, the specimens was loaded to failure then unloaded and kept to a constant volume by applying a vacuum pressure to the specimen. This temporarily hardened sample was then transferred to a Gamma-ray device in order to measure the density profile within the shear band zone. The intensity of the attenuated beam was measured by a detector. In both cases, significant dilation can be captured in the shear band zones. Fig. 2.12 and 2.13 show the density profile across a shear band and density profile before and after loading in plane strain test of dense specimen with low confining pressure, respectively.
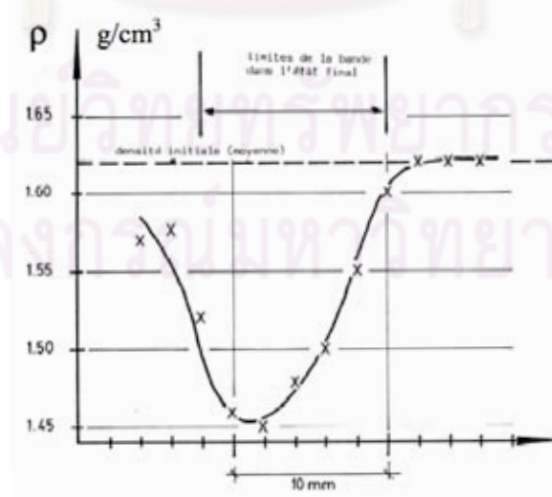
Fig. 2.12 Density profile across a shear band in plane strain test of dense specimen with low

confining pressure recorded by Gamma-ray absorption (Desrues, 1984)
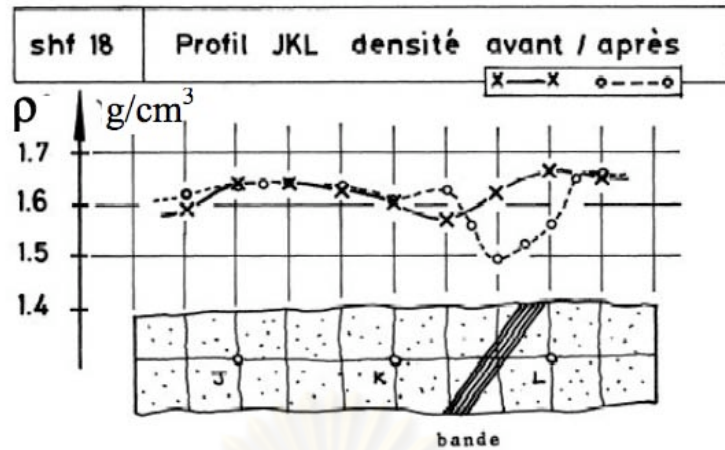
Fig. 2.13 Density profile before and after loading in plane strain test of dense specimen
with low confining pressure (Desrues, 1984)

2.1.2.6 Computerized Tomography (CT)

Computerized Tomography (CT) has been extensively used in the
medical inspection throughout the human body by medical practitioners. The common
name is known as "X-ray scanner". This technique can be used to measure the density
variation within the specimens. A three-dimensional figure can also be displayed by
combining the adjacent slices of two-dimensional density map acquired from several
angles across a single plane. The sample of experimental setup of CT system device
can be illustrated in Fig. 2.14 by Desrues *et al.* (1996).
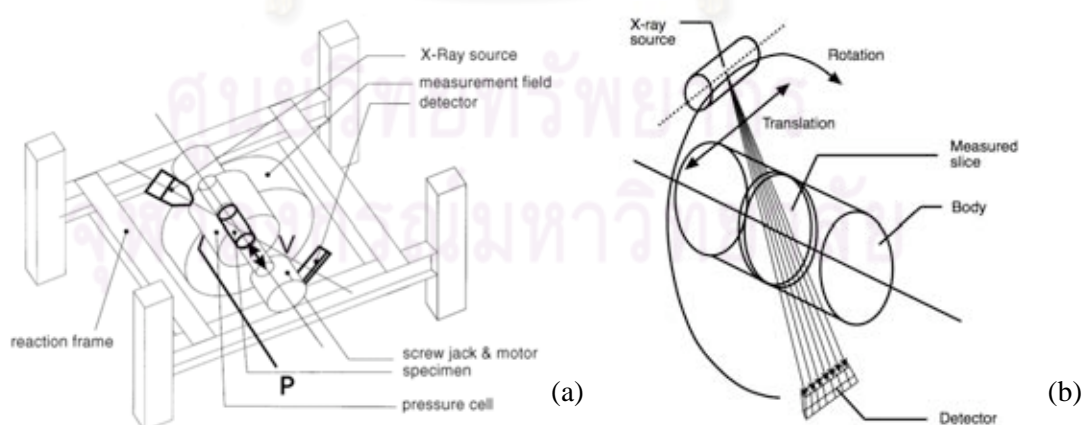
Fig. 2.14 (a) Experimental device: specimen, triaxial cell, scanner field measurement
and reaction frame (b) the technique of CT scan (Desrues *et al.,* 1996)

The uses of CT technique to study the strain localization in geotechnical engineering can be found in the literature. Raynaud *et al*. (1989) and Vinegard *et al.* (1991) had published their works of axisymmetric triaxial tests and showed that CT technique could describe some important characteristics of strain localization, i.e. density variations, inside rock specimens. Hicher *et al.* (1994) used CT to study strain localization in clay specimens. Their studies showed the density alteration inside the localized zone. Namely, the density in the shear band zone was increased relating to the rest of the specimen. However, in undrained tests, no density change could be observed within the shear band zone, though direct visualization confirmed the emergence of strain localization in these tests. For the granular materials, CT technique is extensively used to acquire a series of images of shear band as well as the evolution of strain localization from both of plane strain and triaxial compression test by Desrues (1984), Desrues *et al.* (1996), Alshibli *et al.* (2000 and 2003), and Batiste *et al.* (2004). Their results reveal that the inception and the development of the localization in sand specimens could be well detected and described, both qualitatively and quantitatively. Fig. 2.15 shows the images of CT scan technique of two orthogonal axial sections and two cross sections taken at one third and two thirds of the specimens height under conventional triaxial compression experiments with various test conditions (Alshibli *et al.,* 2003).

2.1.2.7 Digital Image Analysis (DIA)

Most of the experimental studies on strain localization were dependent on the visual observations of deformation profile within the specimens. Because of a rapid revolution of computer industry both in software and hardware development. Digital Image Analysis (DIA), to some extent, allows the researchers to capture and analyze local strain within the specimen as a function of global strain for the strain localization analysis. During the loading process, DIA was used to monitor the entire specimen uniformity, initiation time of localization as well as to determine the specimen dimensions.
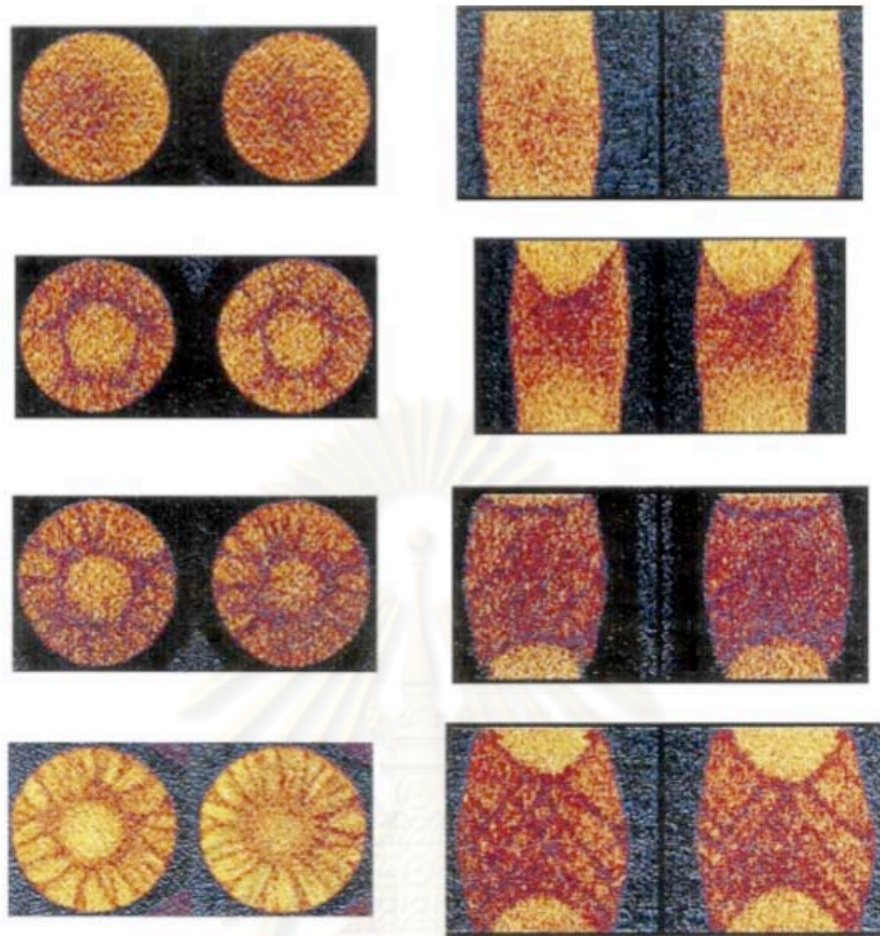
Fig. 2.15 shows CT scan technique of two orthogonal axial sections and two cross sections taken at one third and two thirds of the specimens height under conventional triaxial compression experiments with various test conditions (Alshibli *et al.,* 2003)

Alshibli and Sture (1999) used the DIA to study localized deformations in granular materials tested under plane strain condition (Fig 2.16). They used two independent DIA techniques to measure the shear band thickness. In the first technique, the digitized optical images of a grid printed on the latex membrane, known as a surface measurement, were used to measure the shear band orientation angle and thickness (Fig. 2.17). The second technique used an ultra-low viscosity resin to harden the specimen in preparation of epoxy impregnation and thin-sectioning to study microscopic images of the internal fabric (Fig. 2.18). The observation of this microscopic images is a quantitative analysis of local void ratio of sand. Void ratios are calculated based on the relative areas occupied by voids and particles within these slices.
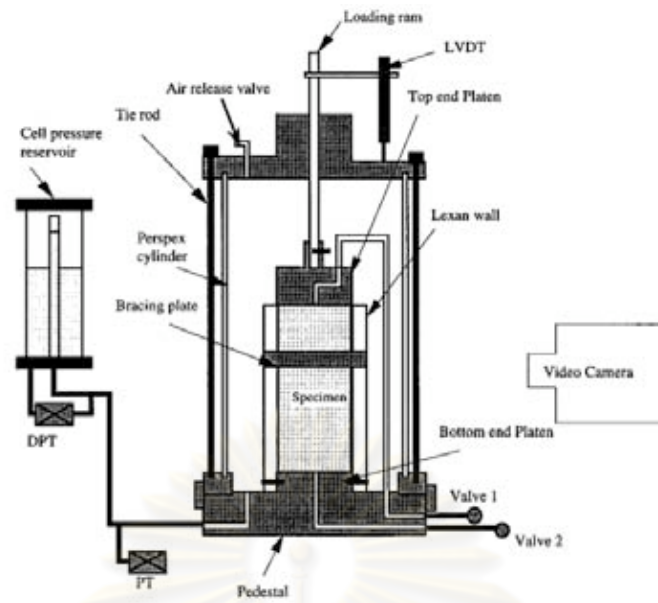
Fig. 2.16 Schematic of experiment apparatus to study strain localization by DIA
(Alshibli and Sture, 1999)
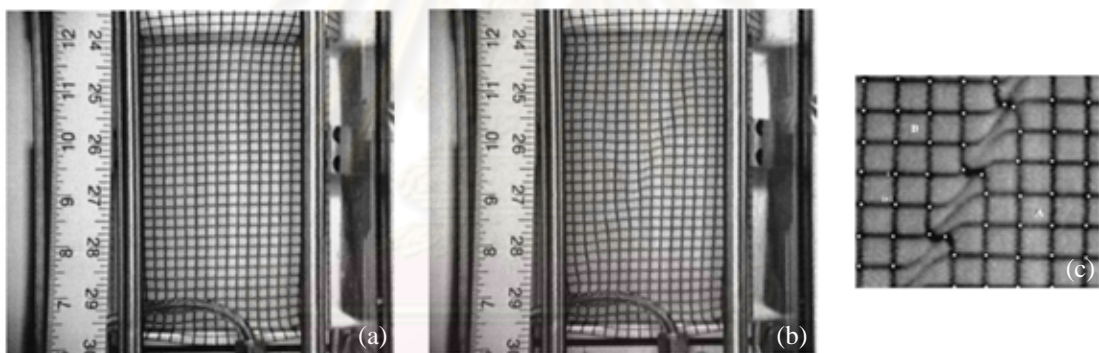
Fig. 2.17 Specimen image (a) before compression (axial strain = 0 %) (b) deformed specimen
at 3.8% axial strain (c) magnified image showing grid relative displacement within shear band
(Alshibli and Sture, 1999)

Alshibli and Sture (1999) finally concluded that DIA demonstrates an
excellent ability in accurately measuring localized deformations in granular materials.
Localized deformations of granular materials can be easily and accurately monitored
and measured using surface digitization. Moreover, they summarized that microscopic
image measurements, from epoxy impregnation and thin-sectioning, of the void ratio
variation can be accurately used to measure the shear band thickness. Shear band
thickness measurements obtained from membrane surface digitization and epoxy
impregnation techniques are also very close.
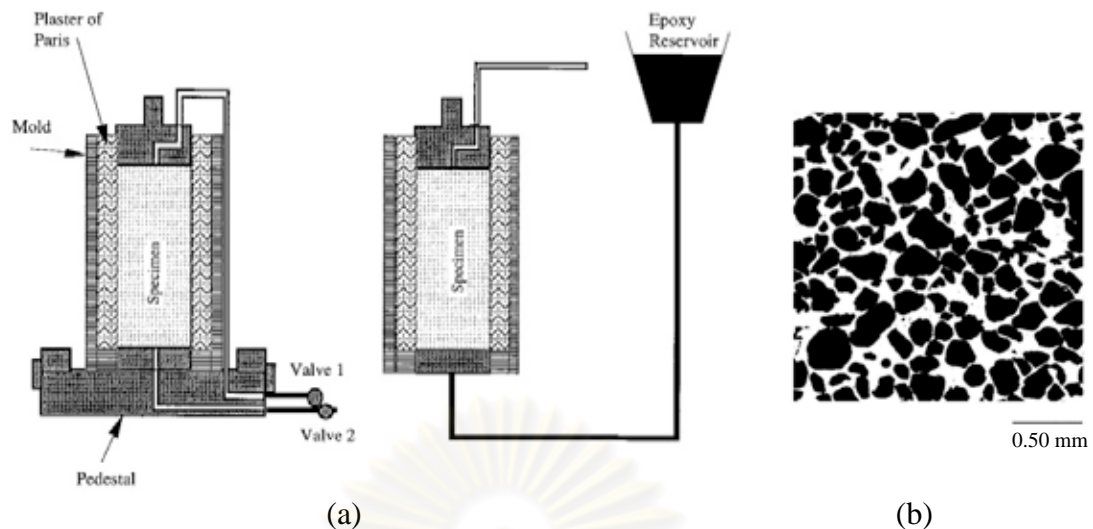
Fig.2.18 (a) Schematic of cross section of specimen resin impregnation setup (b) typical microscopic image of the tested sand after hardening in the epoxy
(Alshibli and Sture, 1999)

Sachan and Penumadu (2007) used DIA to evaluate the strain localization mechanisms, i.e. evolution of shear bands with respect to the loading boundary conditions, in the solid cylindrical Kaolin clay specimens sheared by using lubricated end both in compression and extension triaxial tests. A latex membrane, thickness of 0.3 mm with dots marked in a grid pattern, was placed on the cylindrical specimen used for triaxial testing, which was confined in a cast-acrylic cylinder filled with water. The dots on the membrane were tracked using high resolution digital images taken by a 2.1 million pixel resolution (1792 H: 1200V) of digital camera. This digital camera was placed at about 562 mm distance from the outer wall of cell and mounted on a two-axis controller, which allowed for precisely adjusting camera position in two directions. A soft light was also used to provide uniform illumination of the triaxial specimens and significantly reduced shadows in the digital images. Fig. 2.19 shows the digital image setup and prepared Kaolin clay specimen for triaxial test. After finishing an experimental work, all captured images will then be downloaded to a personal computer to measure the coordinates of the dots by image analysis software. After processing the images taken during triaxial test and developing the contour plots to illustrate the strain field, they found that corresponding local strain contour plots indicated the formation of strong localized deformation zones at high

strain levels. As a result, these contour plots could present the evidence of the occurrence of strain localization due to shear banding within the clay specimen. Moreover, the variation in strain localization patterns of soil specimen could also be used to evaluate the influence of confining stress, loading conditions, stress history, drainage conditions, and soil's microfabric in lubricated-end triaxial tests (Fig. 2.20).

(a)   (b)
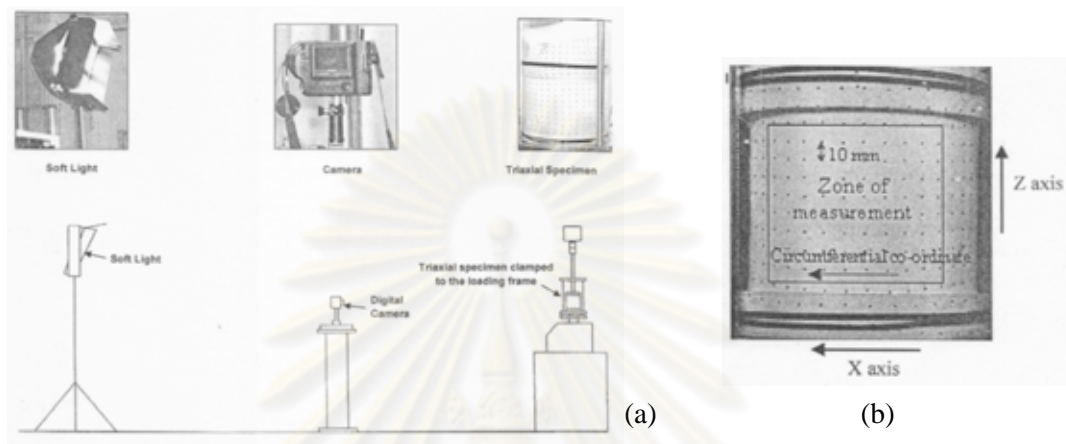
Fig. 2.19 Strain localization using DIA techniques (a) digital image setup

(b) prepared Kaolin clay specimen (Sachan and Penumadu, 2007)
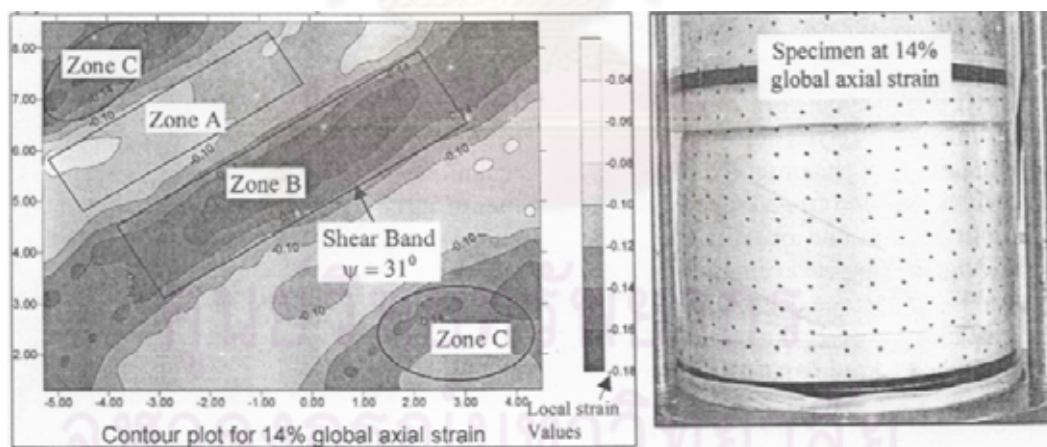
Fig 2.20 An example of contour plots and the digital image of shear band formation

(Sachan and Penumadu, 2007)

2.1.2.8 Digital Image Correlation (DIC)

The basic concept of Digital Image Correlation (DIC) is the correlation of a group of points or pixels between two digital consecutive images taken at

different times in a deformation process. By overlapping these groups of pixels, a complete field displacement can be obtained and identified in the computer software. Rechenmacher and Finno (2004) had performed the plane strain compression experiments on dense sands by the technique of DIC to quantify directly internal strain field. They found that the use of DIC technique is a highly accurate technique for quantifying localized displacements in sands. Fig. 2.21 illustrates the images of displacement fields from DIC techniques.
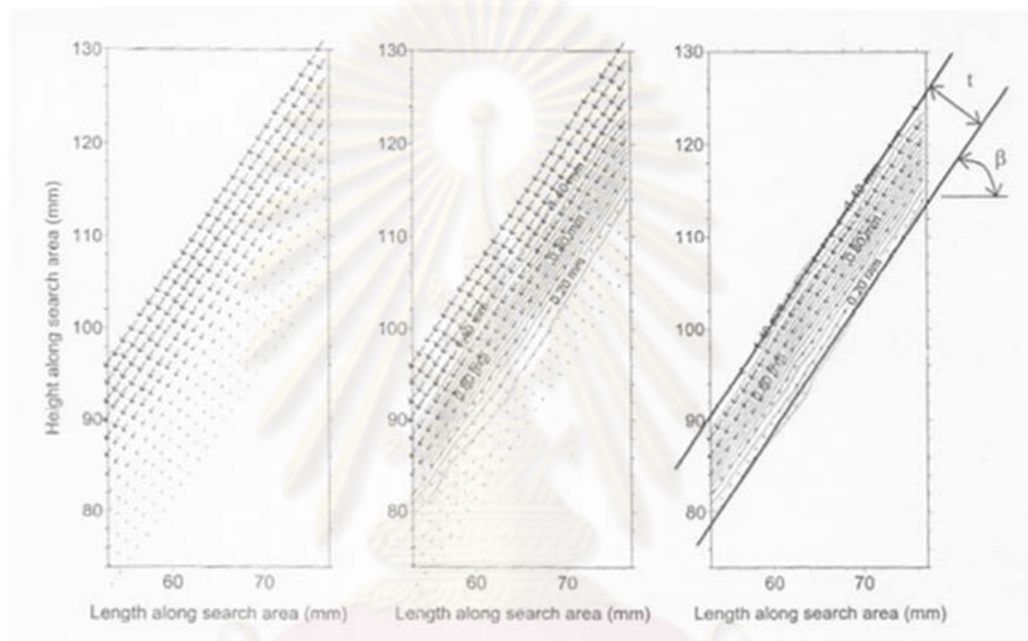
Fig. 2.21 DIC measured displacements surrounding a persistent shear band
(a) DIC displacements (b) contour fitted to displacements (c) shear band displacement points isolated for strain localization (Rechenmacher and Finno, 2004)

2.2 Factor Affecting Strain Localization

There are a number of factors that influence the physical mechanisms of strain localization or shear band, i.e. thickness, orientation as well as the initiation time of strain localization. These factors include the initial stress state, confining stress, grain characteristics and the geometry of the specimen. The influences of these factors will be further discussed in the following sections.

2.2.1 Mean effective stress and confining stress

Desrues *et al.* (1989) performed the testing program to find the dependency of shear band on mean stress level and density in sand. Tests on water-saturated RF Hostun sand were conducted on both dense and loose specimens with initial packing conditions of approximately 95% and 25%, respectively. The initial mean stress applied to the dense sand varied from 100 - 800 kPa with the specimen slenderness of 3.35 for all tests. The results are shown, in Fig. 2.22 and 2.23, in terms of stress ratio $t/s´$ and volumetric strain, ε_v, as a function of axial strain ε_1. Stereophotogrammetry indicated that for all four tests, shear banding initiates at, or shortly before, a point of peak stress ratio and the subsequent stress ratio drop is associated with the complete development of a single shear band. The influence of initial mean stress on the conditions for the onset of shear banding is obvious from stress-strain responses from dense RF Hostun sand (Fig. 2.22). The higher the confining effective stress, the later the strain localization occurs. Also the peak value of $t/s´$ clearly depends on the confining stress, namely it increases with decreasing of confining pressure. In conclusion it can be stated that for a given density of sample, an increase in the initial mean stress delays the appearance of strain localization.

(a)   (b)
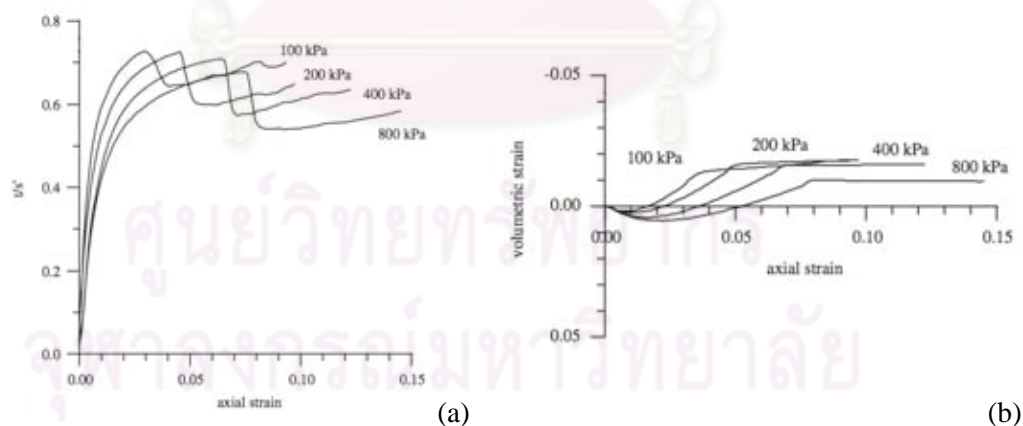
Fig. 2.22 Stress strain responses from four tests on dense RF Hostun sand:
(a) stress ratio (b) global volumetric strain versus global axial strain (Desrues, 2004)

Fig. 2.23 shows the results from four tests on loose RF Hostun sand in the same range of initial mean stress as for the dense specimens. The specimen slenderness was kept constantly at 3.35 for all tests. In these tests, the curve of the

effective stress ratio and axial strain does not exhibit any sharp peak, which is typical for loose specimens. Moreover, the increase in the confining pressure also delays the onset of strain localization as on the dense specimens.
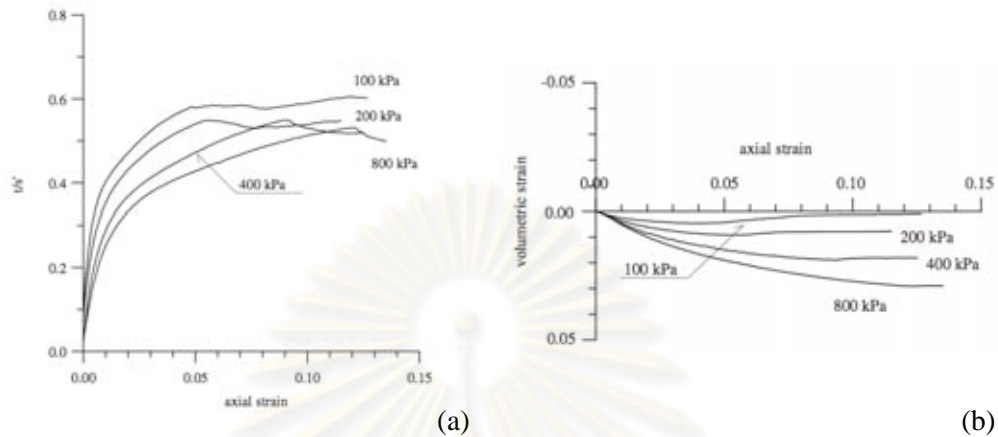
Fig. 2.23 Stress strain responses from four tests on loose RF Hostun sand:
(a) stress ratio; and (b) global volumetric strain versus global axial strain (Desrues, 2004)

Desrues (2004) also reported that the shear band thickness depends on both initial density and mean effective stress, as first suggested by Tatsuoka *et al.* (1986). He stated that for a given sand the width of the shear band decreases as the confining stress and the initial density increase. For dense Hostun sand, shear band thickness reduces from 22 to $13d_{50}$ as the effective confining stress increases from 100 to 800 kPa. A similar trend is observed for loose Hostun sand, the range of measured shear band widths being 31 to $17d_{50}$ over the same range of confining stress.

Alshibli *et al.* (2003) investigated the effects of confining pressure on strength properties and localization phenomenon in sands. A uniform subrounded to rounded natural silica sand known as F-75 Ottawa sand was used in their investigation. A series of conventional triaxial compression (CTC) experiments were tested under very low-confining pressures, 0.05 - 1.30 kPa, in addition to the results of normal to high confining stress, i.e. 10 - 70 kPa, to investigate the effect of confining pressure on the constitutive behavior of sands. Fig. 2.24 illustrates the outcome of some tests. They concluded that the confining pressure have a profound influence on the behavior of CTC specimens. Specimens show a very high-peak friction angle and dilatancy angles

followed by severe softening for specimens tested under very low-confining pressures and the amount of softening decreases as the confining pressure increases. Both angles decrease as the confining pressure increases. All CTC specimens show nearly the same residual stress regardless of the confining pressure value.
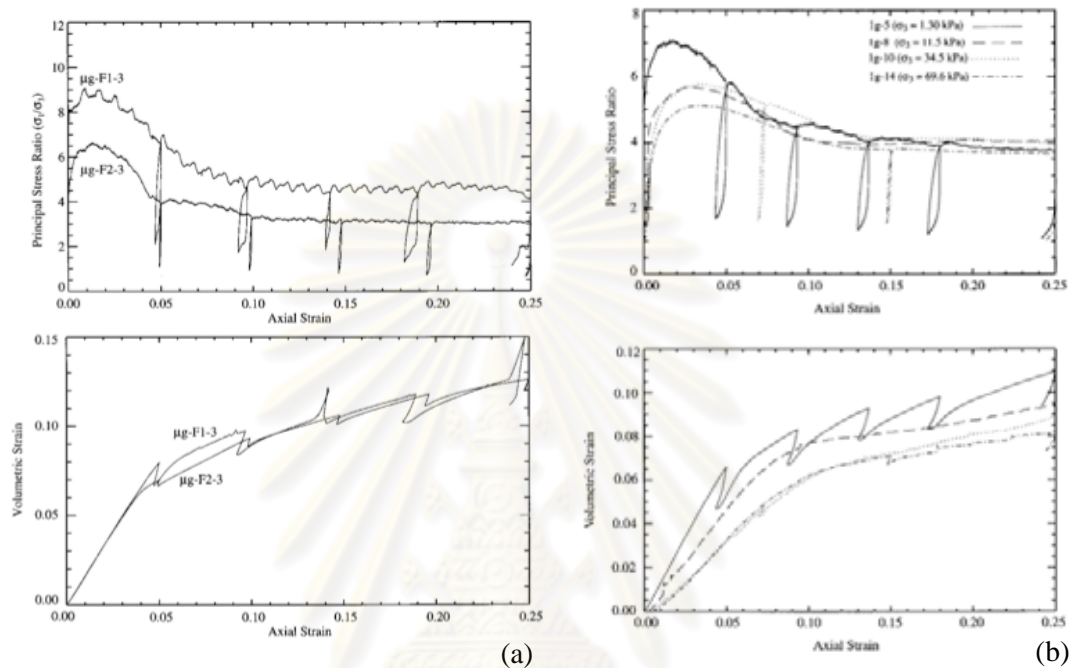
Fig. 2.24 Principal stress ratio versus axial strain and volumetric strain versus axial strain for CTC (a) confining pressure = 1.30 kPa (b) confining pressure = 1 - 70 kPa

(Alshibli *et al*., 2003)

2.2.2 Loading conditions

It is widely known that the stress-strain behavior and failure pattern of granular materials under plane strain (PS) test are different from the conventional triaxial compression (CTC) test. The failure of plane strain specimens always occurs along a unique and uniform shear plane. In the axisymmetric triaxial tests either localized shear plane or bulging diffuse failure modes occur depending on the density of the specimen and the confining pressure. Lee (1970) performed a series of drained and undrained PS and CTC experiments on fully saturated fine-grained sand. The results revealed that PS specimens reach higher values of maximum principal stress ratio than do CTC specimens, and the difference decreases as void ratio increases.

Moreover, PS specimens fail at smaller axial strain with a severe softening compared to CTC specimens. He finally concluded that the difference between PS and CTC results is greatest for dense specimens tested under low-confining pressure and that the difference decreases as confining pressure increases. Marachi *et al.* (1981) also performed a series of PS and CTC experiments on sand. Specimens were prepared to various initial void ratios. All experiments were performed under drained and air-dry conditions. Fig. 2.25 shows a comparison of the stress-strain relationship for both cases. The results are very similar to the behavior reported by Lee (1970).
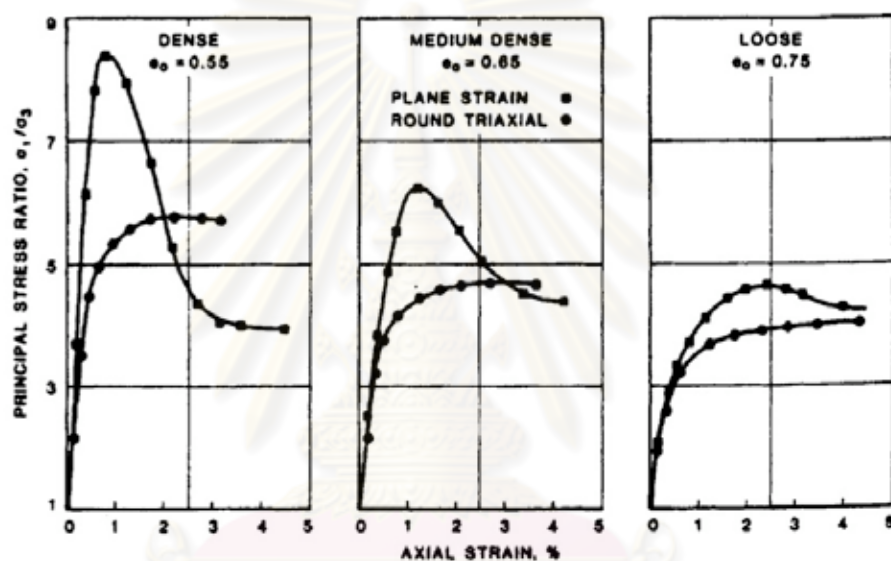
Fig. 2.25 Stress-strain relationship for plane strain and triaxial specimens
(Marachi *et al.* 1981)

Fig. 2.26 shows the results of experimental investigation between CTC and PS tests under low and high confining pressure of silica sand performed by Alshibli *et al.* (2003). PS specimens showed higher-peak stress value followed by severe softening. In all cases, the CTC experiments show very similar principal stress ratio versus axial strain responses. A very small strain softening can also be observed after the peak stress value and the specimens reached the residual stress condition at about 10% axial strain. They also concluded that the failure of specimens subjected to PS loading condition is characterized by distinct shear bands accompanied by softening in the stress response depending on the specimen density and confining pressure. In contrast, the specimens in CTC experiments bulge uniformly in the vicinity of peak

stress and develop complex multiple symmetrical radial shear bands at higher axial strain levels. Therefore, It is quite clear from those results that the deformation processes and the stability behavior are quite different between triaxial and plane strain tests.
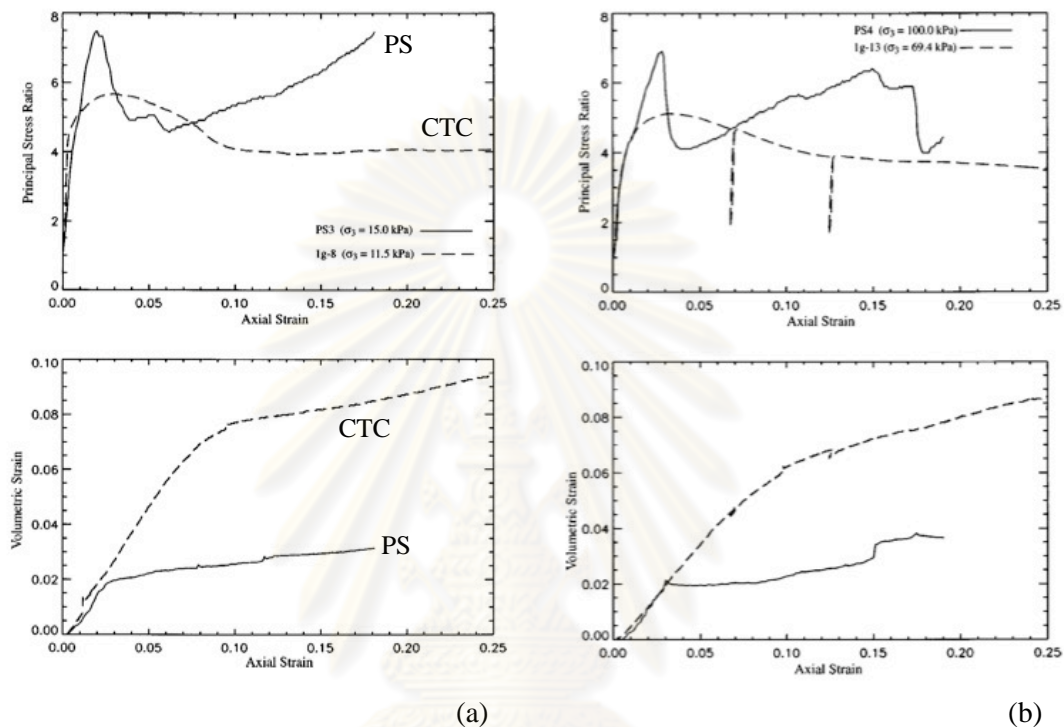
Fig. 2.26 Comparison between CTC and PS experiments of dense specimens tested under (a) low confining pressures and (b) high confining pressures (Alshibli *et al*. 2003)

2.2.3 Specimen geometry

Desrues *et al.* (1996) studied strain localization in triaxial tests on sand to observe void ratio evolution inside shear bands by using computed tomography (CT). Two of their tests performed with long specimens (slenderness ratio = 1.94 and 1.90). The result showed that a long specimen exhibits a single shear plane, though not perfectly planar, at a global axial strain ($\varepsilon_a = 7\%$) and remained the unique localization structure for larger strain (Fig. 2.27). In contrast to the above rather simple localization pattern, a short specimen (Slenderness ratio = 1.00) gave more complex localization pattern. Namely, a rigid cone, attached to the end platen, can be observed. This cone is delimited by a circular shear surface which is the locus of a large

dilatancy (Fig. 2.28). Moreover, the onset of localization was significantly delayed in the short specimen comparing to the relatively long specimen.

(a)   (b)
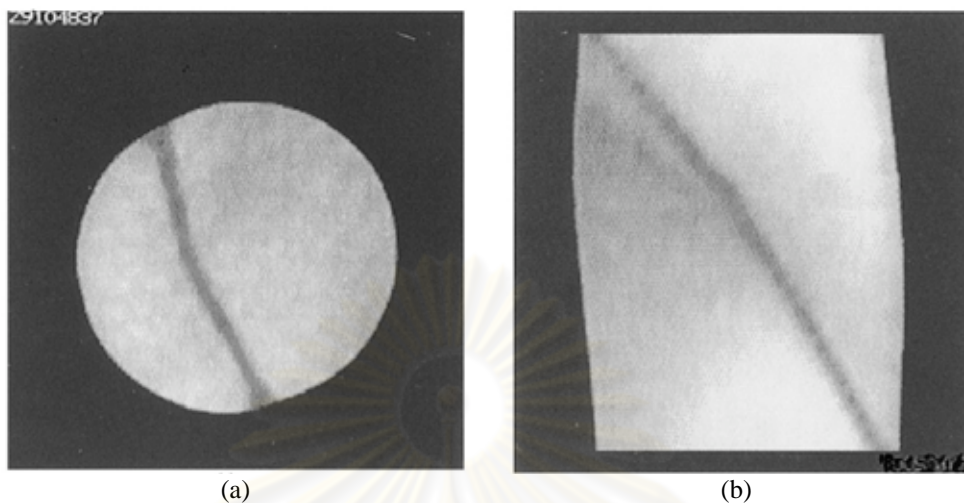
Fig. 2.27 Trace of the single shear plane in long specimen of Triaxial test on sand (a) in a section perpendicular to the axis (b) containing the axis of the specimen (Desrues *et al.* 1996)

(a)   (b)
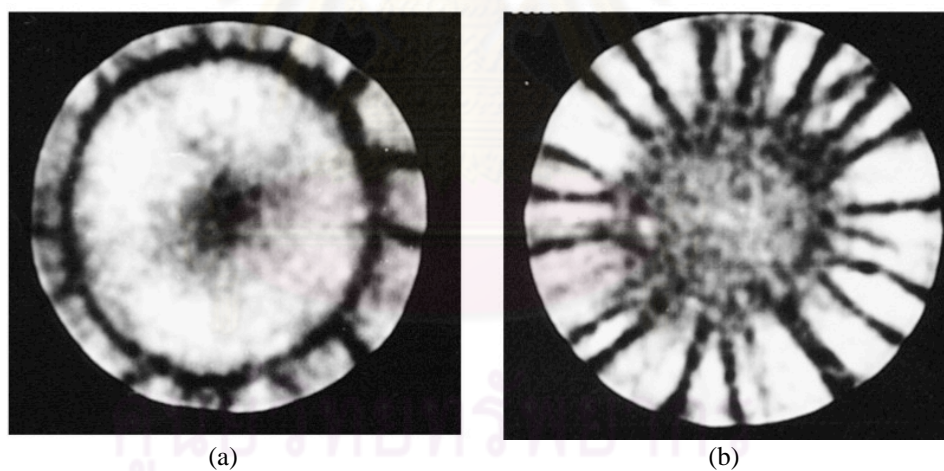
Fig. 2.28 Two cross-sections recorded in a short specimen, revealing complex localization patterns (a) near the upper platen (b) at the middle height of the specimen

(Desrues *et al.* 1996)

The effect of specimen geometry can also be observed in a paper carried out by Desrues (2004). He performed a number of plane strain compression tests on both dense and loose RF Hostun sands by varying four different values for the specimen slenderness (0.5, 1, 2, and 3.3). Three main conclusions can be summarized as

follows: the reduction of specimen slenderness ratio has the effect of (i) retarding the onset of strain localization (ii) reducing the steepness of the shear band and (iii) increasing the thickness of shear band.

2.2.4 Grain size

There are substantial experimental evidences showing that strain localization in sand depends on microstructure, i.e. grain size of the particles. For a certain stress state and loading conditions, different size of sand grain exhibit different responses both in terms of orientation and width of shear bands as well as the strain level at which shear banding occurs. These behaviors cannot be only explained in terms of macroscopic aspects such as void ratio and stress state. Many parameters such as shape and angularity of grains and grain size distribution profoundly influence the strain localization mechanism. Viggiani *et al.* (2001) investigated the influence of grain size distribution on strain localization in sand. The tests performed under different gradations of the same sand in terms of both the mean grain size and uniformity. Saturated specimens of the different sands were tested in plane strain under drained conditions starting from high relative densities. False relief stereophotogrammetry was used to capture the onset of strain localization and for accurately measuring the width and orientation of shear bands. The results confirm the dependence of the shear band thickness on the mean grain size (d_{50}). The testing results indicate that the ratio between shear band thickness and the mean grain size tends toward a constant limit value of approximately 7 for the largest grain size.

2.2.5 Role of imperfection

Desrues *et al.* (1996) and Desrues (2004) had investigated the influence of material imperfection on the behavior of strain localization by placing an artificial inclusion, i.e. a cylindrical of paper, cotton sphere and compact wood with a rough surface, into the sand specimen during sand deposition in the mold. The results showed that the location of the shear band is dictated by the location of the inclusion (Fig. 2.29) but the global stress–strain responses do not show any major deviation from the responses obtained from all the other tests performed at the same confining

pressures and initial density but without any inclusion. The plots of incremental strain field also reveals that in many cases strain localization initiates at more than one locations within a specimen. As the deformation progresses, a process of competition occurs among these different localization structures, with only one well-defined structure eventually taking over the others. On the contrary, in an imperfect specimen strain localization goes immediately to its final structure. This is a remarkable effect of the imperfection. Desrues, however, reported that the nucleation point for the initiation of localization in an imperfect specimen would not be occurred if an inclusion was placed in an axisymmetric position, i.e. on the axis at mid-height, inside the specimen (Fig. 2.30). This means that, in order to act as a localization attractor, an imperfection has not only to be strong but also it has to break the symmetry of the specimen.
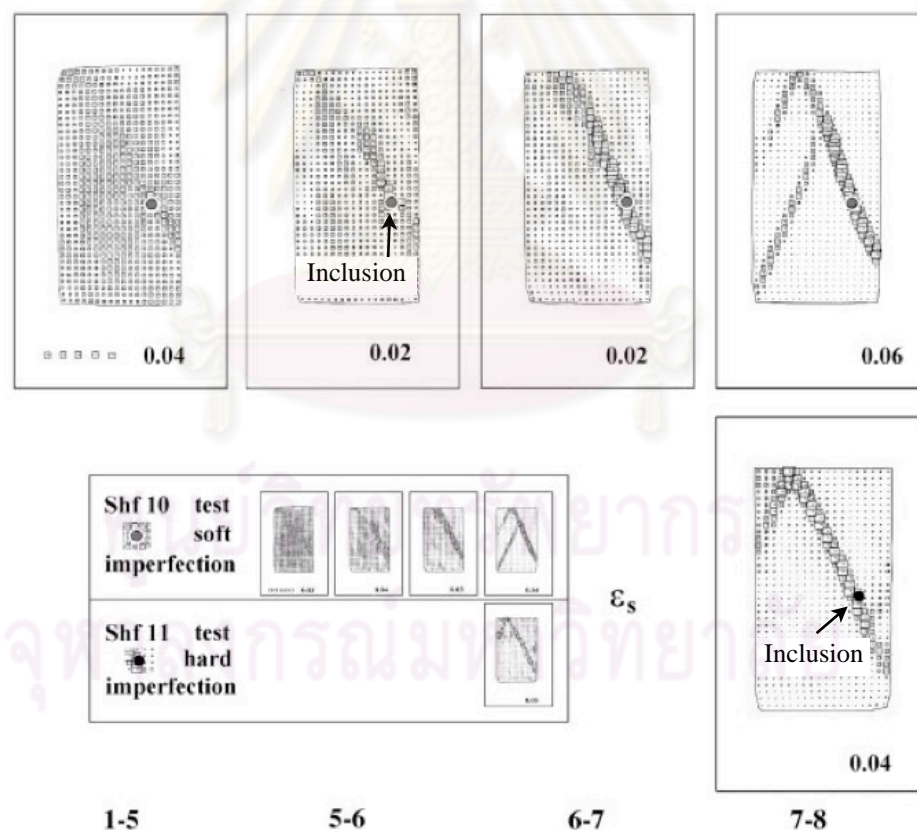
Fig. 2.29 Stereophotogrammetry-based incremental fields of shear strain intensity for soft (top row) and hard (bottom row) imperfection. (Desrues, 2004)
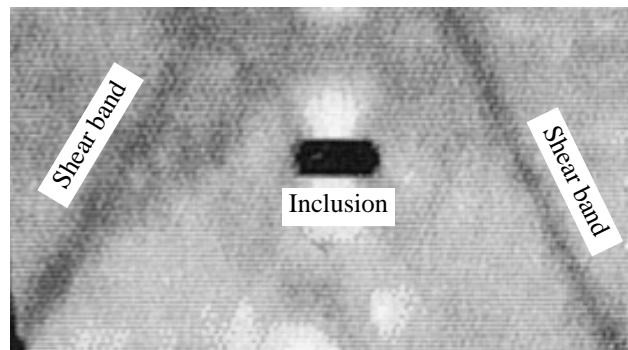
Fig. 2.30 Reconstruction of void ratio field in an axial tomogram of sand specimen: dark disc in the middle of the picture is a soft imperfection placed on the axis of the specimen; localization zones did not pass through the imperfection (Desrues *et al.* 1996)

2.3 Bender Element Test and Shear Wave Velocity in Particulate Materials

2.3.1 Bender element

The original concept of bender element application for geotechnical engineering was the work of Lawrence (1963 and 1965) who used piezoelectric crystals to generate one dimensional compression waves through sand and glass beads. Then, Shirley (1978) was the first to use piezoceramic bender element for generating and receiving shear waves in laboratory tests. Generally, bender element consists of two sheets of piezoelectric ceramic material such as lead, zirconate titanate, barium titanate, or lead titanate sandwiching a center shim of brass, stainless steel, or other ferrous nickel alloys to add strength to it (Fig. 2.31a). When a electrical voltage is applied to the bender element, the polarization will cause a bending displacement and, thus, the bender element acts as a signal generator. When the element is forced to bend, a voltage is generated and, thus, the bender element can act as a signal receiver. If one end is anchored, the other end generates a shear wave, or *S-wave* in the longitudinal direction of the crystal and compression or primary waves, *P-wave*, on the sides (Fig. 2.31b).

Over the years, bender elements have broadly employed in a number of geotechnical testing apparatuses. Bates (1989), Brignoli *et al.* (1996), and Pennington *et al.* (2001) measured shear wave velocity in triaxial specimens using peizoceramic

bender elements. Dyvik and Madshus (1985) measured small strain stiffness, G_{max}, of soil specimens in resonant column, odometer, and direct simple shear apparatuses using bender elements. Kawaguchi *et al.* (2001) measured G_{max}, in an odometer using bender elements. Agarwal and Ishibashi (1991) used bender elements in a triaxial cubical box device.
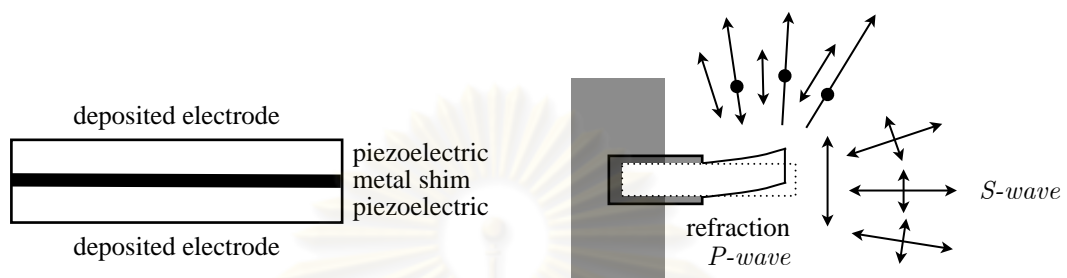
Fig 2.31 Bender elements (a) schematic representation of a bender element

(b) directivity: both *P*- and *S-waves* are generated (Lee and Santamarina, 2005)

Among the different types of piezoelectric ceramics, lead zirconate titanate (PZT) is the most common used. Depending on polarization, there are two types of bender element: x-poled and y-poled. From the energy point of view, there is no difference between x-poled and y-poled. Both the x-poled and y-poled bender elements act similarly when connected in a series connection and a parallel connection, respectively. The bender element types and connections can be illustrated in Fig. 2.32.
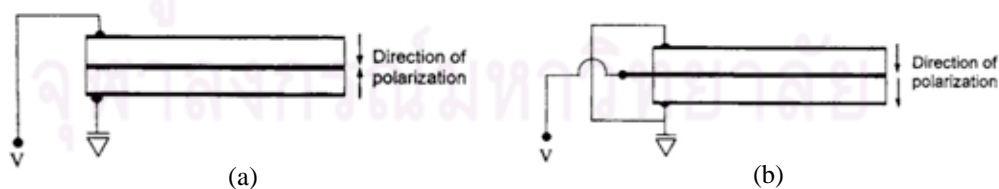
Fig. 2.32 Bender element types and connections (a) x-poled with series connection

(b) y-poled with parallel connection (Lee and Santamarina, 2005)

In the bender element test for shear wave velocity measurement, a pair of peizoceramic of bender elements is used. One of the elements acts as the shear wave

transmitter and the other elements acts as the receiver. A schematic diagram of the bender element system is shown in Fig. 2.33. By measuring the travel time of the wave, the shear wave velocity, V_s, is determined as follows:

$$V_s = \frac{L}{t} \tag{2.7}$$

where L is the tip-to-tip distance between transmitter and receiver of bender element and t is the travel time of the shear wave from transmitter to receiver (Fig. 2.34). Since L can be easily measured by a dial gauge attaching in the apparatus, the error in the shear wave velocity calculation is mainly due to an inaccuracy of travel time determination and interpretation.

(a)   (b)
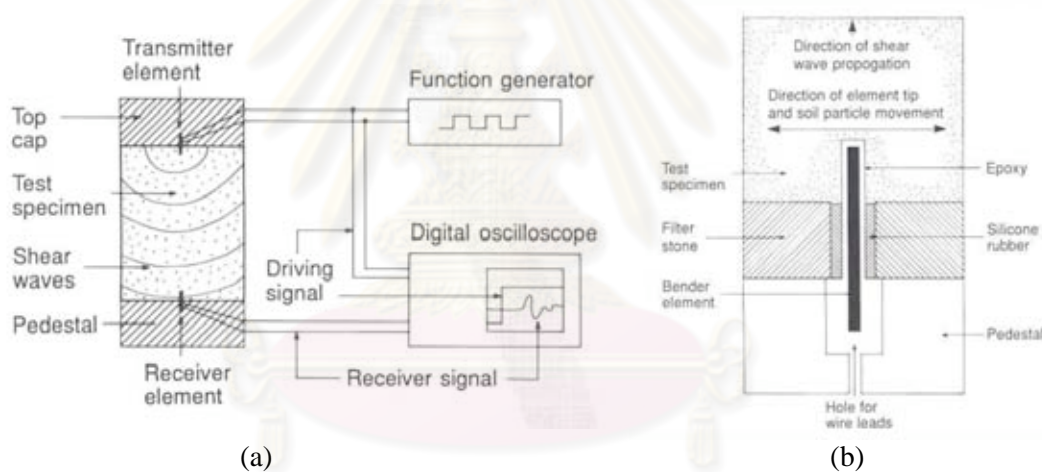
Fig. 2.33 Schematic of bender element system (a) setup of test equipment
(b) detail of bender element connection to soil sample
(Piezoceramic bender element test data sheet of Norwegian Geotechnical Institute, NGI)

2.3.2 Travel time determination

Based on a number of previous works, it is generally accepted that the travel distance is the distance between the tip of two bender elements. However, there is considerable uncertainty regarding the determination of travel time. Various waveforms, such as sine and square waves, with various frequencies, have been recommended as an excitation signal. Also, various methods have been studied for

determining the travel time such as time of flight techniques, i.e. first arrival time, the travel time between the characteristic points, and a cross-correlation method, and phase-sensitive detection technique. The details of each method can be explained in the following sections.
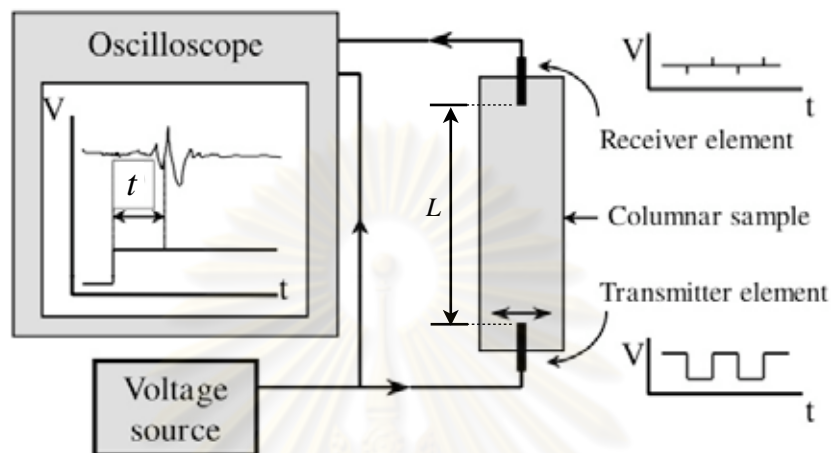
Fig. 2.34 Schematic representation of the conventional travel time measurement for shear wave velocity calculation (Blewett *et al.* 1999)

2.3.2.1 Time of flight techniques

The time of flight techniques use a single pulse as the transmitting signal. Initially, single square excitations have been used as seen in Fig. 2.35a. Many authors have then reported the difficulty in identifying the exact time of arrival signal. Thus Viggiani and Atkinson (1995) suggested the use of a single-shot sinusoidal excitation pulse, shown in Fig. 2.35b, to identify the points of similarity between the input and output waveform. Three different methods of travel time interpretations were generally used in order to find the times of travel from source to receiver. A detailed description of these three methods is provided below.

- First time of arrival

Kumar and Madhusudhan (2010) described that the first time of arrival, t_0, is the different time between the source signal and the receiver signal. In the case of the *S-wave* measurement, the initial weak signal for the receiver was found to be present in all the cases as indicated in Fig. 2.36a; this weak signal indicates the

presence of the near field effect. On the other hand, in the case of the *P-wave* measurements, the arrival of the receiver wave was quite distinct and there was no presence of any initial weak signal at all; see for instance Fig. 2.36b.
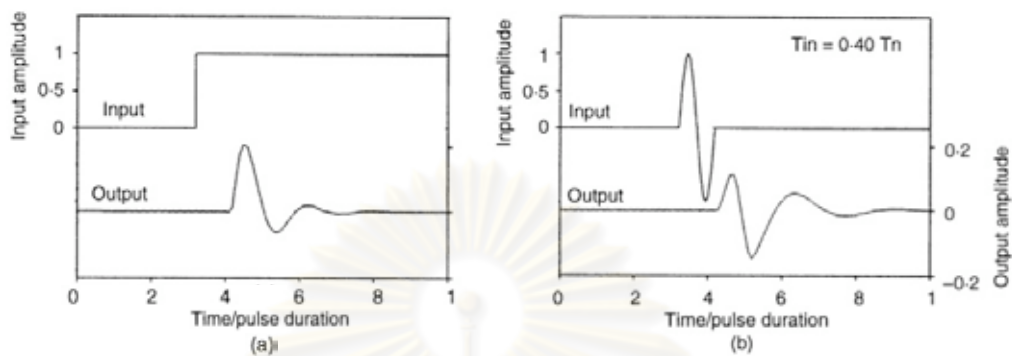
Fig. 2.35 Input pulse of shear wave (a) single square excitation
(b) single-shot sinusoidal excitation (Viggiani and Atkinson, 1997)
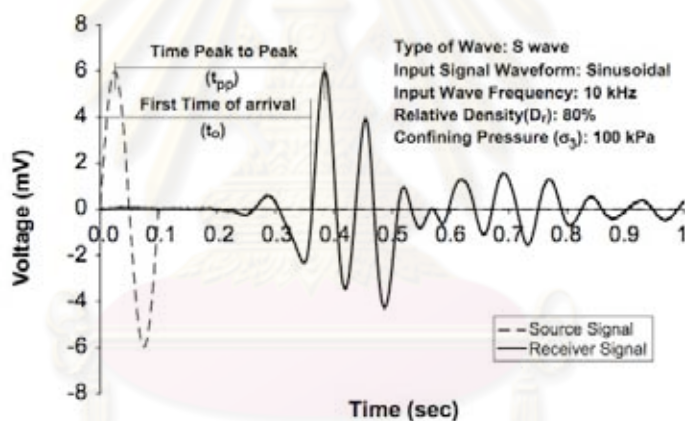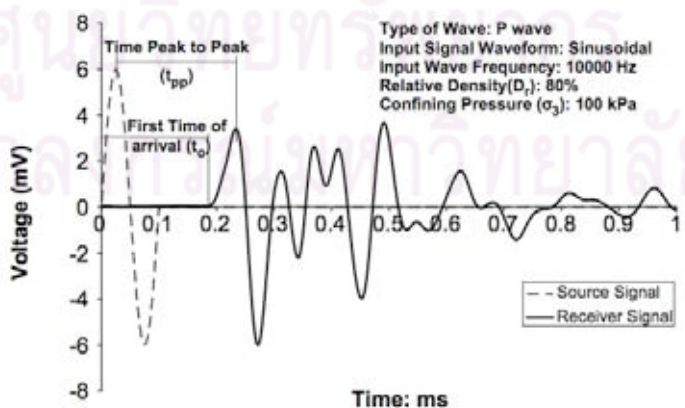
Fig. 2.36 First time of arrival (t_0) and the time between first peak to peak (t_{pp}) with $D_r = 80\%$ and $\sigma_3 = 100$ kPa (a) with *S-wave* and (a) with *P-wave* (Kumar and Madhusudhan, 2010)

- Travel time between characteristic points

Travel time of shear wave can be taken as the time between two corresponding characteristic points in the single sinusoidal input signal and the output signals. The most commonly used characteristic points are the first peak, first trough, or the zero crossing of the input and output signals. The measurement point, i.e. first peak to peak (t_{pp}), of this technique can be shown in Fig. 2.36a and 2.36b.

- The cross-correlation method

Travel time of the shear wave can be taken as the time shift (t_{cc}) that produces the peak correlation between a single sinusoidal input signal and the output signals. This method is the method which produces the most accurate shear wave velocity results since this method eliminates the ambiguity from visual estimations of other methods. The cross-correlation function $CC_{yx}(t)$ is a measure of the correlation between the receiver signal, $X(t)$ and source signal, $Y(t)$ versus the time shift (τ):

$$CC_{yx}(\tau) = \lim_{\tau \to \infty} \frac{1}{T} \int_{T} X(t)Y(t+\tau)dt \tag{2.8}$$

where T is the total duration of the time record. Typical results with the use of the cross-correlation method are shown in Figs. 2.37a and 2.37b with reference to the propagation of the *S-* and *P-waves*, respectively.

2.3.2.2 Phase-sensitive detection

Blewett *et al.* (1999) explained in their paper that phase-sensitive detection is a standard instrumentation technique. A signal is emitted at a particular frequency. This signal is then combined with noise during its transit to a detector, and then undergoes further degradation before arriving at the final measuring or display device. Even though the signal is now a mixture of many frequencies, the user is usually interested only in that part of the signal at the original emission frequency. A conventional lock-in amplifier can be used just before the final device. This amplifier is fed an electrical copy of the drive signal and derives a reference frequency from it.

The amplifier is also fed the received signal. By multiplication and filtering, the lock-in amplifier extracts information about the strength of the component in the received signal which occurs at the reference frequency. The system can be thought of as a tuneable filter, whose output is usually a direct-current signal proportional to the strength of the reference frequency component within the input signal, as shown in Fig. 2.38.

(a)

(b)
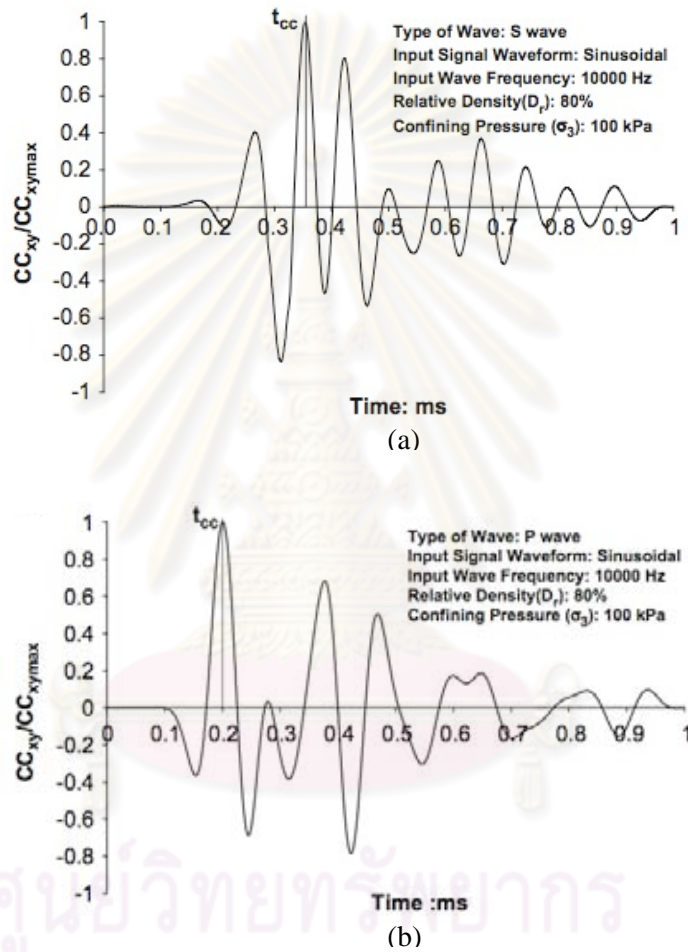
Fig. 2.37 The time of arrival using cross-correlation method (t_{cc}) with $D_r = 80\%$, $\sigma_3 = 100$ kPa

(a) with *S-wave* and (a) with *P-wave* (Kumar and Madhusudhan, 2010)

The relationship between the change in phase angle and travel time can be determined by:

$$dt = \frac{d\theta}{360f} \tag{2.9}$$

where *dt* is the change in time-of-flight in seconds, *dθ* is the change in phase angle in degrees, and *f* is the frequency of the driving wave in Hertz.

Depending upon the drive frequency used, small changes in time can result in multiple revolutions of the phase angle and therefore extreme sensitivity.
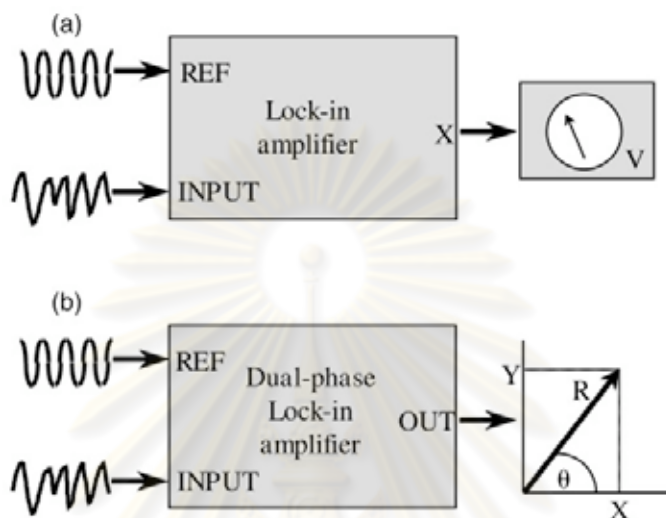
Fig. 2.38 (a) Representation of the lock-in amplifier as a tuneable filter. (b) representation of the output of the dual-phase lock-in amplifier as a vector (Blewett *et al.* 1999)

2.3.3 Potential problems in bender element testing

2.3.3.1 Near-field effect

The travel time of the *S-wave* can be taken as the first arrival of the receiver signal (Leong *et al.* 2005). Reversal of the received signal's polarity when the polarity of the transmitting element is inverted is often taken as the arrival of the *S-wave*. However, numerical studies by some researchers have shown that the first deflection of the S-wave signal may not correspond to the arrival of the *S-wave* but to the arrival of the so-called "near-field" component, which travels with the velocity of the *P-wave*. In addition, inverting the polarity of the transmitter element does not help to eliminate the near-field effect as it produces the reversal of all the waveform components including the near-field components.

Sanchez-Salinero *et al.* (1986) showed that the *S-wave* signal is always accompanied by the propagation of another signal of opposite polarity that travels

with the velocity of the *P-wave*. In other words, the bender element that produces mainly shear displacement will also generate a component that travels at the *P-wave* velocity. This phenomenon is known as the near-field effect, which is quantified in terms of the ratio of wave path length (L_{tt}) to wavelength (λ), L_{tt}/λ. The near-field effect amplitude decays rapidly with increasing number of wavelengths between the transmitter and the receiver element.

Jovicic *et al*. (1996) indicated that the near field effect can be lessen down by increasing the frequency of the input signal. In the literature, most of the bender elements tests have been done at a frequency lesser than 10 kHz. Kumar and Madhusudhan (2010) also concluded that the extent of the near-field effect signal clearly reduces with an increase in the frequency of the input signal. The near-field characteristic of shear wave signal at different frequencies can be displayed in Fig. 2.39.
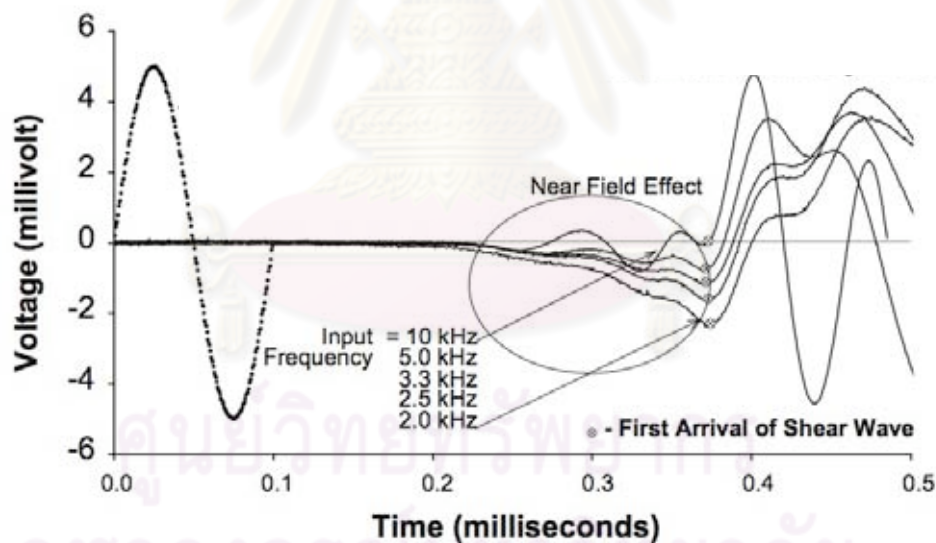
Fig. 2.39 Near-field effect of received shear wave signals at different frequencies
(Kumar and Madhusudhan, 2010)

2.3.3.2 Electromagnetic coupling - crosstalk

Lee and Santamarina (2005) explained in their work that electromagnetic coupling between source and receiver bender elements manifests as an output signal with an early component that is quasisimultaneous with the input signal. This

"crosstalk" can be very important in wet soils. Fig. 2.40a shows typical crosstalk effects observed with two series-type bender elements without grounding; the received signal resembles the discharge of a capacitor. Crosstalk can be effectively removed by grounding either the source or the receiver (Fig. 2.40b). The outer electrodes in a parallel-type connection have a shielding effect when connected to ground. Still, crosstalk can be observed in the series-to-parallel combination when the series element is not shielded and grounded (Fig. 2.40c). Crosstalk vanishes when two parallel-type bender elements are used (Fig. 2.40d).
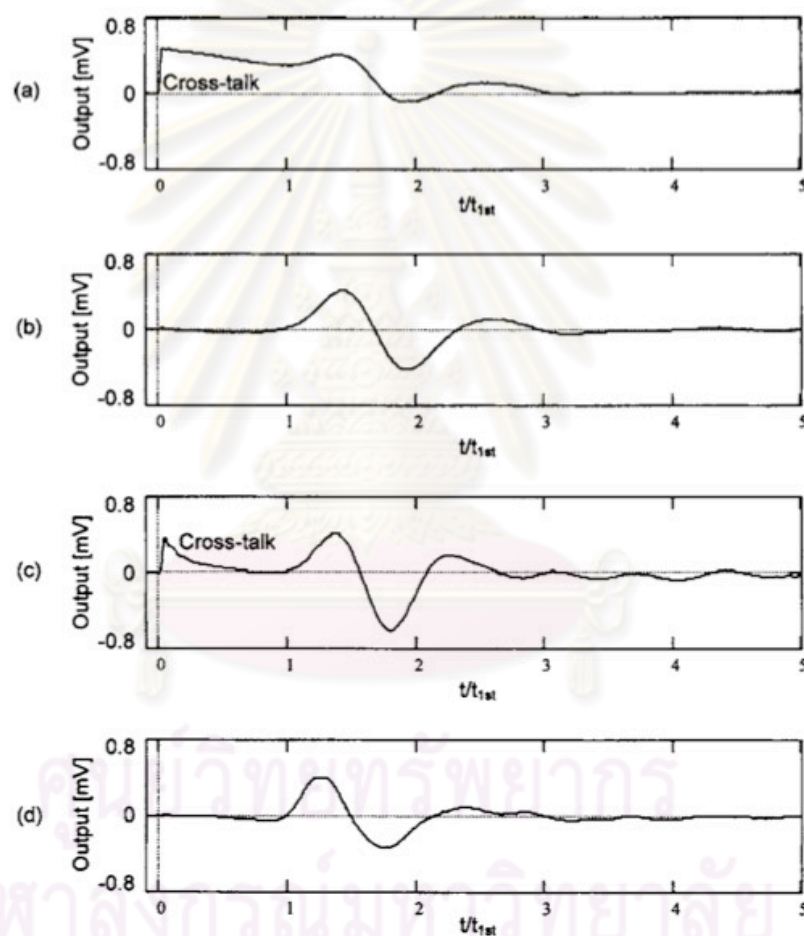
Fig. 2.40 Crosstalk effects: (a) series-to-series without grounding; (b) series-to-series with shielding and grounding; (c) parallel-to-series without shielding and grounding; and (d) parallel-to-parallel without shielding. Time "t_{1st}" corresponds to *S-wave* first arrival (input: step signal, tip-to-tip distance: L = 100 mm) (Lee and Santamarina, 2005)

2.3.3.3 Time or phase lag

The transfer functions relating the physical wave forms to the measured electrical signals introduce significant phase or time lags that are different at the transmitting and receiving benders. The time lag of the system as a whole can be measured by putting bender elements for generating and detecting waves in direct contact with each other. This calibration method was originally proposed by Dyvik and Madshus (1985), who found a nil time lag for small bender transducers. This method was later used by others, e.g. Gajo *et al.* (1997), who found a time lag of 5 μs and 2.8 μs for larger benders.

2.3.3.4 Wave interference and reflection at rigid boundaries

Arulnathan *et al.* (1998) performed bender element tests to investigate how the interference of incident and reflected waves at rigid boundaries can affect the determination of travel time. The transmitter and receiver caps are assumed to be perfectly rigid boundaries and finite elements analyses were done. The results of the finite elements model shows that the correct travel time can be obtained when the ratio of bender separation L to wave length λ is more than or equal to 1/4. In other words the wave length λ must be less than or equal to $4L$, or that there must be at least a quarter wave within the sample separation L. As L/λ decreases below 1/4, travel times are progressively underestimated, and hence shear wave velocity overestimated.

CHAPTER III

Methodology

3.1 Material Properties

There were two types of sand samples in this study. The first sand sample was taken from the eastern region of Thailand in Chonburi province. The grain particle slightly varies from rounded to sub-angular shape with low sphericity. The sand samples were then sieved to separate the grain particle to be in various dimensions. The sand particles resting on the sieve number 16 and 40 of U.S. standard size which has the opening equal to 1.18 and 0.425 mm., respectively would be selected as the test samples in the experiments. These uniformly graded sand samples will be called later by D16 and D40. The second sand sample was the commercial standard Silica test sand which has the well rounded shape of grain particle with high sphericity. This Silica test sand conforms to the ASTM C-778 #20 - 30. The mean size particle, d_{50}, is approximately 0.60 mm. The shape of grain particle of entire test sands can be shown in Fig. 3.1. To clearly observe the particle shape, the photo effect from the photo editing software was carried out. The results of that effect can be displayed in Fig. 3.2.

The basic engineering properties of sand samples shows in Table 3.1. It should be note that because of the low to medium sphericity and angular shape of each particle the mean size number (d_{50}) of D16 and D40 samples was the average value for the whole grain. The sample, after sieving, was washed out by clean water and the moisture was dried out in the electronic oven before the experiment.

3.2 Sample Preparation

Though, it is significantly understood that the sample preparation techniques for such a test of cohesionless materials can greatly influence the tested results. However, these types of preparation methods have their own advantages and disadvantages. For example, moist tamping method, though easy to perform, might

partially produce very loose to dense conditions of sample which consequently make a nonuniform specimen regarding of its entire density or particle size gradation. The air pluviation technique produces fairly uniform specimens depending upon the technique used. A higher drop height results in a higher energy of deposition and thus a denser soil specimen. Nevertheless, air pluviation of well-graded sand is not suitable because well-graded sand may become segregation when deposited by pluviation through air, especially if it has a considerable amount of fine contents. On the other hand, the influence of this segregation of well-sorted or uniformly graded sand is quite small.

Figure 3-1 Shape of grain particle of (a) D16, (b) D40 and (c) Silica test sand.
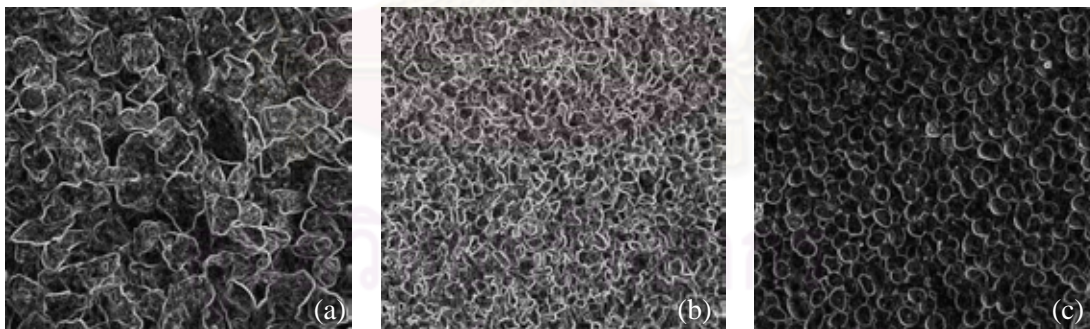
Figure 3-2 The photo effect of grain particles of (a) D16, (b) D40 and (c) Silica test sand.

In this study, the air pluviation technique was adopted because of the uniformity of the test sand particles and to prevent the separation between each layer in the composition procedure due to the difference in compaction energy of tamping method. Creating and maintaining a uniform sand rain during specimen reconstitution is really crucial because this is the main characteristic of pluviation and controls the uniformity of fabric and density. Five layers of test sand sample would be

consecutively dropped from a funnel with a constant height depending upon the required density of the specimen. Namely, the higher the drop of sand rains, the higher the density of the specimen. To prepare for very loose to loose conditions of the specimen, the nearly attached distance between the edge of the funnel and the reconstituted specimen, or null drop height, would be done. On the other hand, the medium to dense state would be performed by larger gap between the funnel and the top of the sand layer, i.e. about 5 - 8 cm. high. Moreover, to be certain that the desire relative density (D_r, %) would be acquired, the amount of the test sands would be calculated and weighted according to their basic engineering properties, e.g. minimum and maximum void ratio, specific gravity and dry density as in equations 3.1 and 3.2. The qualitative description of granular soil deposited into a specimen would follow Table 3.2.

Table 3.1 The basic engineering properties of sand samples

Basic property	D16	D40	Silica sand
Shape of grain particle	Low to medium sphericity with angular shape	Low to medium sphericity with angular shape	High sphericity with well rounded shape
Mean size particle, d_{50} (mm)	1.18	0.465	0.60
Specific gravity, G_s	2.69	2.72	2.65
Maximum void ratio, e_{max}	1.06	1.12	0.6
Minimum void ratio, e_{min}	0.713	0.808	0.459

$$e = \frac{G_s}{\rho_d} - 1 \qquad (3.1)$$

where e is the actual void ratio, G_s is the specific gravity of soil, ρ_d is the dry density

$$D_r(\%) = \frac{e_{max} - e}{e_{max} - e_{min}} \times 100\% \qquad (3.2)$$

where D_r is the percentage of relative density and e, e_{max} and e_{min} is the actual void ratio, maximum void ratio and minimum void ratio, respectively.

According to the literature, i.e. Desrues *et al.* (1996) and Desrues and Viggiani (2004), about the slenderness ratio of the sample, this study attempts to stay away from the unusual results form the triaxial tests. Desrues *et al.* (1996) could observe the complex patterns of shear band in a relatively short specimen, e.g. slenderness ratio = 1.0. However, in a long specimen, i.e. slenderness ratio = 1.94, the shear band exhibits itself in a form of single unique plane. They finally reported that the slenderness ratio greatly influences the strain localization in sand. Therefore, to avoid the complex pattern of shear band as well as some undesirable outcomes, the dimension of the specimen would be maintained to have the appropriate slenderness ratio; about 2.0. The typical height and width varied between 11.20 - 11.80 cm and 4.80 - 4.95 cm, respectively. The slenderness ratio, *H/D*, is therefore approximately 2.30 - 2.45.

Table 3.2 Qualitative description of granular soil deposits

Relative density (D_r, %)	Description of soil deposits
0 - 15	Very loose
15 - 50	Loose
50 - 70	Medium
70 - 85	Dense
85 - 100	Very dense

It should also be noted that to reduce the friction effect between the specimen and the top / bottom end platens (filter paper), the silicon grease should be lubricated on the surface of both ends every time prior to the test.

3.3 Bender Element

Depending on polarization, there are two types of bender element: series-type (x-poled) and parallel-type (y-poled). From the energy point of view, there is no difference between x-poled and y-poled bender elements. The bender elements used in this study were both series- and parallel- types. The parallel-type bender element

was used as a source and the series-type bender element as a receiver because the parallel-type connection gives twice the displacement of the series-type connection (Lee and Santamarina, 2005). One of the most important aspects associated with the use of bender elements is the waterproofing of the elements. Since piezo-ceramics are high impedance devices that may short circuit when contact with moisture. Therefore, the waterproof material, i.e. epoxy glue, was entirely coated to all surface of bender elements. The shielded wires were then connected with the bender element according to its type of connection. The shielded wires were used in order to minimize noise interfering with the signal.

The bender elements were then fixed into the slot of the top and bottom pedestals of the conventional triaxial apparatus by resin hardener. The protrusion of the bender element was 9.65 mm. for top cap and 9.80 mm. for top bottom cap. The schematic view of the installation of bender element in the pedestals can be shown in Figure 3.3.
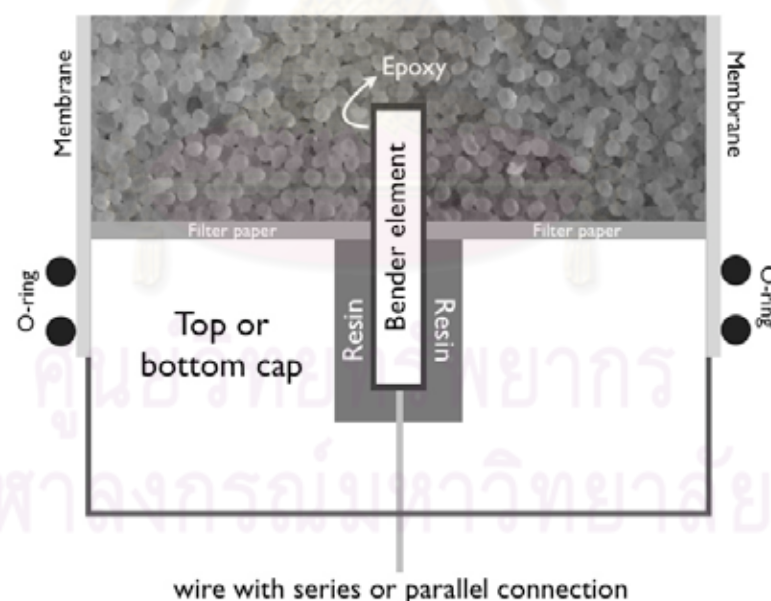
Figure 3.3 The installation of parallel- or series-type of bender element
in the top / bottom cap of the triaxial apparatus

3.4 Digital Image Analysis (DIA)

Nowadays, DIA techniques are very powerful for gathering information to study the fabric and deformation of granular materials in geotechnical engineering. In the study of localization and shear band in soil sample, one of the simple and extensively used methods is the visual observation from the deformation profiles of the sample surface, i.e. membrane surface. Though, this technique cannot be used for the microscopic study of the deformation and failure mechanisms but can use to some extent to measure the thickness and inclination angle of the shear band. The series of square grid or dot will be imprinted on the membrane surface and the images will be captured by high resolution digital camera or video camera.

In this study, the surface of membrane would be lined by a waterproof and permanent pen. The dimension of these blue square grids is 5 x 5 mm. Figure 3.4 shows the square grid pattern of the specimens. The high resolution image, 2848 x 2136 pixels, was acquired by Fuji Finepix S6500fd digital camera. A series of image captures would be performed before, during and after the compression test. The digital camera was mounted on a camera stand in the fixed position for the entire process. It should be note that during the triaxial compression test, the images of the sample would be taken in every 0.5 mm. of axial deformation. When the axial strain is approximately more than 10% or when the shear band is obviously developed, the last snapshot of the failure specimen would be performed. However, because of the unpredictable zone of the localization inside the failure sample in the triaxial test, the suitable plane of the failure sample would be selected for a final shot of the image.

3.5 Triaxial Compression Test by Vacuum Technique

Due to the necessity of shear band observation by DIA, the conventional triaxial compression test by applying water pressure as a sample confinement will interfere the snapshot of specimen pictures during the test. Therefore, the triaxial compression test by vacuum technique would be adopted in all tests. The confining pressure was obtained by applying an internal vacuum inside the specimen, without a confining cell. However, the vacuum capacity is very limit, i.e. about 90 kPa.

Therefore, in this research, the maximum isotropic confining pressure would be around 80 kPa. Before filling the test sands into the mold for constituting the specimen, the partially vacuum pressure, e.g. 8 - 10 kPa, was applied to help smoothing the membrane attaching inside mold surface and to support the constituted specimen after disassembling of the mold. Any of the test procedures are similar to the conventional triaxial test. All of triaxial compression tests will be in dry condition. No pore water pressure and volume change would be measured and recorded.
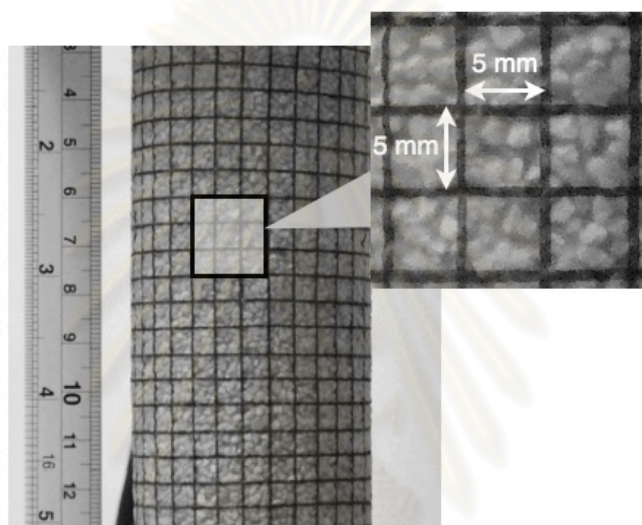
Figure 3.4 The printed square grid on the rubber membrane surface of the specimens
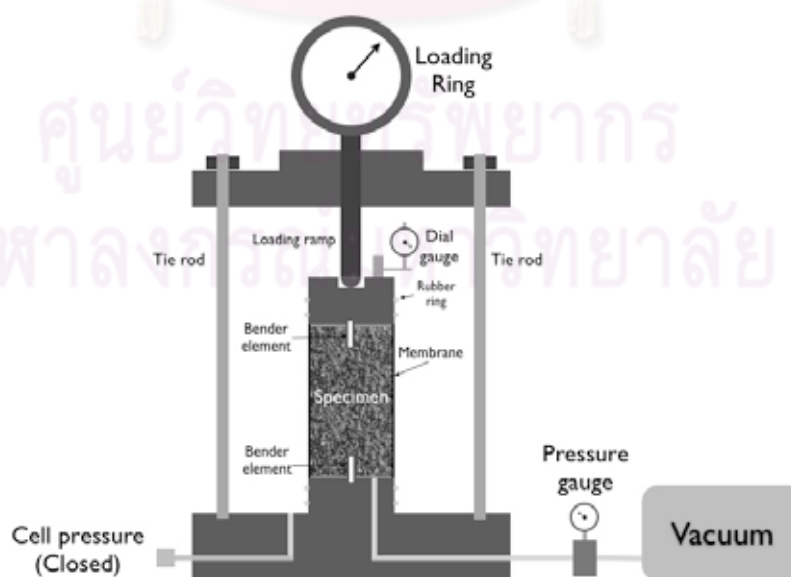
Figure 3.5 The schematic view of triaxial testing by vacuum technique

3.6 Experimental Works

The major apparatuses required in this research are;

1) Conventional triaxial compression apparatus modified to accommodate the bender elements

2) Bender elements installed in the top cap and pedestal of triaxial device

3) Oscilloscope and signal data acquisition software

4) Function generator (square wave trigger)

5) High resolution digital camera and stand

6) Computer

The schematic view of the bender element test setup incorporated in a triaxial cell apparatus can be shown in Figure 3.6.
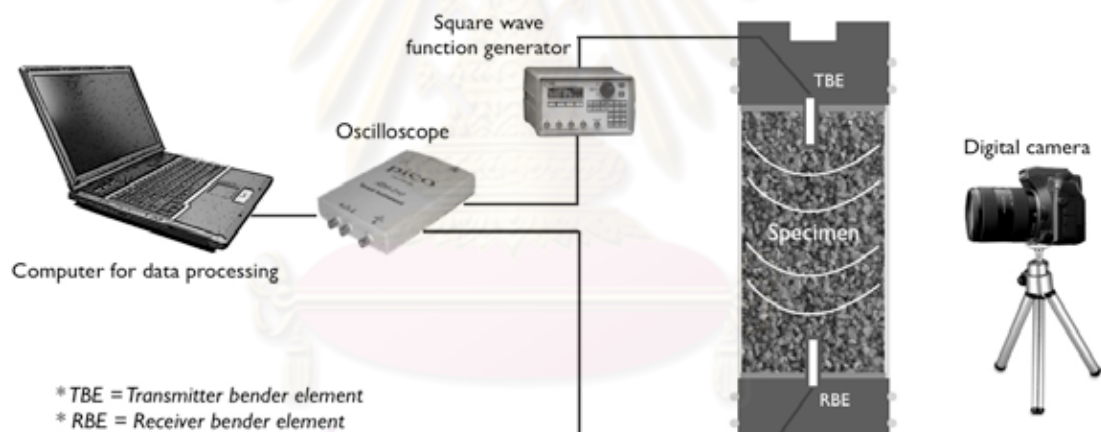
Figure 3.6 The schematic view of the bender element test setup
incorporated in a triaxial cell apparatus

The commercial digital oscilloscope model, ADC-212, and wave data acquisition software by Pico Technology Limited was employed in the experiments. Because of many electrical devices e.g. personal computer and oscilloscope, used in the testing system, the ground of every apparatus was connected directly to the ground of the computer to minimize interference. The square wave function generator was connected to the oscilloscope and the transmitter bender element. The oscilloscope would then analyze the signal of both transmitter and receiver signals

and transferred theses signals to the data acquisition software in the computer for further signal processing. These data would be stored for future calculation and numerical analysis of V_s traveling inside the specimen. The figure of the transmitter square wave and received wave from the software shows in Fig 3.7.
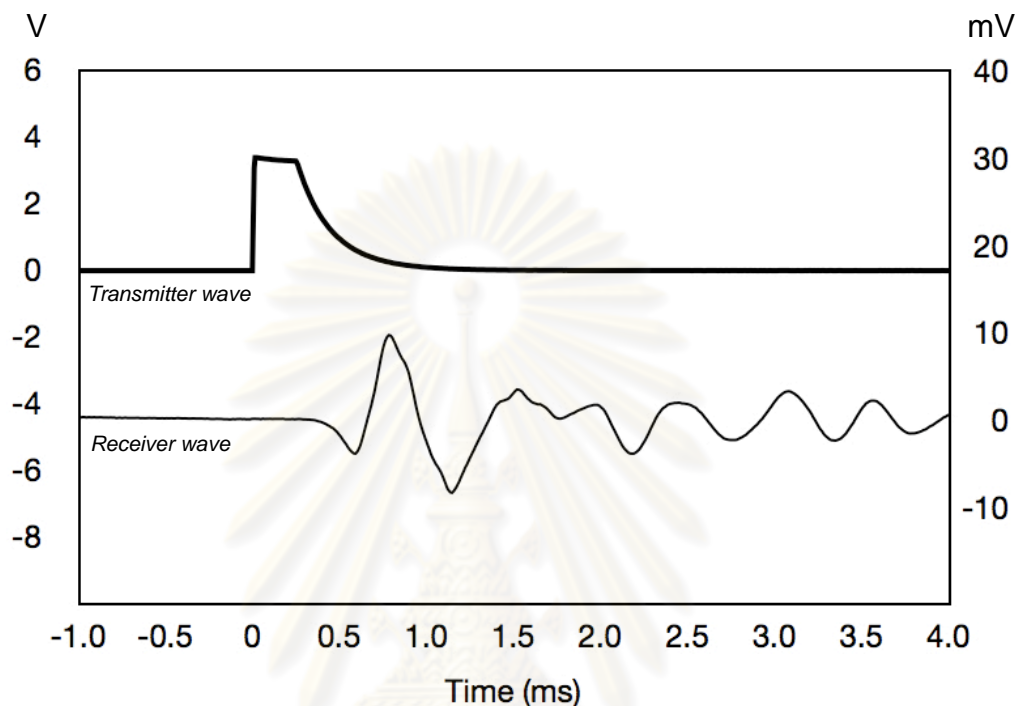
Figure 3.7 The graphical display of typical transmitter and receiver wave
from oscilloscope processing

Before starting any triaxial compression tests, the entire system would be calibrated to correct some existing errors of the travel time and shear wave measurement as well as to minimize the interference from the noise of the surrounding apparatuses. It was found that the received signal was alway intervened by the nearby electrical devices. The appropriate grounding of all devices should be carefully performed.

The triaxial tests would be carried out with the vacuum confinement of 25, 50 and 80 kPa. Three types of test sand, i.e. D16, D40 and silica were reconstituted into various conditions, e.g. very loose, loose, medium and dense state. It should be note that the cases of very loose and medium condition were tested only for silica sand. The measurement of shear wave travel time and the snapshot of specimen before,

during and after testing would be performed and saved into the computer for further analyses. It should be noted that during the triaxial compression test, the loading machine would be momentarily halted, i.e 1-2 seconds, in every 0.5 mm of axial deformation while the specimen image was being captured by digital camera at its surface membrane. Although, this action might somewhat influence stress-strain relationship of the test but can considerably minimize the interference signal and vibration from the electrical motor machine.

The data of axial loading from proving ring and the axial deformation from dial gauge would also be recored to observe the stress-strain relation of the sample. This stress-strain relation can explain to some extent the initiation of the shear band or localization inside the sample under triaxial test.

Summary of testing and specimen conditions can be shown in Table 3.3 and the schematic chart of testing procedures can be shown in Figure 3.8

3.7 Calculation of Travel Time and Shear Wave Velocity

To calculate the shear wave velocity, V_s, traveling between transmitter and receiver bender elements, a conventional equation as in 3.3 is widely used among the researchers.

$$V_s = \frac{L_{tr}}{t} \tag{3.3}$$

where L_{tr} is the distance between tip of transmitter to receiver bender element and t is the traveling time (time-of-flight) of shear wave from transmitter to receiver bender element. Though this equation can easily calculate the V_s propagating throughout the soil specimen but the determination of t is still ambiguous. There are many controversial methods, e.g. first deflection, first bump maximum, zero crossing after first bump, and major first peak, to determine the first arrival time of propagated shear wave inside soil sample by using the bender elements.

Viggiani and Atkinson (1995) concluded from the numerical analyses that the travel time of the signals from bender elements tests on a reconstituted boulder clay

sample should not be taken as the time corresponding to the first deflection of the received signal. The travel time corresponding to the first inversion of the received signal is more accurate.

Table 3.3 All testing conditions and specimen properties of this study

Sand	Confining pressure (kPa)	Relative density		Specimen dimension			Image capture
				H (cm)	$D*$ (cm)	Slenderness ratio (H/D)	
D16	25	43.75%	Loose	11.49	4.79	2.39	Yes
		80.98%	Dense	11.80	4.81	2.45	Yes
	50	47.26%	Loose	11.22	4.82	2.32	Yes
		73.09%	Dense	11.67	4.86	2.40	Yes
	80	38.78%	Loose	11.22	4.87	2.30	Yes
		75.66%	Dense	11.54	4.87	2.37	Yes
D40	25	28.65%	Loose	11.27	4.81	2.34	Yes
		79.32%	Dense	11.35	4.85	2.34	Yes
	50	39.85%	Loose	11.21	4.79	2.34	Yes
		81.60%	Dense	11.45	4.82	2.37	Yes
	80	32.48%	Loose	11.27	4.95	2.27	Yes
		81.58%	Dense	11.67	4.78	2.44	Yes
Silica	25	13.58%	Very loose	11.51	4.91	2.34	Yes
		56.83%	Medium	11.50	4.90	2.35	Yes
	50	38.99%	Loose	11.44	4.82	2.37	Yes
		77.09%	Dense	11.19	4.87	2.29	Yes
	80	22.77%	Loose	11.49	4.87	2.35	Yes
		60.66%	Medium	11.44	4.89	2.33	Yes

$$* \quad D = \frac{D_{top} + 2D_{middle} + D_{bottom}}{4}$$
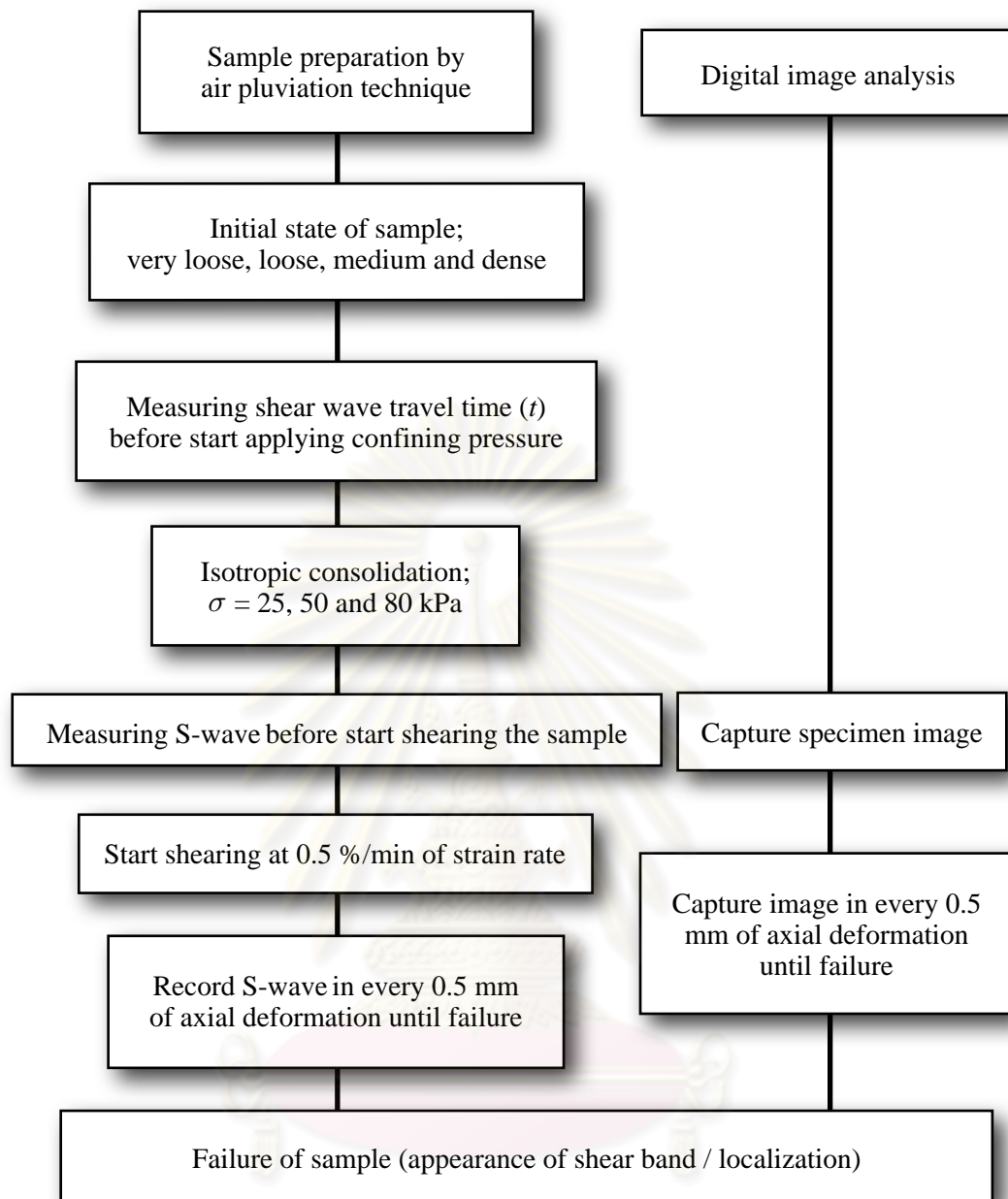
Figure 3.8 The schematic chart of all testing procedures

Leong *et al.* (2005) compared the travel time of a mudstone residual soil specimen at a confining pressure of 800 kPa. between the ultrasonic test and conventional bender element tests. The travel times for both the bender element test and the ultrasonic test are the same only if the first deflection of the receiver signal was used for the bender element test.

Lee and Santamarina (2005) described various techniques to determine the first arrival time between source and receiver bender elements as in Figure 3.9. They

also demonstrated that suggested criteria and recommendations to measure this first arrival time vary depending installation, application and input signal.
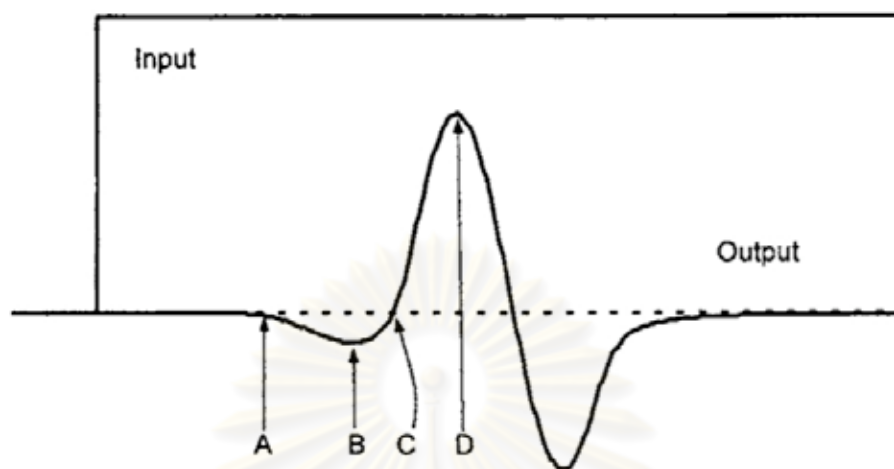
Figure 3.9 Typical *S-wave* signal within near field A) first deflection, B) first bump maximum, C) zero after first bump, and D) major first peak
(Lee and Santamarina, 2005)

Therefore, it can be discerned from those previous reports that the method to choose the first arrival time of received signal to calculate for V_s slightly varies among the past experiments. There are a number of reasons which make this traveling time calculation complicated, for example, the interference between *P-waves* and *S-waves* (shear wave) at the first part of the received signal, the excitation frequency of the input signal as well as the near field effect. The *P-waves* which are also generated from the transmitter bender element generally reflect from the cell wall and always arrive earlier than the shear wave. Therefore, these reflecting *P-waves* will mainly disguise the interpretation of the first arrival time of the shear wave. The near field effect is usually occurred in short specimen and when L_{tr}/λ is less than 2. This effect will decrease as L_{tr}/λ increases (Sanchez-Salinero *et al.*, 1986 and Brignoli *et al.*, 1996) where λ is the wavelength of the shear wave.

In this research, because of a broad range of shear wave velocity determination in one test, i.e. from zero strain to failure, the variation of stress state and void ratio during shear will certainly affect the shear wave propagation characteristic. At any certain strain level the near field effect as well as the reflecting

P-wave may dominate or diminish depending on that current state of the soil. As a result, the manual visualization and interpretation of captured high-resolution image of signal from oscilloscope processing to select the appropriate first point of shear wave arrival would be adopted to calculate the shear wave velocity propagating throughout the specimen. The influences of *P-Wave* and near field effect would be carefully accounted in the result interpretation. Figure 3.10 shows the interpretation practice to point out the first arrival time of shear wave transmitted from the source to the receiver bender element justified for the near field effect and reflecting *P-waves*. It can be seen that the position of line Y is approximately the same as point B (first bump maximum) in Figure 3.9 where line X is the starting time of generated signal of transmitter bender element. The traveling time, *t*, will be the different between line X and Y. Figure 3.11 shows the effect of the near field and reflecting *P-waves* of the receiver signal.
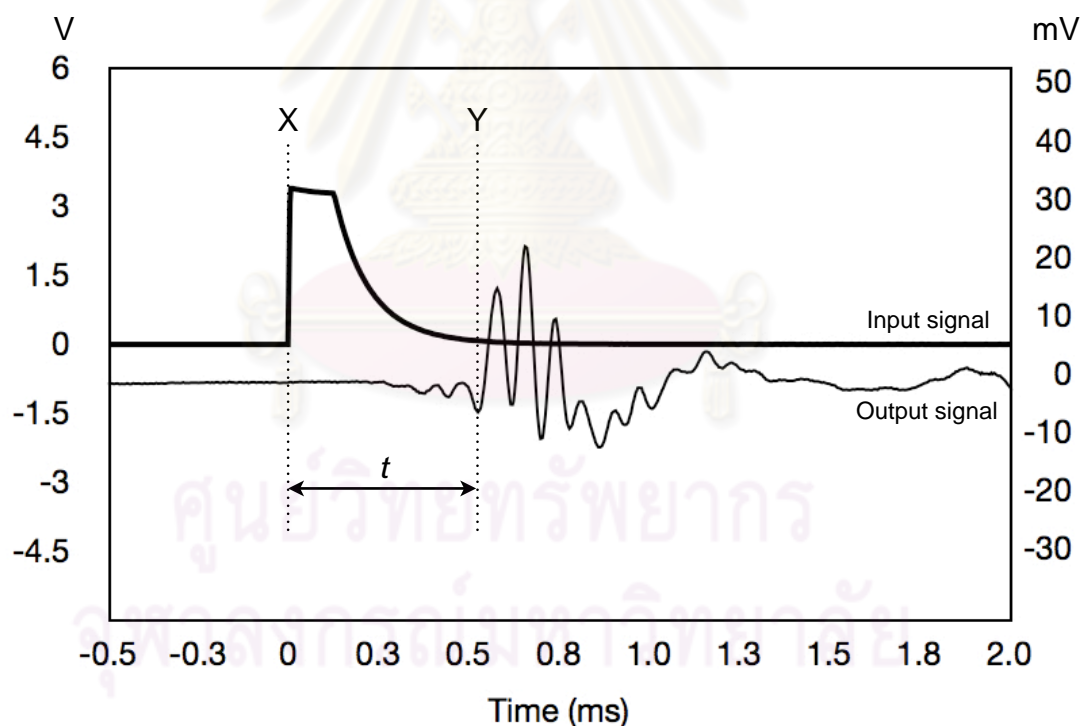
Figure 3.10 The interpretation method to point out the first arrival time of shear wave justified for the near field effect and reflecting *P-waves*.

First deflection

Zero line

Near field effect with reflecting P-Wave
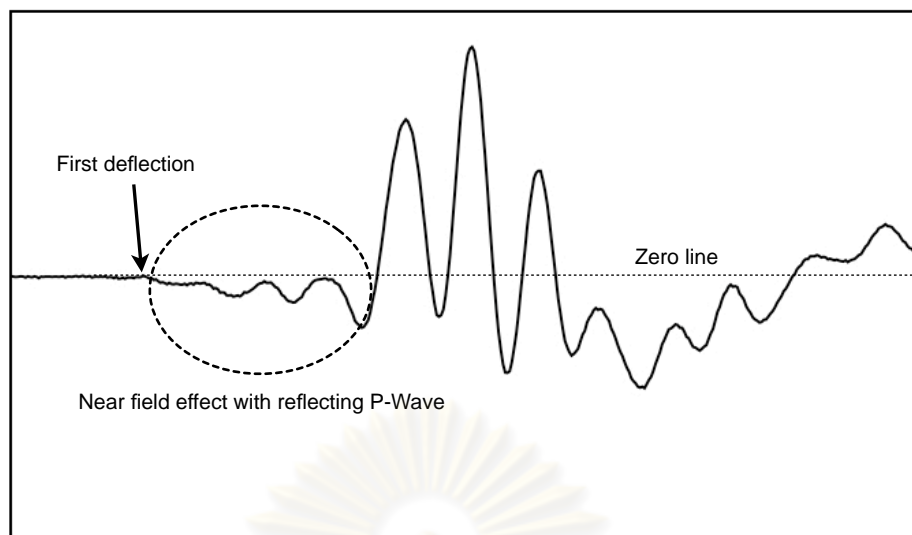
Figure 3.11 The effect of near field and reflecting *P-wave* of the receiver signal.

CHAPTER IV

Results and Analyses

4.1 The Stress Strain Responses from Triaxial Tests

It is widely recognized that the global stress-strain response during compression of a sand is dependent upon the initial density and initial mean effective stress. At a given stress level, initially dense specimens of sand will expand when sheared, while initially loose specimens will contract. The stress strain relationship from all tests; very loose, loose, medium and dense state with the confining pressure of 25, 50 and 80 kPa on D16, D40 and Silica test sand can be shown in Figure 4.1 - 4.3. It can be seen that the higher the confining pressure the higher the load carrying capacity of the soils. The abrupt drop of stress-strain curve after peak strength level could be observed in the dense specimens while there was no such sharp peak in the samples of loose condition. This stress drop always followed by the so-called softening behavior. This observed softening after each peak is a consequence of bifurcation instability in the vicinity of the peak. Dense specimens normally reached the peak state at the strains of about 2 - 5% depending on the initial condition of confining pressure. Namely the relatively high confining pressure slightly delayed the peak strength of the stress - strain response of the soils. The ultimate state would be generally reached after strains greater than 10%. On the other hand, most of the test sands in loose condition, especially with low confining stress, would compress throughout, shearing up to the ultimate state, no dominant peak could be observed. However, in a high confining stress, i.e. 80 kPa, some specimens exhibited a peak shear stress but the difference between this peak shear stress and corresponding ultimate stress was not as large as in the dense sample.

These observed behaviors are typical for loose and dense sands or normally consolidated and overconsolidated clays. Though this study did not measure the volumetric strain of the specimen, however, it could be recognized that sand in loose condition compresses as shear stress increases while sand in dense condition dilates

after a small compression. Because of the comparatively round shape of the grain, the Silica test sand has the smaller shear strength and starts failing at lower strain than D16 and D40 which have the angular shape of grain particle at the same packing condition and confining pressure. The somewhat round particle can easily rotate as well as slide when subjected to the surrounding pressure. However, Silica test sand shows the greater strain of ultimate strength compared to the other sands at the same initial state. The summary of the test results in terms of stress - strain value can be shown in Table 4.1.
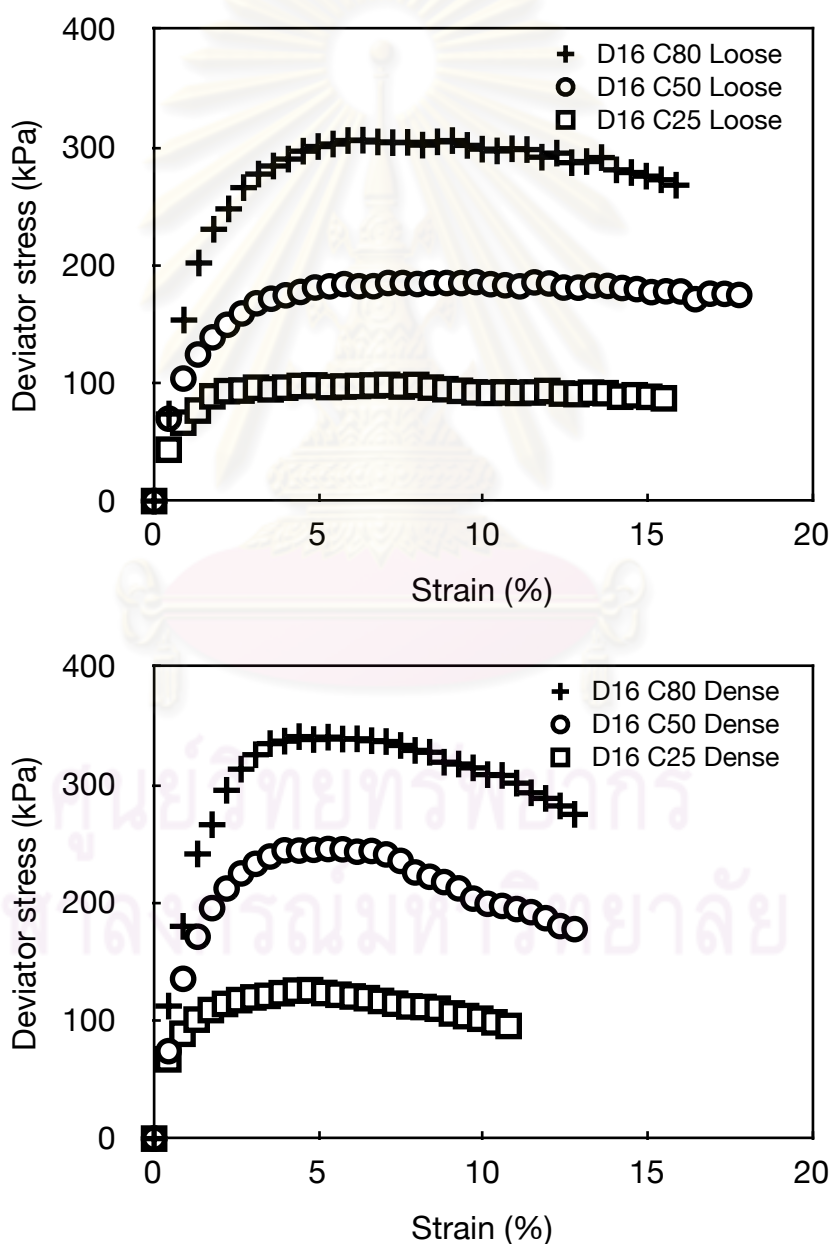
Figure 4.1 The stress - strain relation of D16 specimen in loose and dense conditions with confining pressure 80, 50 and 25 kPa
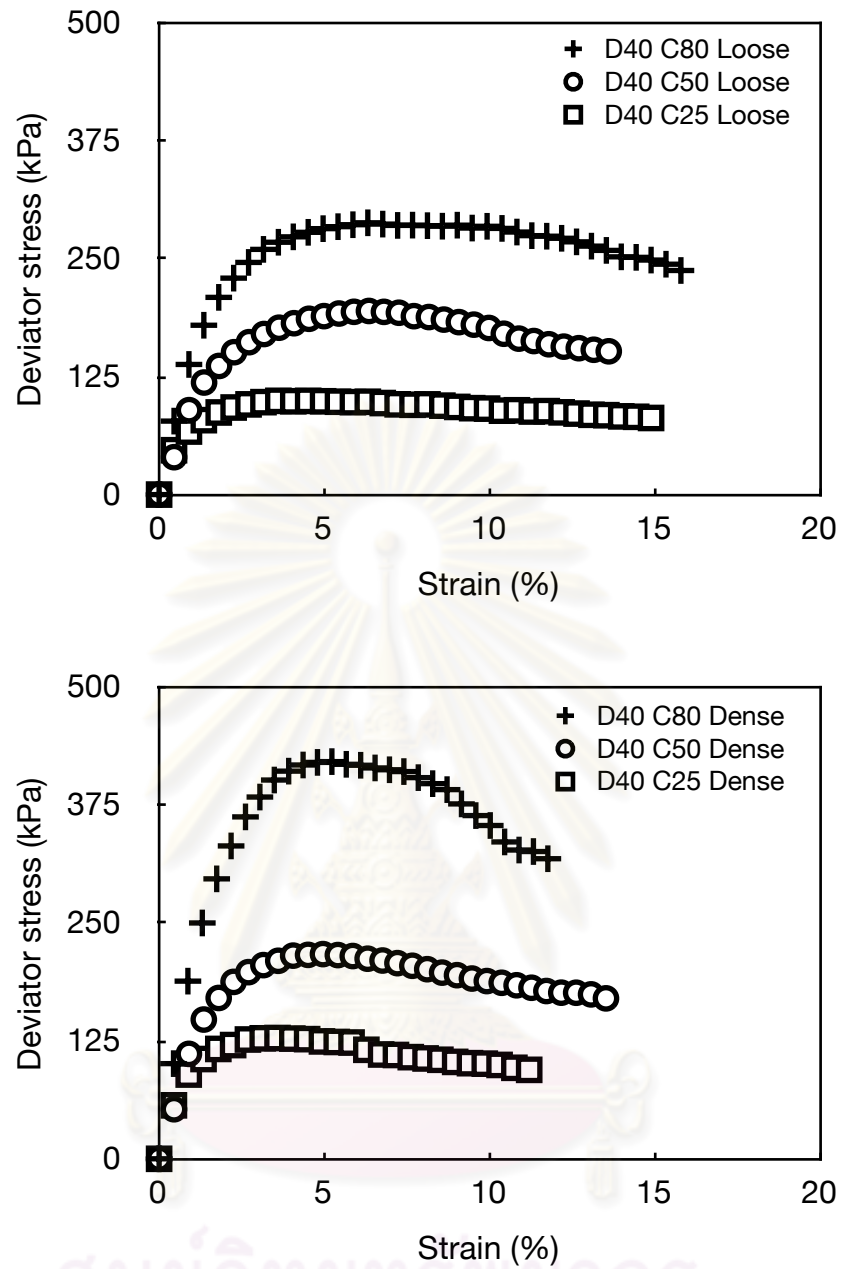
Figure 4.2 The stress - strain relation of D40 specimen in loose and dense conditions with confining pressure 80, 50 and 25 kPa
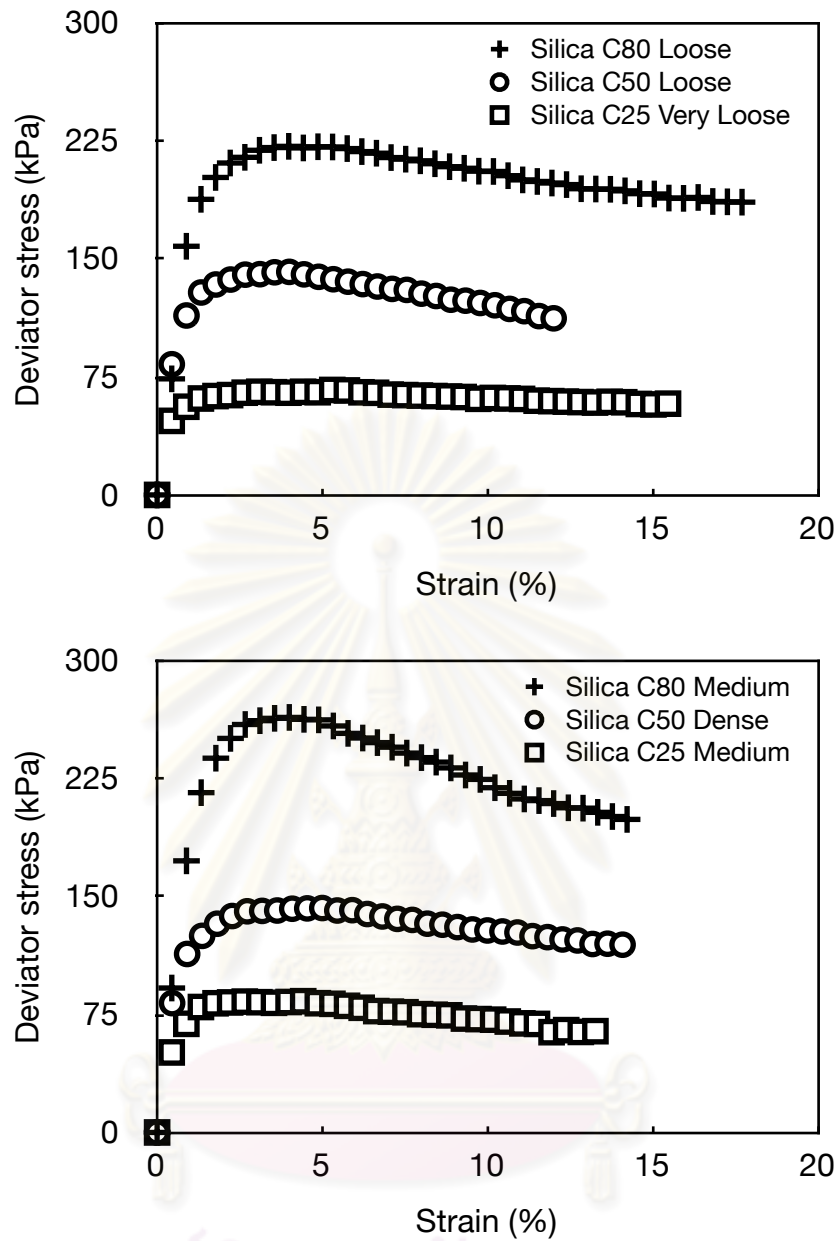
Figure 4.3 The stress - strain relation of Silica specimen in very loose, loose and dense conditions with confining pressure 80, 50 and 25 kPa

Table 4.1 Summary of the test results of stress - strain relationship

Initial condition	σ'_c (kPa)	Type of sand	Stress - strain characteristics			
			ε_1 (%) at peak	Max. q' (kPa)	ε_1 (%) at ultimate	Ultimate q' (kPa)
Loose	25	D16	4.42	98	15.47	87
		D40	3.61	99	14.87	81
		Silica[c]	5.30	67	15.45	58
	50	D16	5.87, 9.96[b]	184, 185[a]	18.11	174
		D40	5.89	194	13.60	152
		Silica	4.00	142	11.99	112
	80	D16	6.34	306	15.85	268
		D40	6.31	288	15.78	237
		Silica	3.54	221	17.68	186
Dense	25	D16	4.74	126	10.76	95
		D40	3.13	128	11.19	94
		Silica[d]	2.21	83	13.25	64
	50	D16	4.79	245	12.62	178
		D40	4.88	217	13.31	170
		Silica	4.99	143	14.07	119
	80	D16	4.40	341	12.77	275
		D40	5.22	421	11.75	318
		Silica[d]	4.00	264	14.21	199

σ'_c = confining pressure, ε_1 = axial strain and q' = deviator stress;
[a] represents an actual peak and [b] its corresponding strain;
[c] represents a very loose condition and [d] represents a medium condition

4.2 Shear Wave Velocity During Isotropic Loading and Shearing

4.2.1 Shear wave velocity under isotropic loading

Many researchers proposed the equations to correlate between V_s and state of stress in the direction of particle motion and wave proportion. Because sands are particulate materials, their V_s is governed by the mean state of stress (σ'_{mean}) in the polarization plane, where effective stress σ'_3 and σ'_1 act in the direction of particle motion and in the direction of shear wave propagation, respectively (Hardin and Richart, 1963). As a result, the V_s - stress relationship for granular material under isotropic loading (σ'_0) can be expressed as equation 4.1 by Santamarina *et al.* (2001):

$$V_s = \alpha \left(\frac{\sigma'_0}{1 \text{ kPa}} \right)^{\beta} \tag{4.1}$$

where α and β are experimentally determined from the in-situ or laboratory tested results. The α and β parameters represent the mechanical responses, i.e. contact effects, void ratio, coordination number, fabric change as well as the loading history. For a given soils, the α factor and β exponent can be uniquely estimated depending on the their porosity. The formulation of equation like in equation 4.1 for this studies can be shown by trend line of power function as in Figure 4.4 - 4.6 for D16, D40 and Silica sand samples in various initial state conditions. The values of α factor and β exponent of these testing results are plotted in the relationship, reproduced from Santamarina *et al.* (2001), between the typical value for α and β coefficients of clays, sands, steel balls and lead shot in order to observe the accuracy of the testing results obtained in the experiments (Figure 4.7). It can be discerned that the data from this studies moderately underestimates both α and β parameters compared to the linear correlation, equation 4.2, of those compiling data of various granular materials. However, the opposite trend between each other can be perceived in that such plots.

$$\beta = 0.36 - \frac{\alpha}{700} \tag{4.2}$$
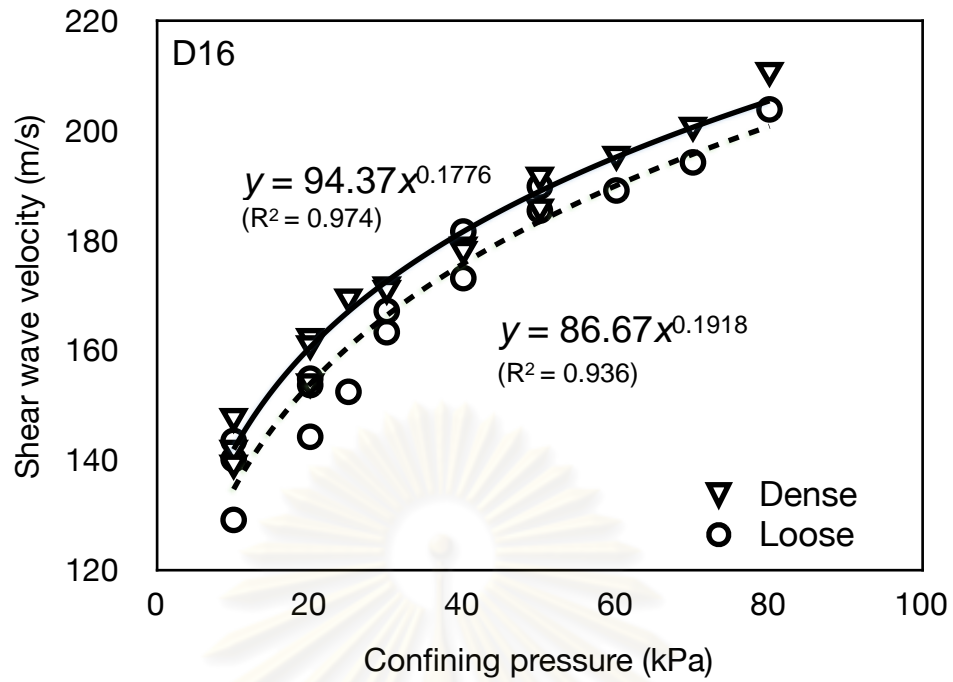
Figure 4.4 Shear wave velocity and stress relation of D16 sand in loose and dense conditions and its empirical relation
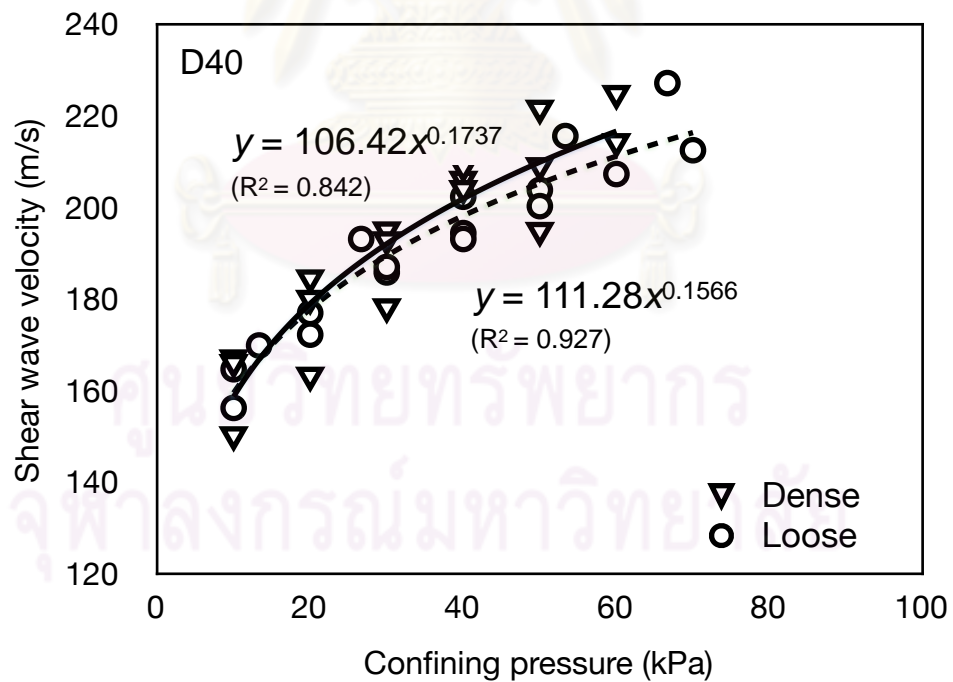
Figure 4.5 Shear wave velocity and stress relation of D40 sand in loose and dense conditions and its empirical relation
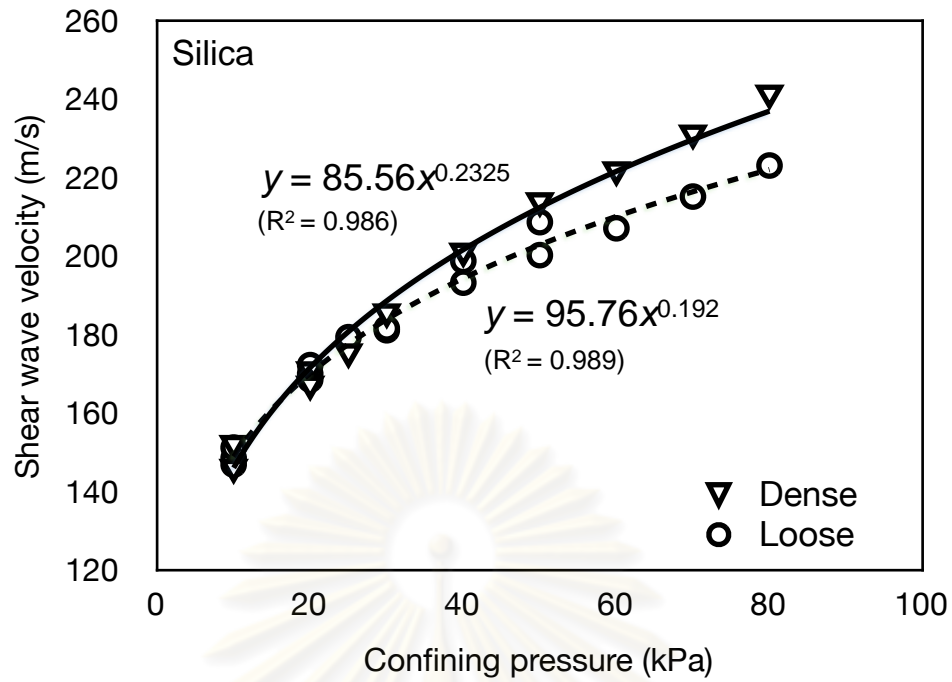
Figure 4.6 Shear wave velocity and stress relation of Silica sand in loose and dense conditions and its empirical relation
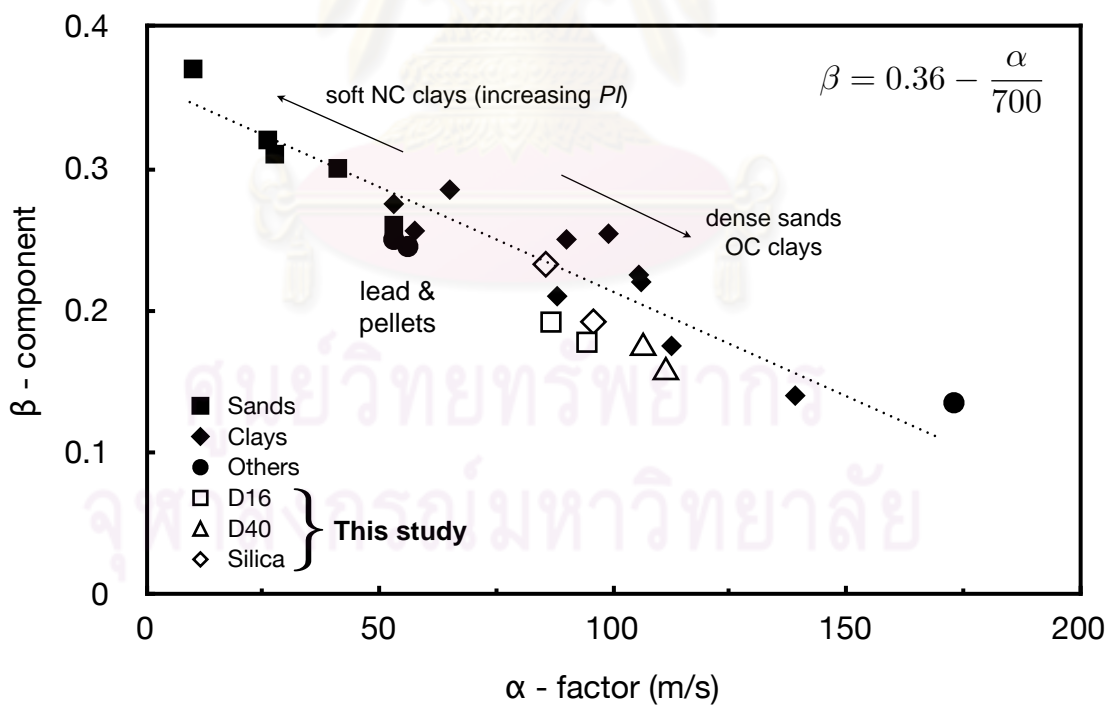
Figure 4.7 Typical values for α and β coefficients

(reproduced from Santamarina *et al*., 2001)

However the value of α involves the influences of various properties, i.e. sample density as well as fabric characteristics. It is convenient to separate α factor into two new parameters; 1) *A* which includes the effect of grain properties and 2) *F(e)* which includes the influence of packing properties, i.e. void ratio (e) and coordination number (C_n). Consequently, V_s that is measured within the same soil in various packing properties, e.g. loose and dense state, can be compared. Inversely, if we know V_s and their grain characteristic parameter, *A*, the porosity, *n*, or *e* can be empirically estimated. Equation 4.1 can be re-written as follows (Santamarina *et al.*, 2001):

$$V_s = AF(e) \left(\frac{\sigma_0'}{1 \text{ kPa}} \right)^{\beta} \tag{4.3}$$

The function *F(e)* has been proposed for both sands and clays from the derivation of empirical formulas tested by various methods, e.g. resonant column, cyclic triaxial as well as ultrasonic pulse. The detailed formulation of this function can be found in Ishihara (1996). However, the classical proposed function (equation 4.4 and 4.5) by Hardin and Richard (1963) will be employed in this analysis.

$$F(e) = \frac{(2.17 - e)^2}{1 + e} \qquad \text{round particles} \tag{4.4}$$

$$F(e) = \frac{(2.97 - e)^2}{1 + e} \qquad \text{angular particles} \tag{4.5}$$

Figure 4.8 shows the variation between V_s and e of the D16, D40 and Silica sand in loose and dense conditions. This shear wave propagates within an elastic range of soil stress in an isotropic confining environment. It can be seen from this figure that the relatively linear correlation between V_s - e can be drawn though a scatter of data can be observed especially in the angular shape of soil grain, e.g. D16 and D40. Moreover, it can obviously conclude that the higher the void ratio the slower the shear wave velocity.
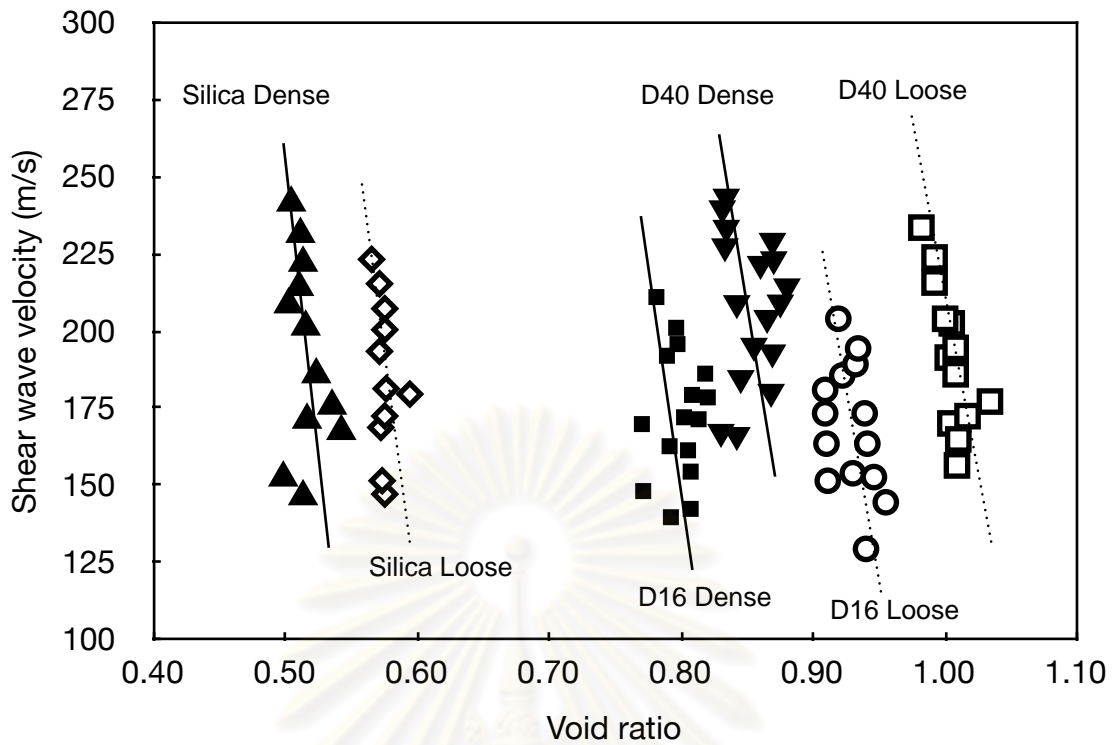
Figure 4.8 The variation between shear wave velocity and void ratio of D16, D40 and Silica sand in loose and dense conditions under isotropic loading

4.2.2 Shear wave velocity during shear

After required initial state of the test was attained, the sand specimen would be sheared by increasing the vertical load at a small rate of compression while the horizontal load would be kept to be constant by vacuum suction throughout the test. There are two empirical relations proposed in the literature to correlate between the V_s along the principle planes, x and y, with the stress in the direction of σ'_3 and σ'_1 which is the direction of particle motion and direction of wave propagation, respectively. Santamarina *et al.* (2001) complies those empirical formulas with the state of stress in anisotropically loaded media as follows;

$$V_s = \Omega \left(\frac{\sigma'_3}{1 \text{ kPa}} \right)^{\theta} \left(\frac{\sigma'_1}{1 \text{ kPa}} \right)^{\delta} \tag{4.6}$$

or

$$V_s = \Theta \left(\frac{\sigma_1' + \sigma_3'}{2 \text{ kPa}} \right)^{\zeta} \left(\frac{\sigma_1' - \sigma_3'}{2 \text{ kPa}} \right)^{\psi} \tag{4.7}$$

Similar to the empirical relationship of isotropically loading condition (equation 4.1), the coefficients Ω and Θ represent the void ratio of the arrangement at constant fabric as well as the packing property while the exponent constants θ, δ, ζ and ψ reflect the contact effect and the influence of fabric change. Those material parameters can be obtained in the experiments. Equations 4.6 and 4.7 will shorten to equation 4.1 in the isotropic state of loading.

Santamarina *et al.*, 2001 states that the effect of void ratio in coarse-grained materials, i.e. Ω and Θ, can also be separated to the function $F(e)$ as in equation 4.3. Nevertheless, this void ratio dependency is less relevant when the cohesionless materials were subjected to anisotropic loading due to fabric evolution and change in void ratio during shear. Santamarina and Cascante (1996) performed a resonant-column tests to observe the effect of isotropic and deviatoric stresses on wave propagation in paticulate materials at low strains as well as to interpret results at the micro level. The results of their experiment showed that the value of exponents θ and δ is in agreement with the exponent β obtained under isotropic loading, namely $\theta + \delta = \beta$. The stress acting in the direction of particle motion has a greater influence on V_s propagation (higher value of exponent parameter) than the stress in the direction of wave propagation. The exponent constants ζ and ψ of equation 4.7 were also regressed. The exponent ζ of the mean effective stress in the polarization plane is very similar to the isotropic exponent β. However, the exponent ψ for the deviatoric stress is close to zero ($\psi \approx 0$), i.e. -0.01 in axial compression, even when isotropic data was not considered in the regression analysis. Therefore it is sufficient to some extent, i.e. stress ratio less than 2 to 3, to calculate the V_s by considering only the mean state of stress in the polarization plane and the exponent for this mean stress equals to the exponent for isotropic loading, $\zeta = \beta$. The new equation as in equation 4.8 can be governed;

$$V_s = \Psi \left(\frac{\sigma'_{mean}}{1 \text{ kPa}} \right)^{\varphi} \tag{4.8}$$

where Ψ is the coefficient representing the effect of void ratio and φ is the exponent parameter reflecting the contact behavior under anisotropic loading environment of granular material. The figures illustrating the impact of σ'_{mean} to the V_s can be shown in Figure 4.9 - 4.11. It can be observed from those figures that the initial state of the sample, i.e. confining pressure and density condition has a few influences to the propagation velocity of shear wave. The grain size particle also impacts the shear wave propagation speed, the smaller the grain size the higher the V_s. This might be explained by the higher number of contact point of small grain size than large grain size. Moreover, at a certain value of σ'_{mean}, e.g. after starts shearing, the V_s drops continuously and the relationship as in equation 4.8 is not further valid due to the effect of strain localization.

The results from the triaxial compression test during shear in which the state of anisotropically loading takes place show that the influence of deviatoric stress, $(\sigma'_1 - \sigma'_3)$ is relatively low comparing to the influence of σ'_{mean} for all grain size of particles as well as packing conditions (Figure 4.12 - 4.14). This outcomes confirm the previous work by Santamarina and Cascante (1996) and the relationship of equation 4.8 that includes only the effect of σ'_{mean}. However, similar to the previous relationship between σ'_{mean} and V_s, at a certain level of shearing, i.e. principal stress ratio (q'/p') more than 1.2, the V_s deviates from its normal behavior, i.e. slowly increasing as the σ'_{mean} gets higher, as in equation 4.8. Namely, V_s stops increasing but tends to lessen and varies in some ranges before failure (Figure 4.15 - 4.17). This might be of course due to non-homogenous deformation as well as the initiation of the shear bands inside the specimen. The detailed discussion for this phenomena will be made later in the following section.

Figure 4.18 shows the example of shear wave propagation during isotropic consolidation and shear.
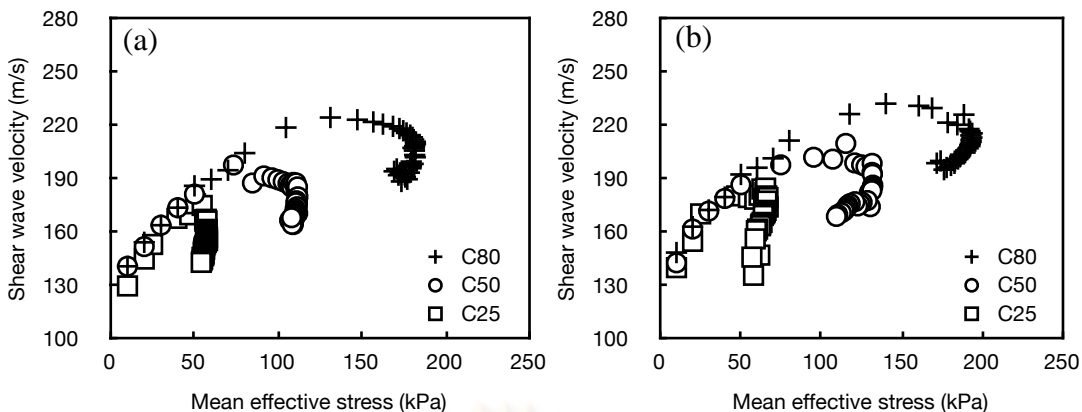
Figure 4.9 The influence of mean effective stress to shear wave velocity on D16 sample for
a) loose and b) dense state in various confining conditions
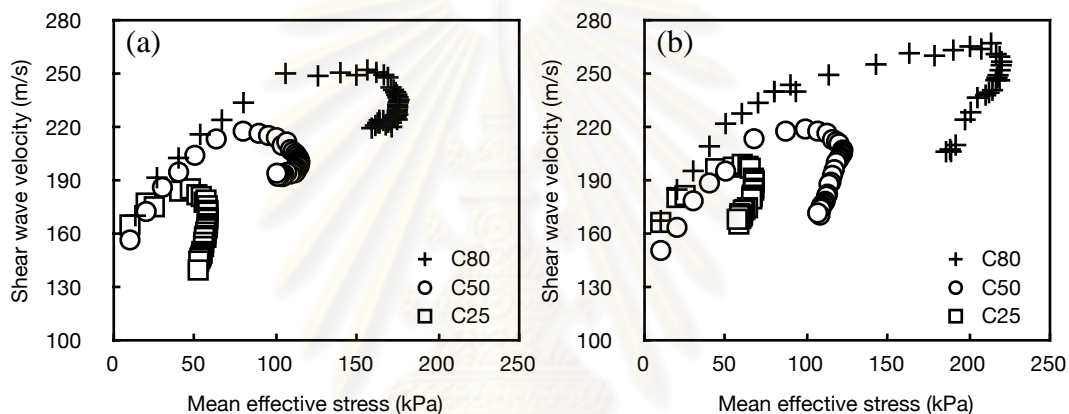
Figure 4.10 The influence of mean effective stress to the shear wave velocity on D40 sample
for a) loose and b) dense state in various confining conditions
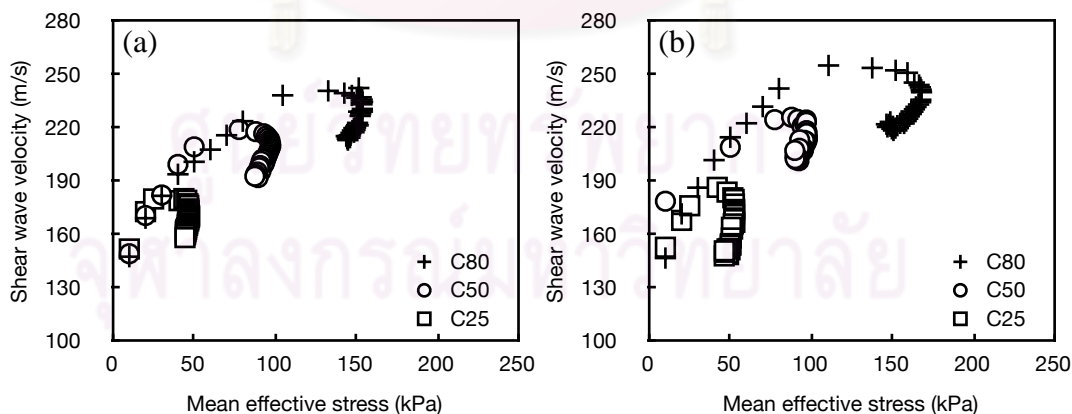
Figure 4.11 The influence of mean effective stress to the shear wave velocity on Silica sand
for a) loose and b) dense state in various confining conditions
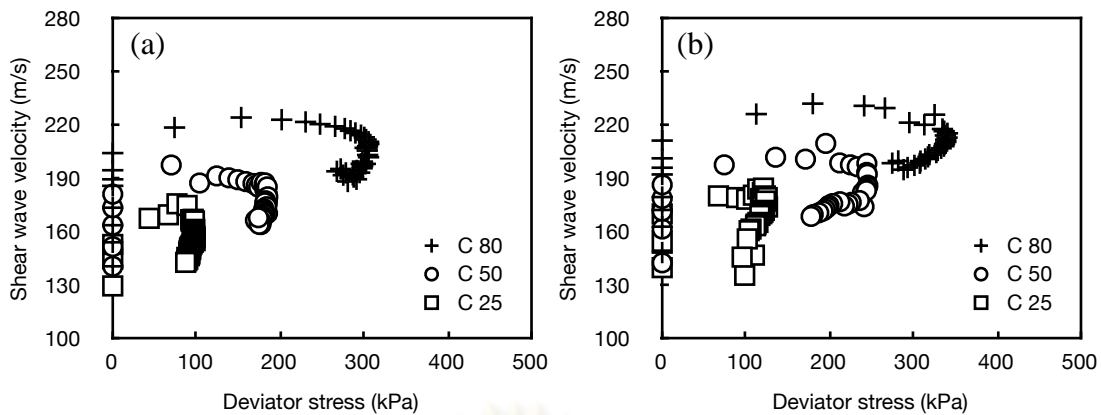
Figure 4.12 The influence of deviator stress to shear wave velocity on D16 sample for

a) loose and b) dense state in various confining conditions
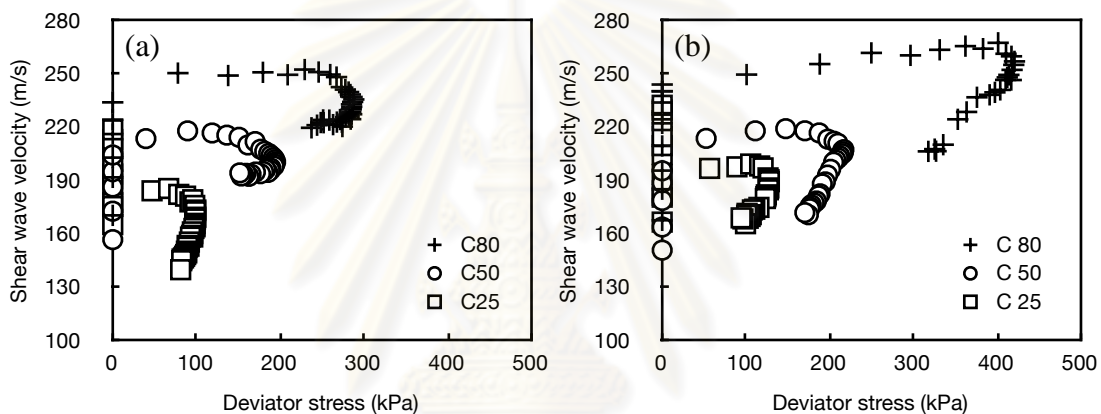
Figure 4.13 The influence of deviator stress to shear wave velocity on D40 sample for

a) loose and b) dense state in various confining conditions
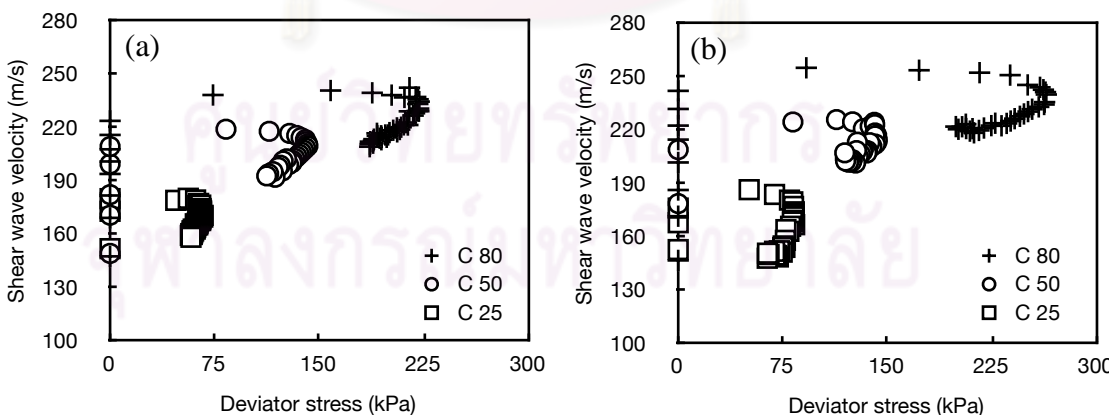
Figure 4.14 The influence of deviator stress to shear wave velocity on Silica sand for

a) loose and b) dense state in various confining conditions
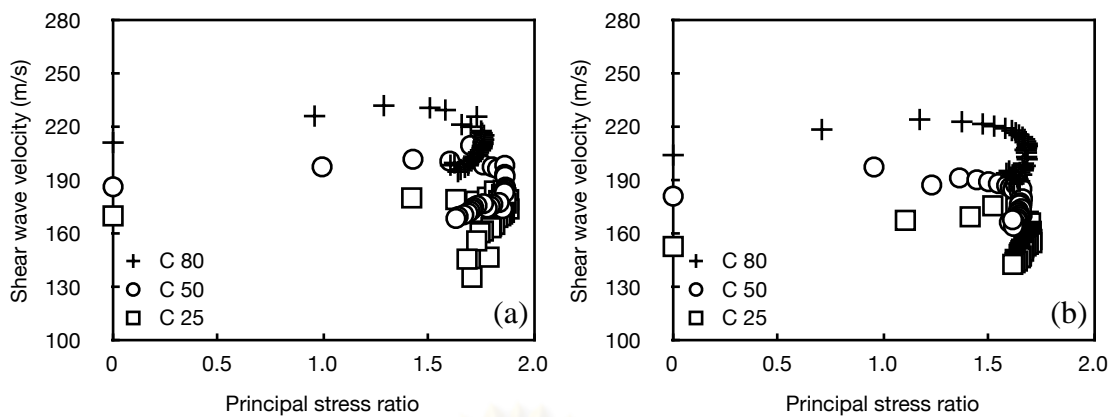
Figure 4.15 The variation between shear wave velocity and the principal stress ratio on D16 sample for a) loose and b) dense state in various confining conditions
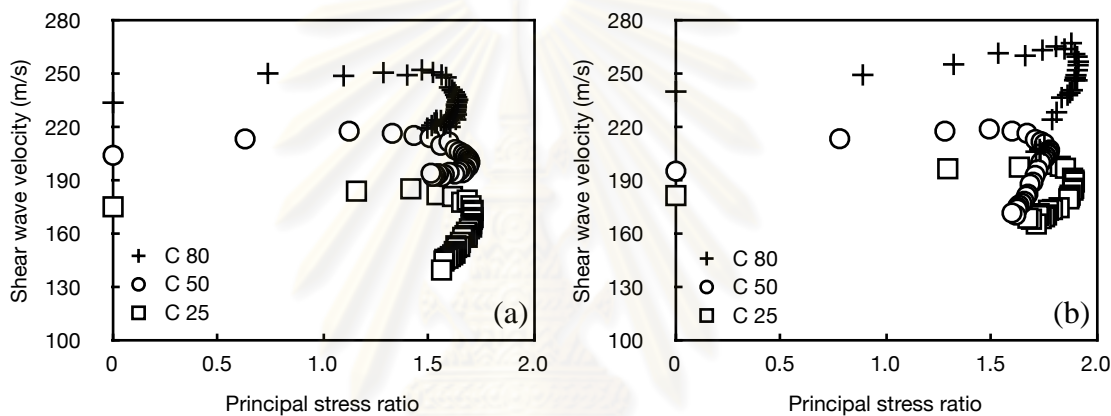
Figure 4.16 The variation between the shear wave velocity and the principal stress ratio on D40 sample for a) loose and b) dense state in various confining conditions
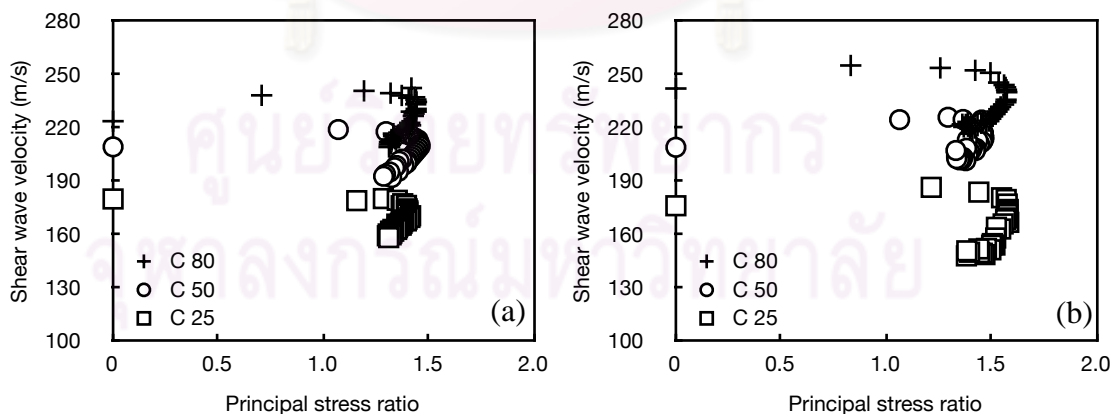
Figure 4.17 The variation between the shear wave velocity and the principal stress ratio on Silica sand for a) loose and b) dense state in various confining conditions
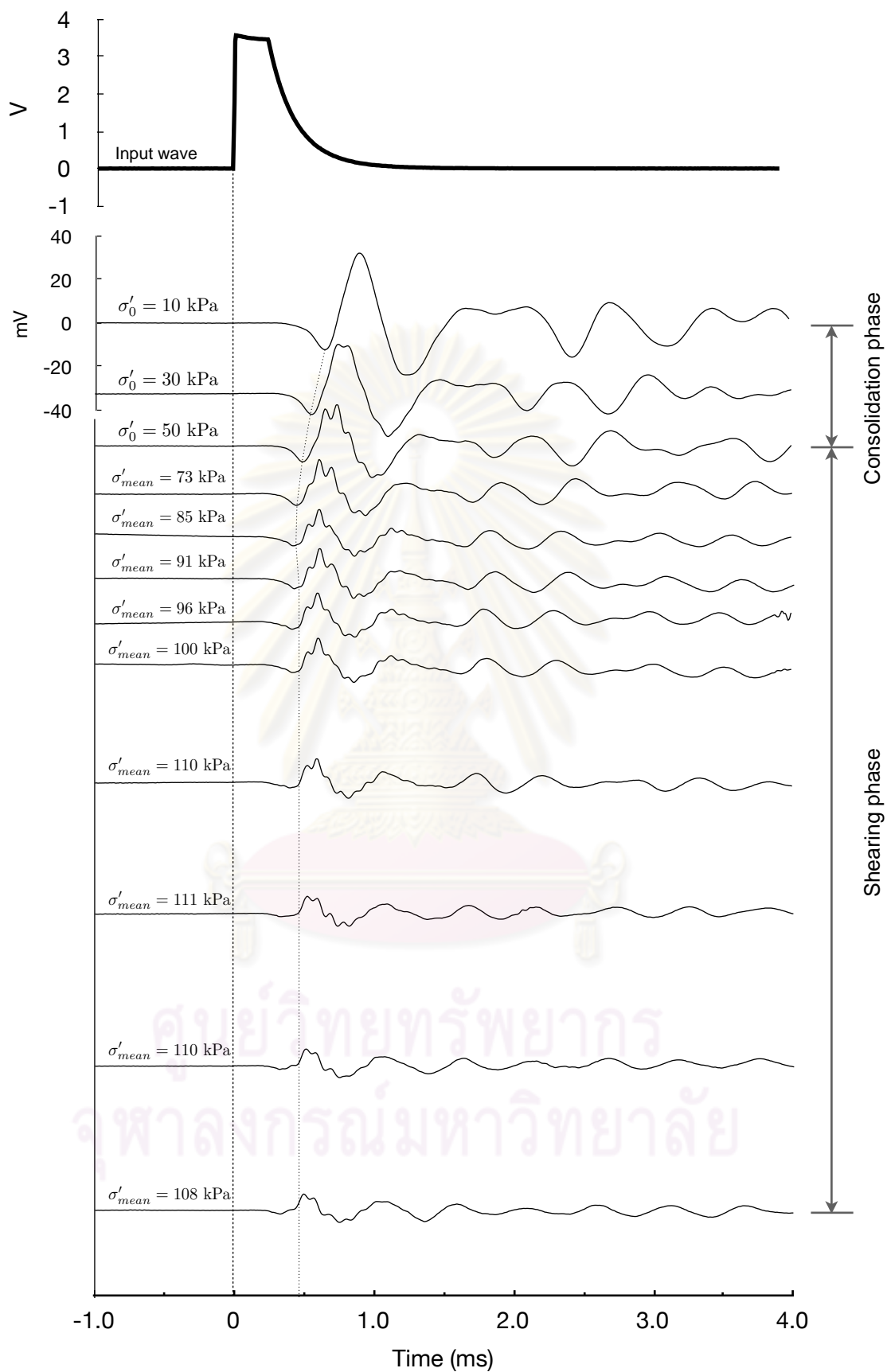
Figure 4.18 Shear wave propagation during isotropic consolidation and shear

4.3 The Initiation and Persistent of Strain Localization

4.3.1 Observation from shear wave velocity profile and stress ratio

There are a number of conclusions stating the onset and formation of shear band. Desrues and Viggiani (2004) inferred from their plane strain compression tests on sand that the onset of a persistent shear band will always occur near, i.e. at or slightly before, the peak of stress ratio and never occurs after that peak. Figure 4.19 shows an example of the stress strain responses in terms of effective stress ratio (t/s') vs global axial strain of biaxial test in sand and the stereophotogrammetry-based increment fields of shear strain intensity to explain that conclusions. From this figure, it can be seen that the progression of strain localization in test shf06 indicates the two parallel zones of strain localization form in the middle portion of the tested specimen in the increment 3-4, promptly prior to the peak of the stress ratio. It can also be perceived that though no shear bands were observed before increment 3-4, shear strain fields however suggest a somewhat non-homogeneous deformation presenting during an increment 2-3.

Figure 4.19 The effective stress ratio vs global axial strain of biaxial test in sand and the stereophotogrammetry-based increment fields of shear strain intensity
(Desrues and Viggiani, 2004)

Finno *et al.* (1997) performed a series of plane strain compression on loose masonry sand. They concluded from the tested results that regardless of the drainage conditions, consolidated void ratio as well as mean effective stress, the friction mobilized when strain localization begins is very close to its maximum value. An

example of their results can be shown graphically in Figure 4.20. In this figure, we can see the lateral deformation response determined by the two pairs of horizontal linear variable displacement transducers (LVDTs). The local lateral strain at two elevations of the specimen is shown in images (a) and (b) while the absolute width difference between the upper and lower parts of the specimen and the sled or block movement are plotted in (c). Initially, the local lateral strain responses are parallel indicating a relatively uniform deformation. These responses ideally equal to the global axial strain (dashed line). However, based on the local lateral strain response, non-uniform deformation initiated at about 2.7% of global axial strain, as the two lateral strain responses begin to obviously diverge. This onset of non-homogeneous deformation is marked as point O. At approximately 3.6% global axial strain (marked as point B), the lateral strain rate of lower portion becomes almost zero (flatted growth) while the upper portion lateral strain rate increases to a constant value. They reported that at this point a shear band has bisected the specimen because deformations have concentrated in a zone of upper LVDT pair whereas no significant deformations are occurring in the zone bounded by the lower LVDT pair. They also found that the sled moves less than 0.3 mm until point O, then begins to move at a rate which becomes constant after 3.9% (point S). These results of lateral responses suggest a pattern of uniform deformation up to point O, followed by the progressive development of a shear band until point B which is the point that the band has completely developed.
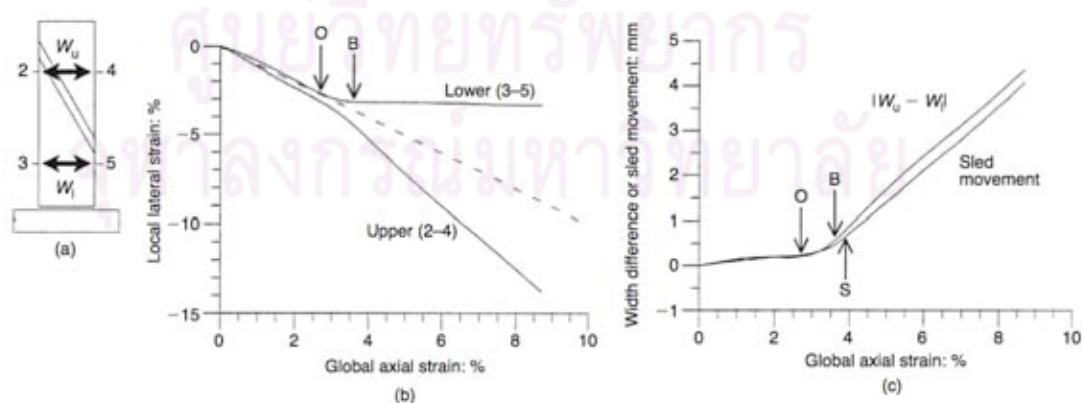
Figure 4.20 (a) The lateral deformation measurement (b) the lateral strain vs the global axial strain at two elevations (c) the absolute width difference between the upper and lower parts of the specimen and the sled or block movement (Finno *et al.*, 1997)
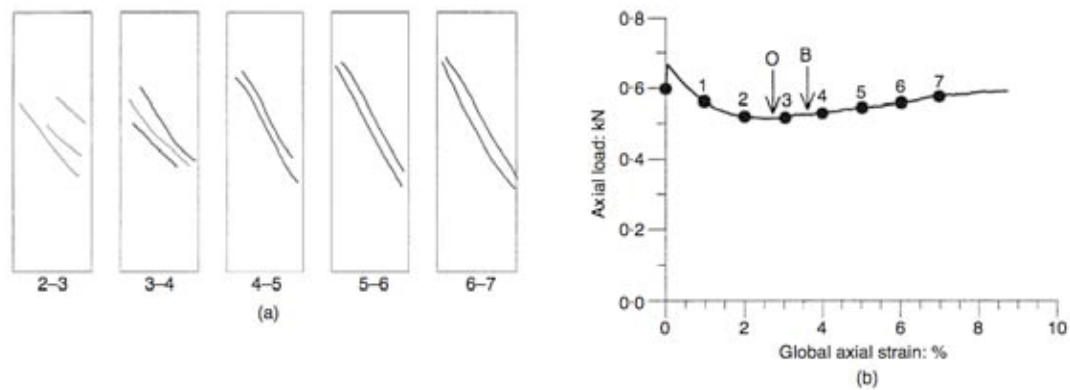
Figure 4.21 Evolution of shear bands (a) images from intervals of global axial strain by stereo-comparison (b) axial load curve (Finno *et al.*, 1997)

They explained from the above figure that while no localization of strain was observed in the test before 2% of global axial strain, a wide zone of slight strain localization appears in the middle portion of the specimen when photographs at 2% and 3% are viewed in stereo. In the subsequent increment 3-4, this zone becomes steeper and narrower, meaning that the shear strains are larger and more localized. A single shear band is clearly observed in increment 4-5 and is maintained throughout the test. To further quantify the progression of shear band formation, points O and B were specified in the axial load curve. While point B is clearly defined by the achievement of constant rates of local lateral strain, the selection of point O is relatively subjective. However, the occurrence of strain localization in increment 2-3 corroborates the selection of point O at approximately 2.7%. The results from the lateral deformation response (Figure 4.20) together with stero-comparison (Figure 4.21) can ably present a consistent account of the strain localization development inside the soil sample. The stress strain response during shear is also presented in Figure 4.22 in terms of effective principal stress ratio (q'/p') against global axial strain. The mobilized friction q'/p' monotonically increases to a peak at 1.13 (point F), then slightly decreases to a constant value of 1.10. This maximum friction mobilized after the onset of non-homogeneous deformation at point O, whereas the band is completely formed (point B) just after point F.
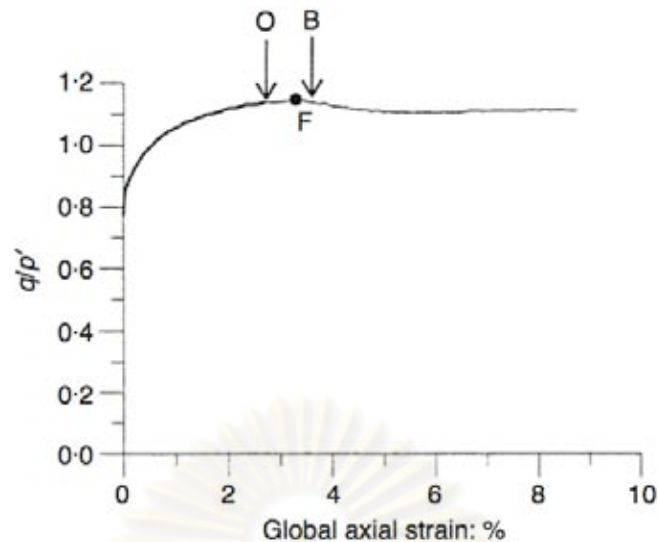
Figure 4.22 Stress strain response in terms of stress ratio during shear (Finno *et al.*, 1997)

From the example of above reports and conclusions in the biaxial tests, for triaxial test results in clays see in Sachan and Penumadu (2007), we can understand that the progression of strain localization takes place in the tested specimens at or shortly prior to the mobilization of peak friction following the fairly uniform vertical (axial) compression coupled with slight lateral expansion. After the achievement of this peak stress, the failure planes in the form of significant multiple shear bands, later developing to a single band, are presented in the post peak response.

Figures 4.23 to 4.40 show the relationship between effective stress ratio (q'/p') versus axial strain which is similar to the previous plot of above researches together with the plot of complete V_s profile against axial strain of triaxial compression test. The typical results of these figures in terms of effective stress ratio as well as the profile of V_s propagation inside the specimen during the entire compression test are depicted in Figure 4.41. It is clearly recognized from the testing results and analyses in the previous sections and in figure 4.41a and 4.41b that V_s in the consolidation state and in the very beginning part of shearing state, i.e. axial strain less than 2%, remarkably increases as σ'_0 or σ'_{mean} increases. The higher the confining pressure, the higher the increasing in V_s. This nonlinear relation is only valid within an elastic range of both isotropic (consolidation state) and anisotropic (shearing state) loading conditions. After soils reach a yield point which is the point of

transformation from the uniform to non-uniform state, V_s tends to grow slowly. The point of material yield is a marked change in the gradient of a stress-strain curve. This is associated with a fundamental change in behavior often from elastic and recoverable straining to inelastic and irrecoverable straining. This yield point in the stress-strain curve corresponds to the first Maximum Shear Wave Velocity (MVS$_f$) during the compression test in this analysis. Moreover, sands with relatively more angular shape, e.g. D16 and D40, due to their inherent characteristic to withstand sliding and rolling of particle movements can a little bit develop the shear wave propagation to a certain value. Namely, the maximum shear wave velocity (MVS) can reach the higher value than the first one (MVS$_f$). In contrast, the results of Silica sand always exhibit the same point between MVS$_f$ and MVS. After the point of MVS the V_s for all tests reduces linearly and remains relatively constant from a particular point of large axial strain. This tendency to some extent confirms the non-uniformity and the initiation of strain localization inside the specimen because V_s is not further a function of void ratio and stress state. It can also be explained that this reduction of V_s is independent on particle shape and size but is dependent on the initial condition of the sample. In other words, dense sample manifests higher downslope than the loose one. This reduction of V_s can be explained by 2 main reasons; 1) the lowering of specimen height during shear and 2) the development of strain localization inside the sample.

Although the maximum stress ratio (MSR) comparatively varies among a specific range of strain but it is rational to note that the lower the initial confining pressure the earlier the mark of MSR. Moreover, at the point of MSR there is no remarkable change in V_s. It is therefore difficult to detect that which point is the initiation point of strain localization inside the soil mass.

Figure 4.23 The stress ratio and shear wave velocity (V_s) against strain for D16 in loose condition with confining pressure 80 kPa

Figure 4.24 The stress ratio and shear wave velocity (V_s) against strain for D16 in loose condition with confining pressure 50 kPa

Figure 4.25 The stress ratio and shear wave velocity (V_s) against strain for D16 in loose condition with confining pressure 25 kPa

Figure 4.26 The stress ratio and shear wave velocity (V_s) against strain for D16 in dense condition with confining pressure 80 kPa

Figure 4.27 The stress ratio and shear wave velocity (V_s) against strain for D16 in dense
condition with confining pressure 50 kPa

Figure 4.28 The stress ratio and shear wave velocity (V_s) against strain for D16 in dense
condition with confining pressure 25 kPa
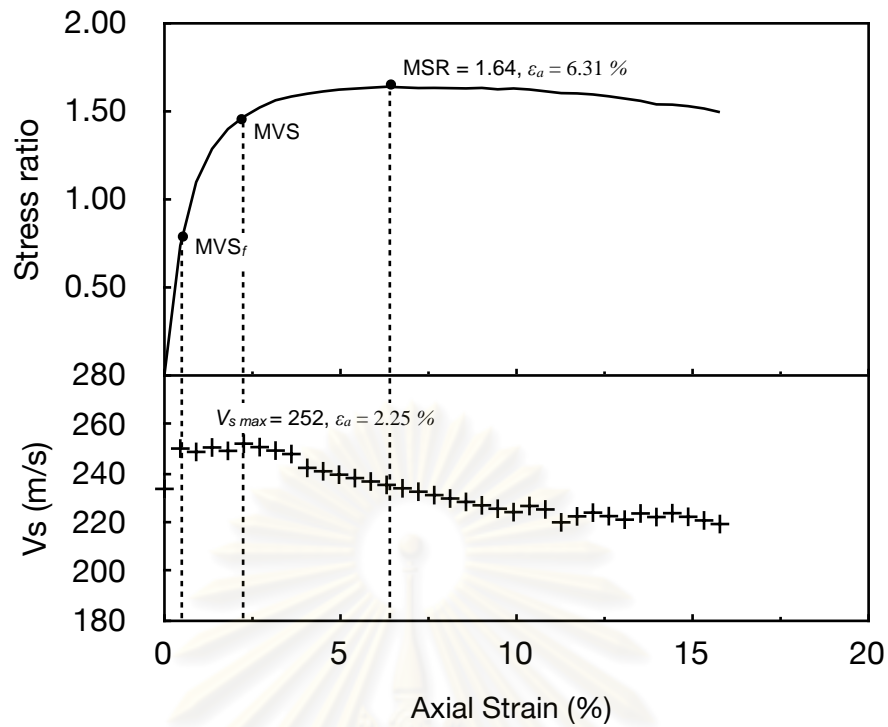
Figure 4.29 The stress ratio and shear wave velocity (V_s) against strain for D40 in loose condition with confining pressure 80 kPa
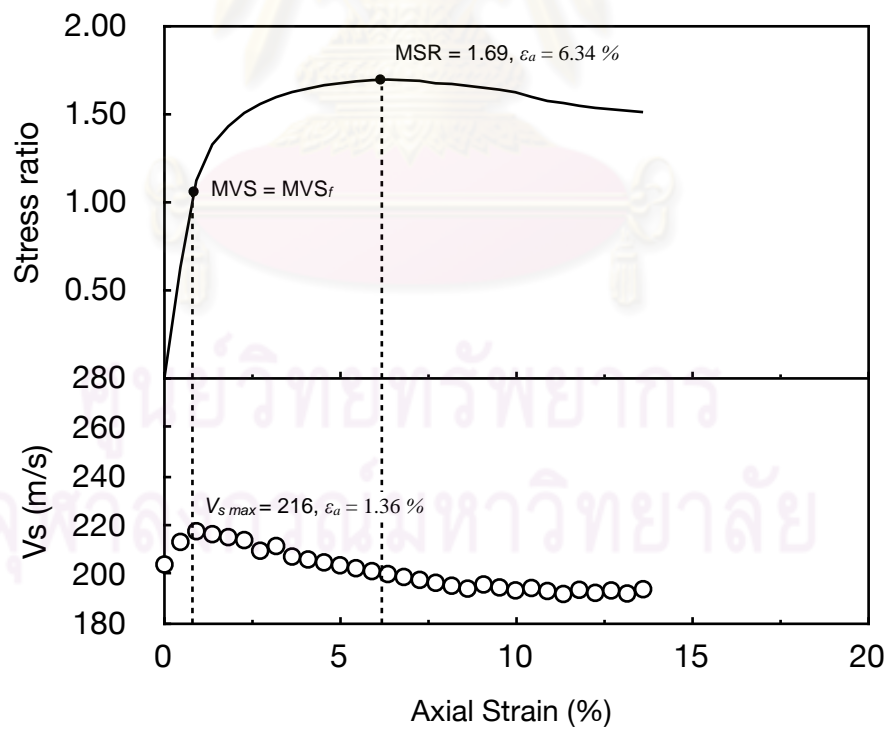
Figure 4.30 The stress ratio and shear wave velocity (V_s) against strain for D40 in loose condition with confining pressure 50 kPa
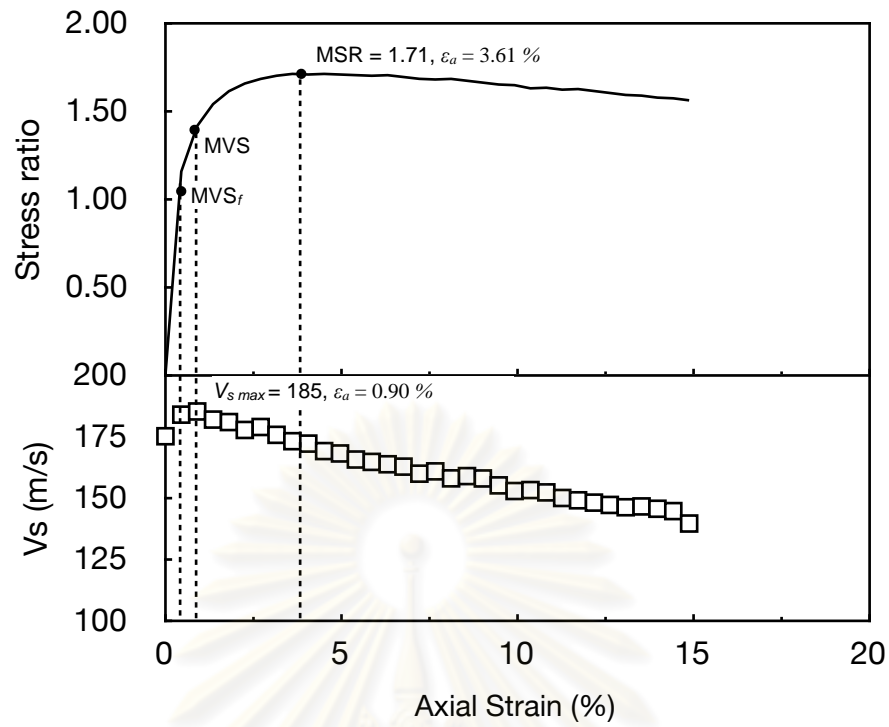
Figure 4.31 The stress ratio and shear wave velocity (V_s) against strain for D40 in loose
condition with confining pressure 25 kPa
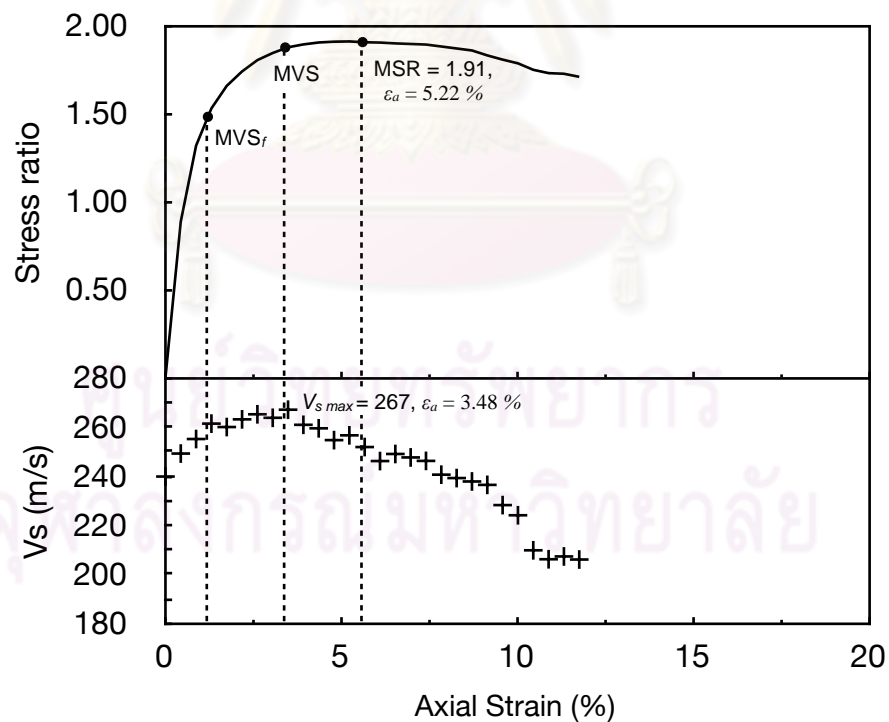
Figure 4.32 The stress ratio and shear wave velocity (V_s) against strain for D40 in dense
condition with confining pressure 80 kPa
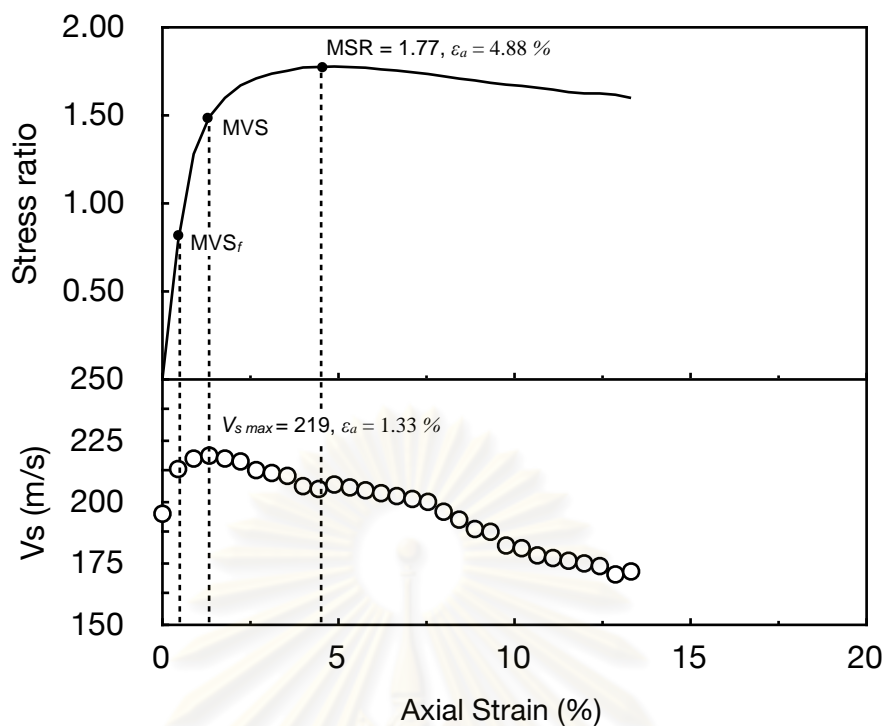
Figure 4.33 The stress ratio and shear wave velocity (V_s) against strain for D40 in dense condition with confining pressure 50 kPa
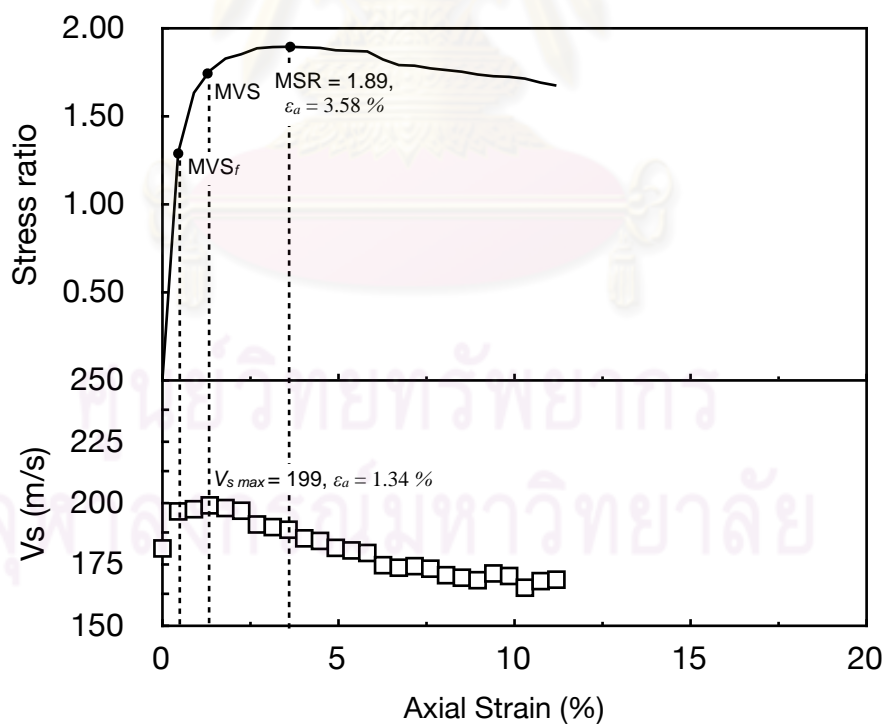
Figure 4.34 The stress ratio and shear wave velocity (V_s) against strain for D40 in dense condition with confining pressure 25 kPa
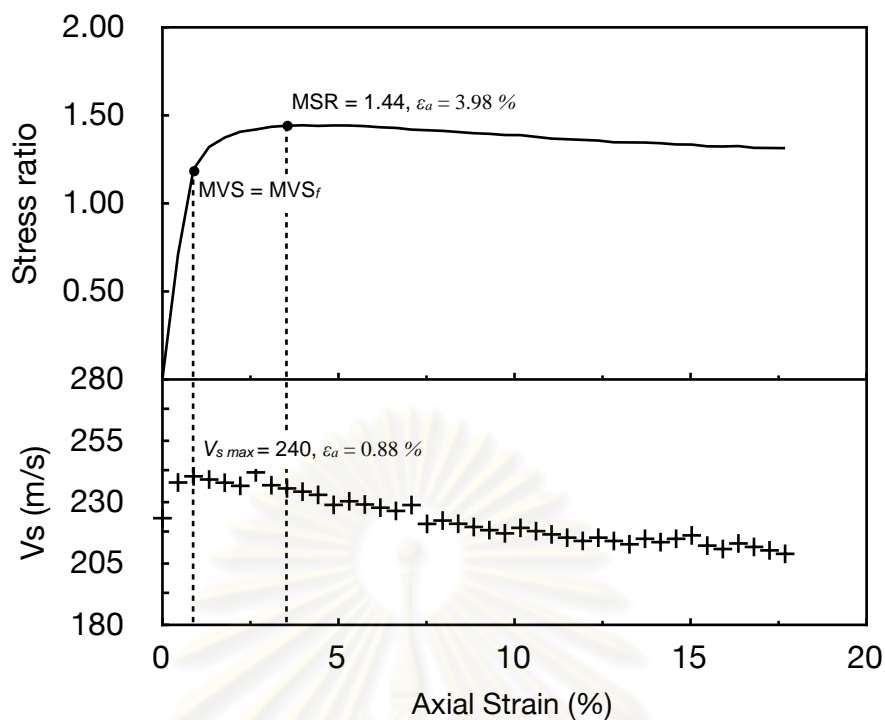
Figure 4.35 The stress ratio and shear wave velocity (V_s) against strain for Silica sand in loose condition with confining pressure 80 kPa
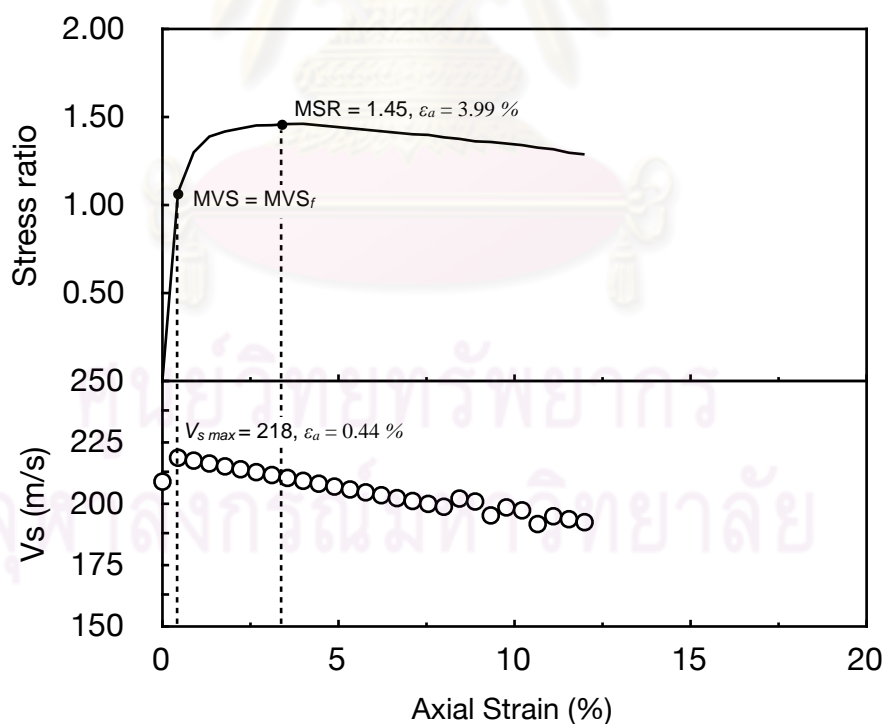
Figure 4.36 The stress ratio and shear wave velocity (V_s) against strain for Silica sand in loose condition with confining pressure 50 kPa
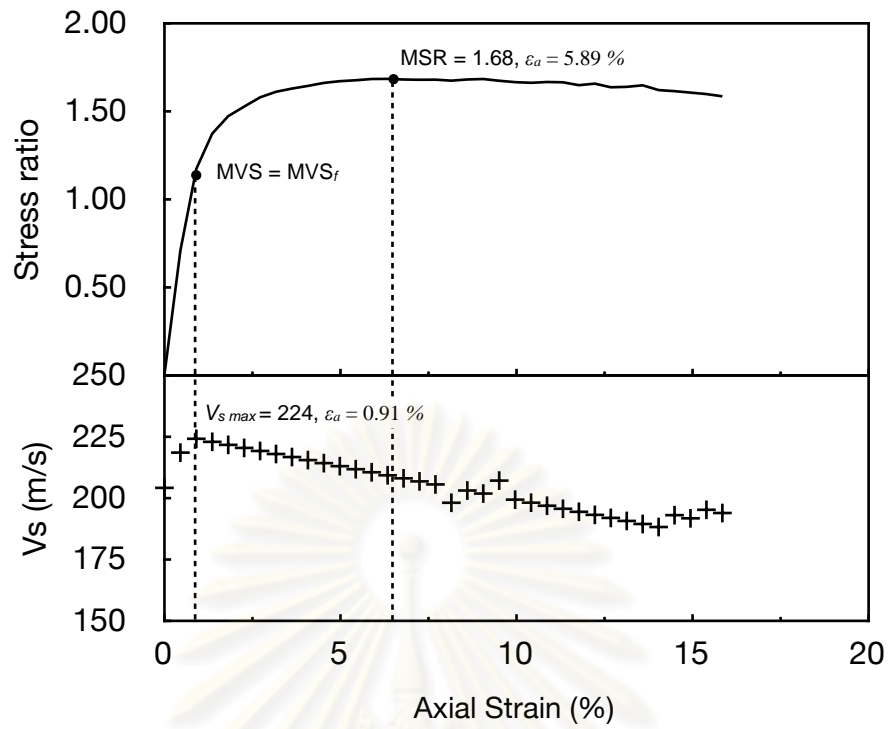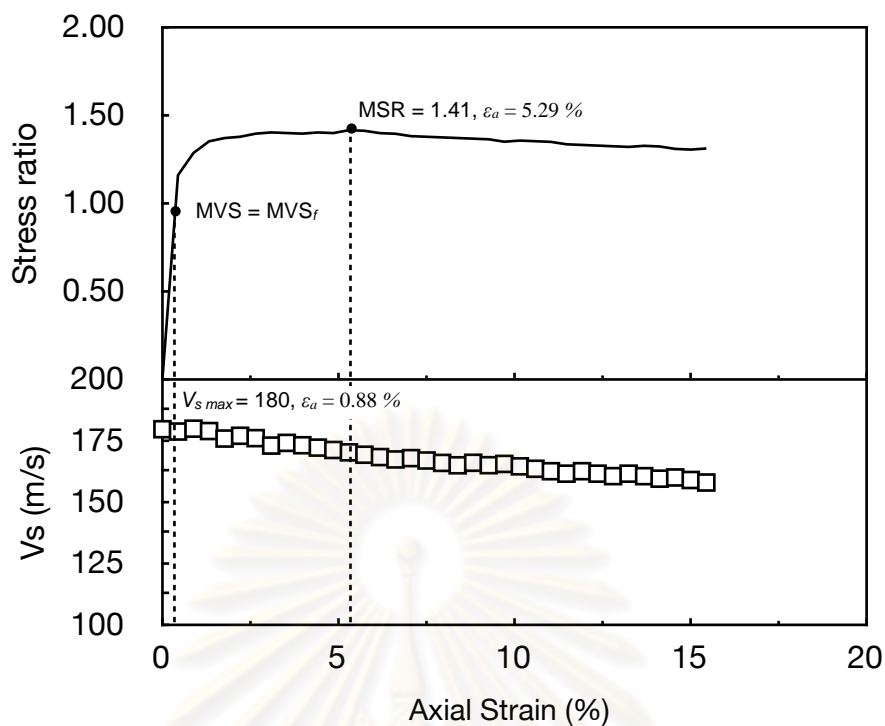
Figure 4.37 The stress ratio and shear wave velocity (V_s) against strain for Silica sand in
loose condition with confining pressure 25 kPa
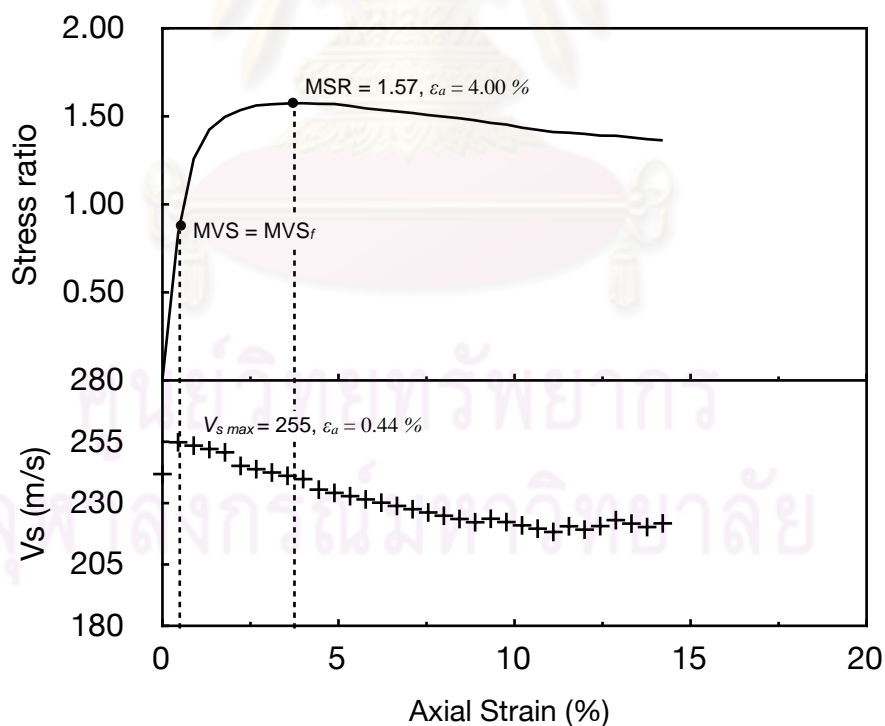
Figure 4.38 The stress ratio and shear wave velocity (V_s) against strain for Silica sand in
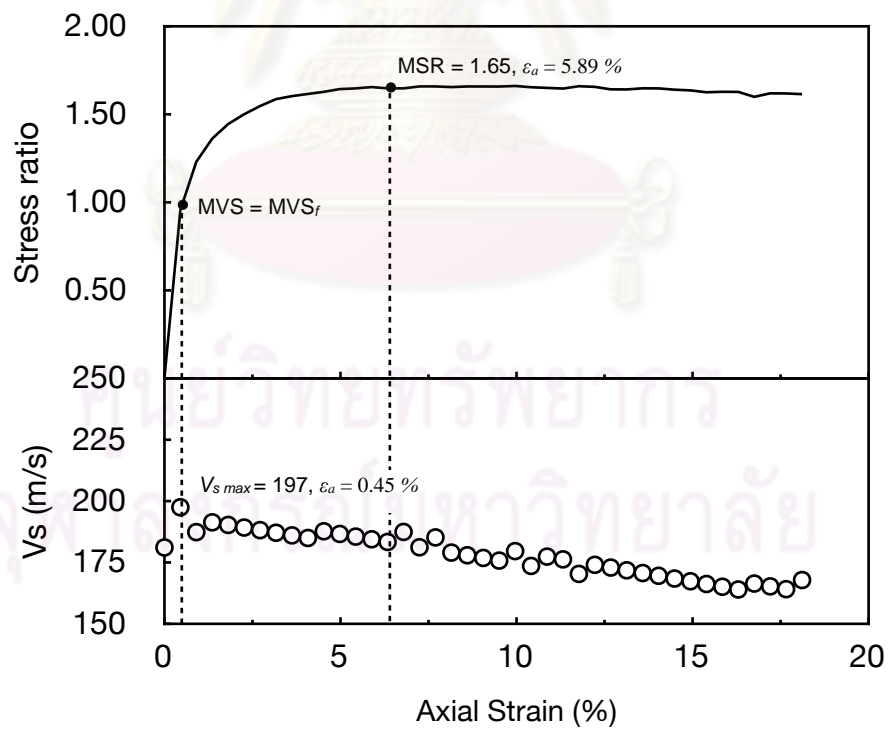dense condition with confining pressure 80 kPa
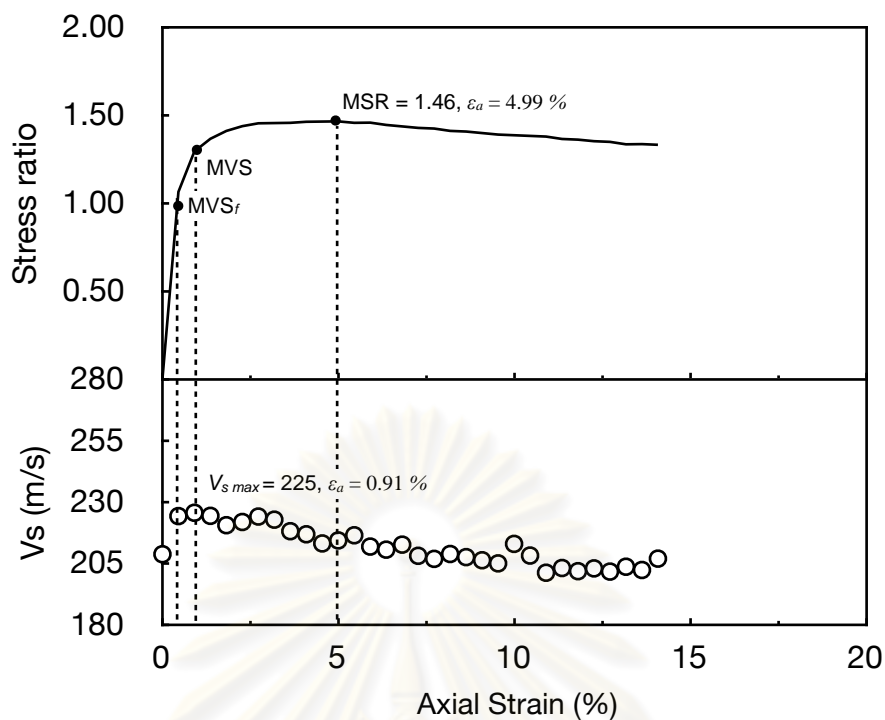
Figure 4.39 The stress ratio and shear wave velocity (V_s) against strain for Silica sand in dense condition with confining pressure 50 kPa
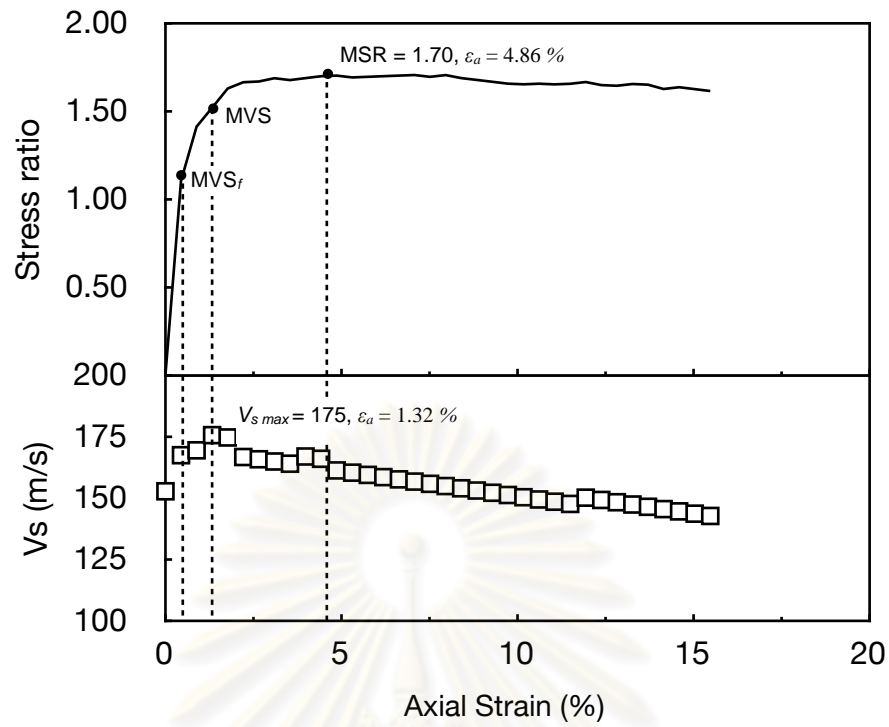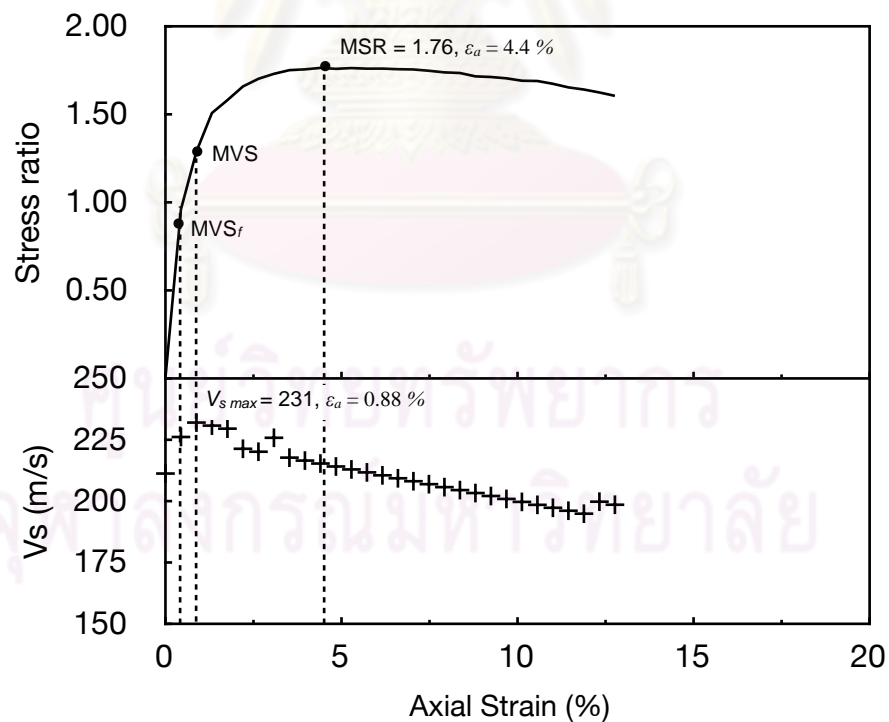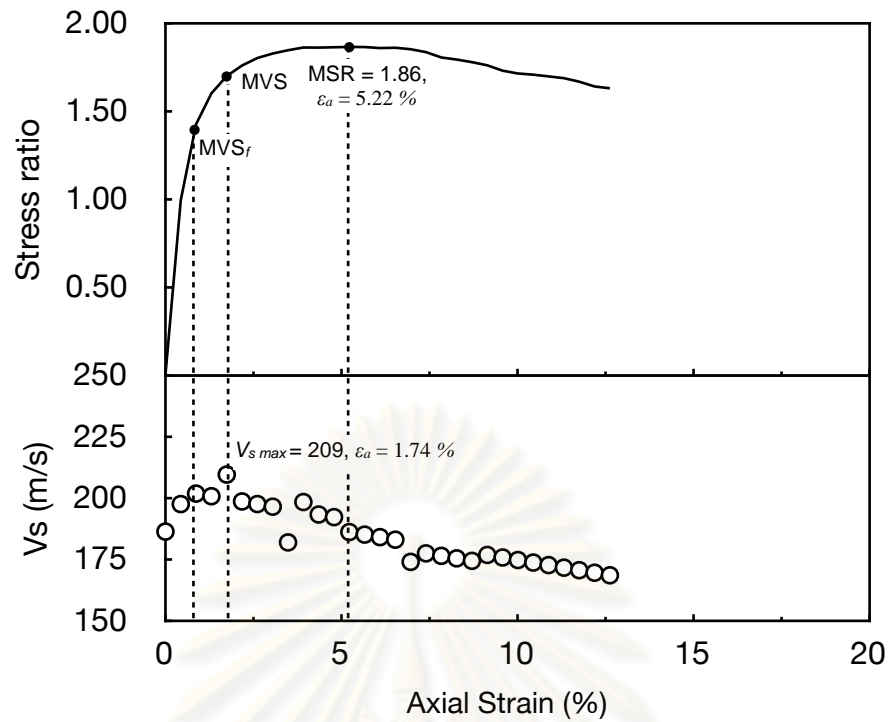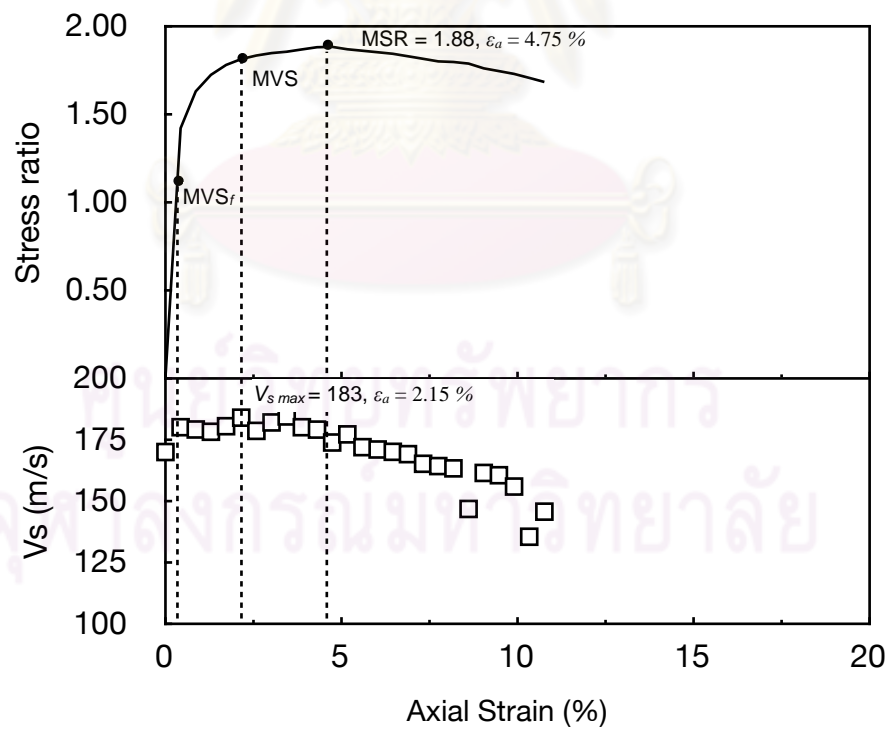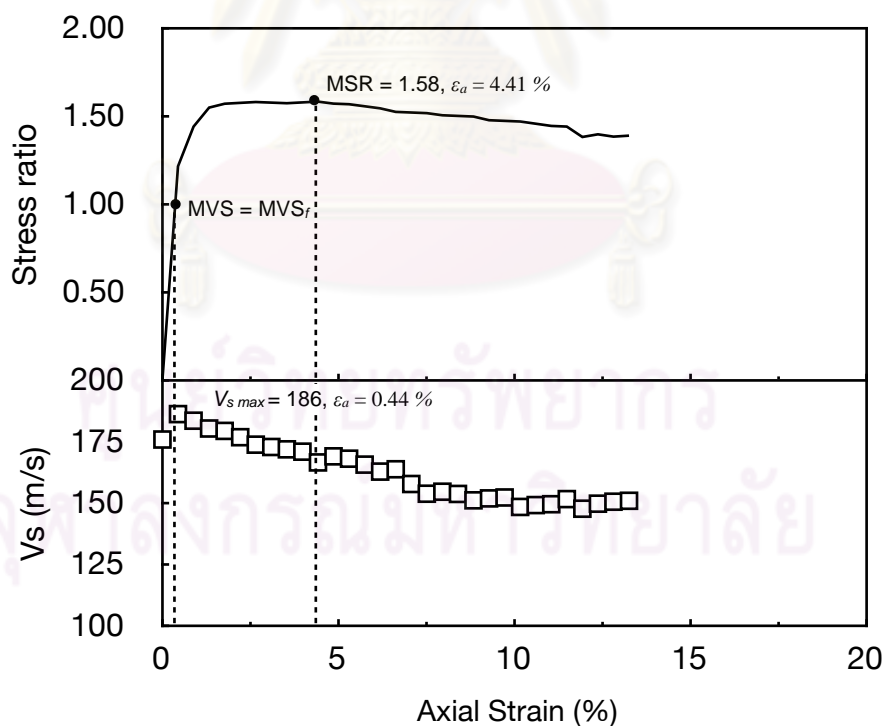

Figure 4.40 The stress ratio and shear wave velocity (V_s) against strain for Silica sand in dense condition with confining pressure 25 kPa
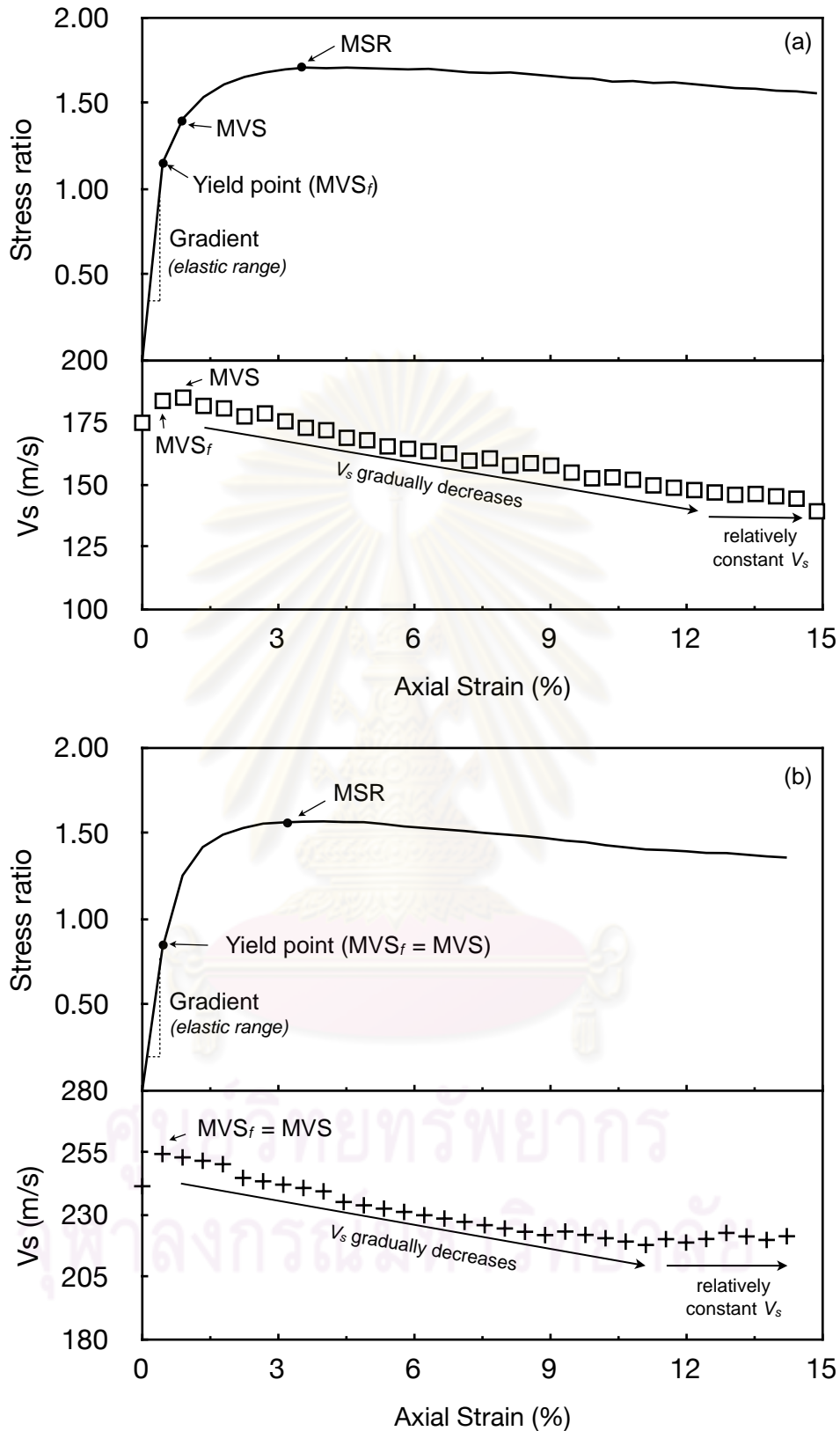
Figure 4.41 The typical results stress-strain and the profile of V_s propagation inside sample during the compression test a) angular-shape and b) round-shape sands

4.3.2 Observation from Digital Image Analysis (DIA) technique

It can be seen from the previous section that although V_s profile can reveal some strain localization characteristics inside the soil sample but the observation of this phenomenon by using DIA would be clearly understand. The measurement of an alteration of grid dimension on the surface membrane of the specimen was performed to observe the local strain distribution inside the deformed sample. This measurements are used to demonstrate how the local elements throughout triaxial specimens of uniform sand evolves during undrained axial compression loading. To compute this local strain profile, the high-resolution of the captured images, i.e. 6 million pixels, would be zoomed in computer software to magnify and precisely determine the deformed size of local elements. The local strain analysis would be based on photo analysis of images taken from a fixed viewpoint at different times during the loading process. The deformation of each local element can be directly calculated by the differentiation between the original length to the deformed length of successive pairs of photographs. The shortest length which can be measured from the magnified high-resolution image is about 0.01 mm.

Two series of local strain analysis by DIA were carried out. The first DIA was performed to observe the zone of strain localization as well as the initiation time of localization in terms of global axial strain. The computation of local axial strain of each element within 3 columns throughout entire height of the specimen will be operated (Fig. 4.42, 4.44, 4,46 4.48, 4.50 and 4.52). The second DIA was done to observe soil non-uniformity and the local strain profile inside the specimen especially in the localization zone. Nine local elements would be randomly selected and calculated the local axial strain. This local strain profiles would then plotted against global axial strain to help in identifying the initiation and evolution of strain localization of sand in triaxial compression tests (Fig. 4.43, 4.45, 4.47 4.49, 4.51 and 4.53). Six sand samples, i.e. D16 of loose and dense packing conditions with confining pressure of 25 and 80 kPa and Silica sand of loose and dense condition with confining pressure of 80 kPa, were selected to observe the evolution of local strain profiles by using DIA technique.

Fig. 4.42 Evolution of local axial strain profile during axial compression loading of D16 sample in loose condition with confining pressure 25 kPa

Fig. 4.43 (a) Failure specimen and selected local elements (b) relationship between local and global axial strain (c) stress ratio of the highest deformed element of D16 sample in loose condition with confining pressure 25 kPa

Fig. 4.44 Evolution of local axial strain profile during axial compression loading of D16 sample in dense condition with confining pressure 25 kPa

Fig. 4.45 (a) Failure specimen and selected local elements (b) relationship between local and global axial strain (c) stress ratio of the highest deformed element of D16 sample in dense condition with confining pressure 25 kPa

Fig. 4.46 Evolution of local axial strain profile during axial compression loading of D16 sample in loose condition with confining pressure 80 kPa

Fig. 4.47 (a) Failure specimen and selected local elements (b) relationship between local and global axial strain (c) stress ratio of the highest deformed element of D16 sample in loose condition with confining pressure 80 kPa

Fig. 4.48 Evolution of local axial strain profile during axial compression loading of D16 sample in dense condition with confining pressure 80 kPa

Fig. 4.49 (a) Failure specimen and selected local elements (b) relationship between local and global axial strain (c) stress ratio of the highest deformed element of D16 sample in dense condition with confining pressure 80 kPa

Fig. 4.50 Evolution of local axial strain profile during axial compression loading of Silica sample in loose condition with confining pressure 80 kPa

Fig. 4.51 (a) Failure specimen and selected local elements (b) relationship between local and global axial strain (c) stress ratio of the highest deformed element of Silica sample in loose condition with confining pressure 80 kPa

Fig. 4.52 Evolution of local axial strain profile during axial compression loading of Silica sample in dense condition with confining pressure 80 kPa
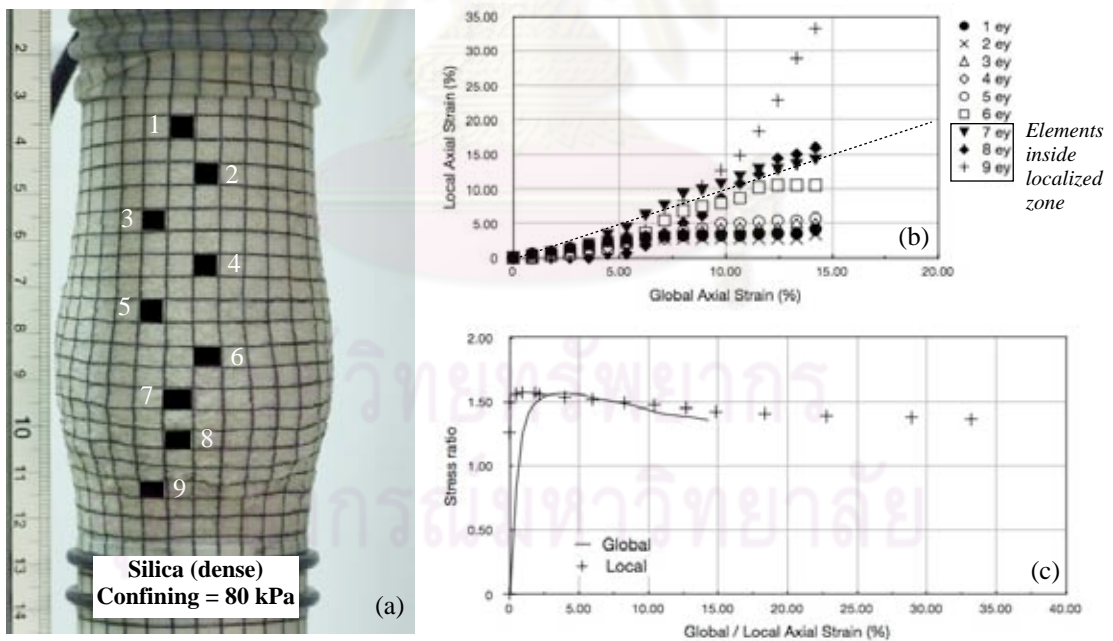
Fig. 4.53 (a) Failure specimen and selected local elements (b) relationship between local and global axial strain (c) stress ratio of the highest deformed element of Silica sample in dense condition with confining pressure 80 kPa

Using the data from digital images, the strain profiles on the surface membrane of the soil specimen could be calculated based on the deformation during the triaxial compression. The strain profiles were developed to illustrate the evolution of localization inside the soil sample. These profiles can explain visually the potential for the initiation of strain localization. In these strain profiles, such as those shown in Fig. 4.42, the vertical strain on the surface of the specimen is displayed and the intensity of gray color at certain point of strain of the profiles represents the magnitude of corresponding axial strain. Fig. 4.42 shows the deformation profile of loose D16 sand specimen sheared under triaxial compression loading conditions at the confining pressure of 25 kPa, which includes the images of specimen and corresponding local axial strain plots at different global axial strain values. The measurement of this variation of local strains could lead to the study of the shear band development and formation within the specimen. In Fig. 4.42, it could be seen that at about 1.77% of global axial strain some local elements of D16 sample exhibit the higher strain ($> 5\%$) than the rest. This strain non-uniformity occurs randomly throughout the specimen. At 3.54% of global axial strain, the sample shows more strain non-uniformity especially at the central portion. Moreover at global strain of 5.31% and so on, this strain non-uniformity develops to form zones of strain localization and these zones distribute along the middle portion of the specimen. It can also be observed that during the entire compression loading the elements outside the localized zone response relatively less value of strain, i.e. $< 5\%$.

Fig. 4.43 also shows the visual inspection of the images of failure specimen and the evolution of local axial strain against global strain. This plot can help in pointing out non-homogeneous of deformation within the specimen. Fig. 4.43(b) shows the progression of local axial strain of selected local elements as in Fig. 4.43(a) against global strain until failure. It can be perceived from Fig. 4.43(b) that elements in the localized zone collect most of the deformation inside the specimen. At failure, the local axial strain of element 3 responses almost 3 times global axial strain. Other elements inside localized zone, i.e. element 4 and 6, also response high value of strain. However, the distribution of axial strain of local elements along the sample is rather uniform. Fig. 4.43(c) shows relationship between the stress ratio versus global /

local axial strain of the highest deformed element inside localized zone. It can be seen that the stress ratio of the highest deformed local element moves along the same path with the global deformation.
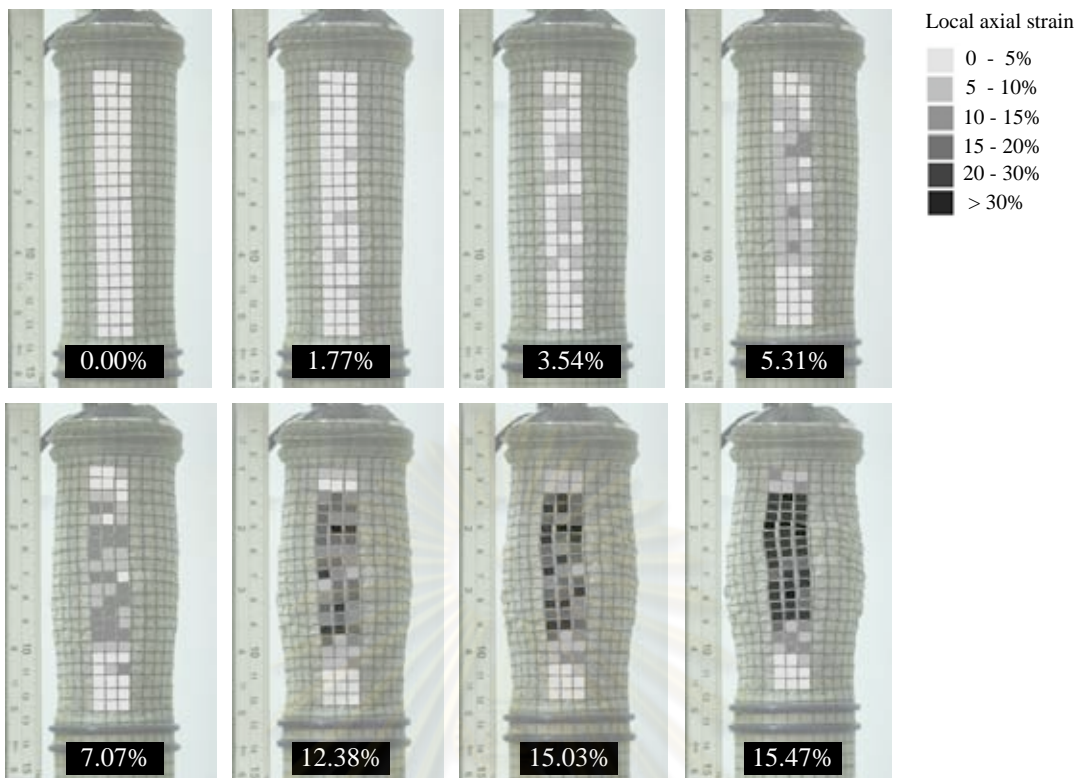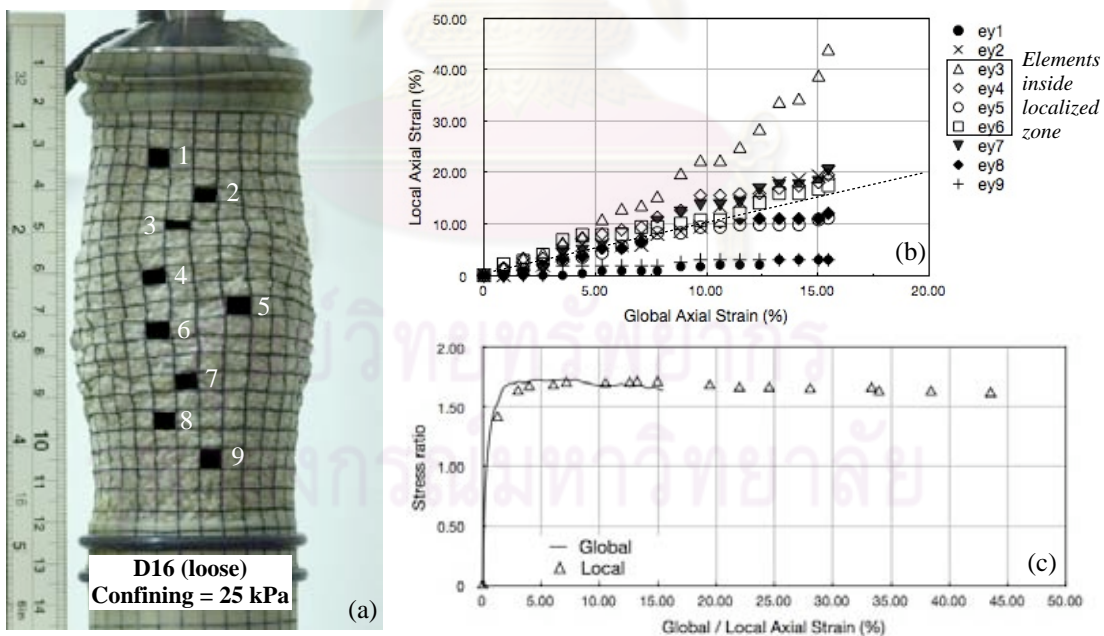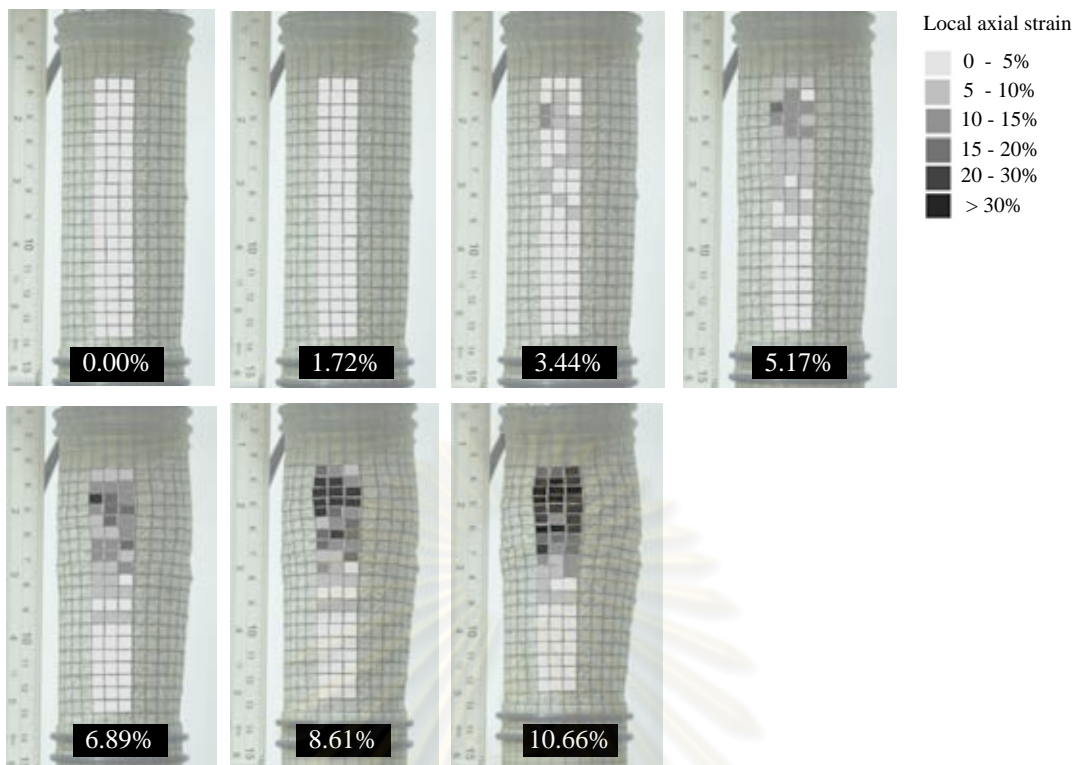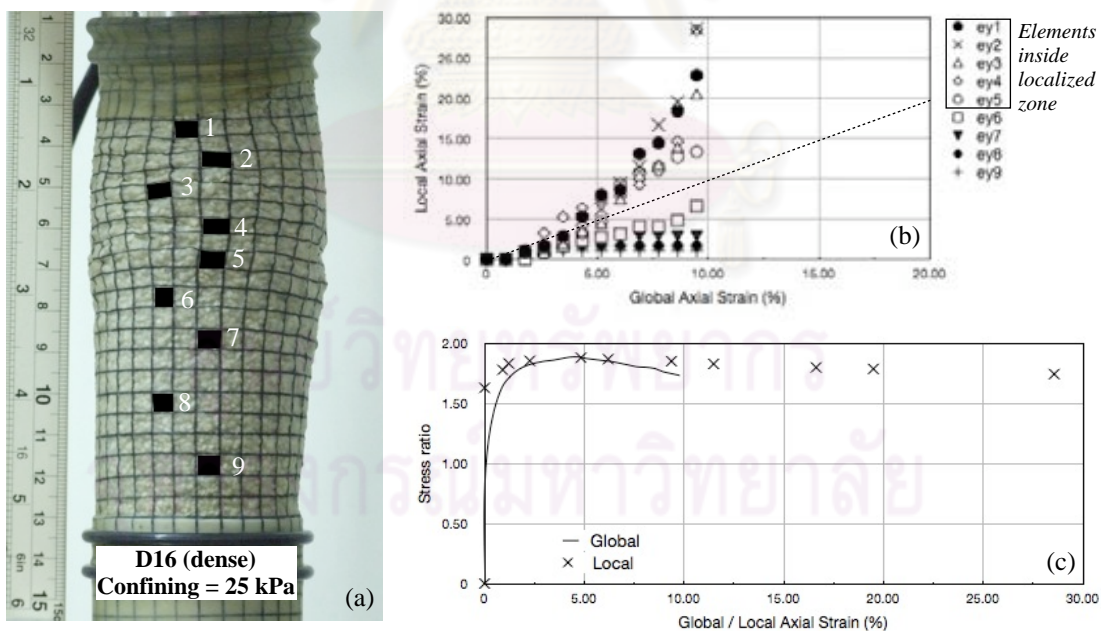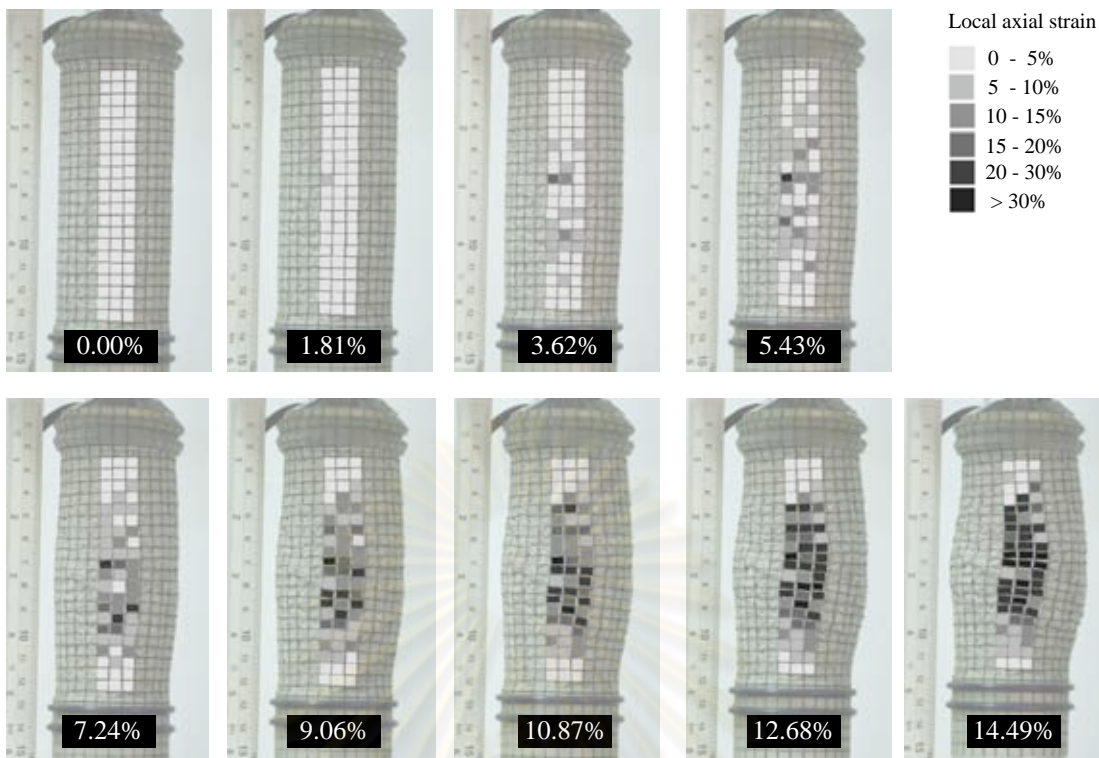
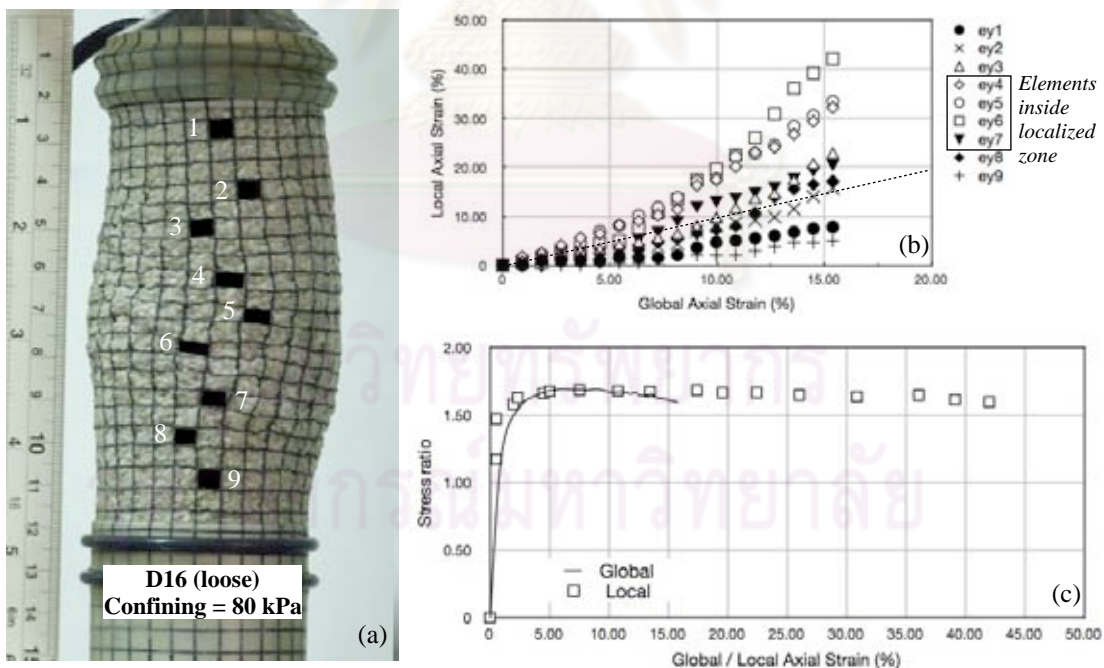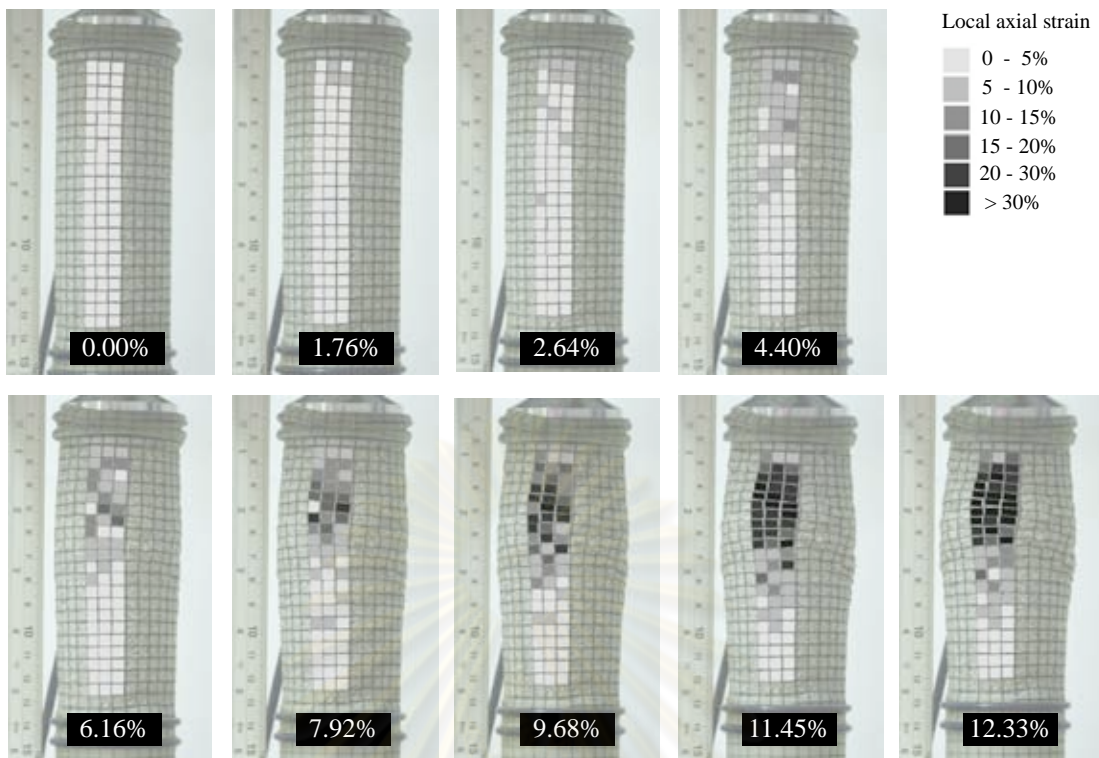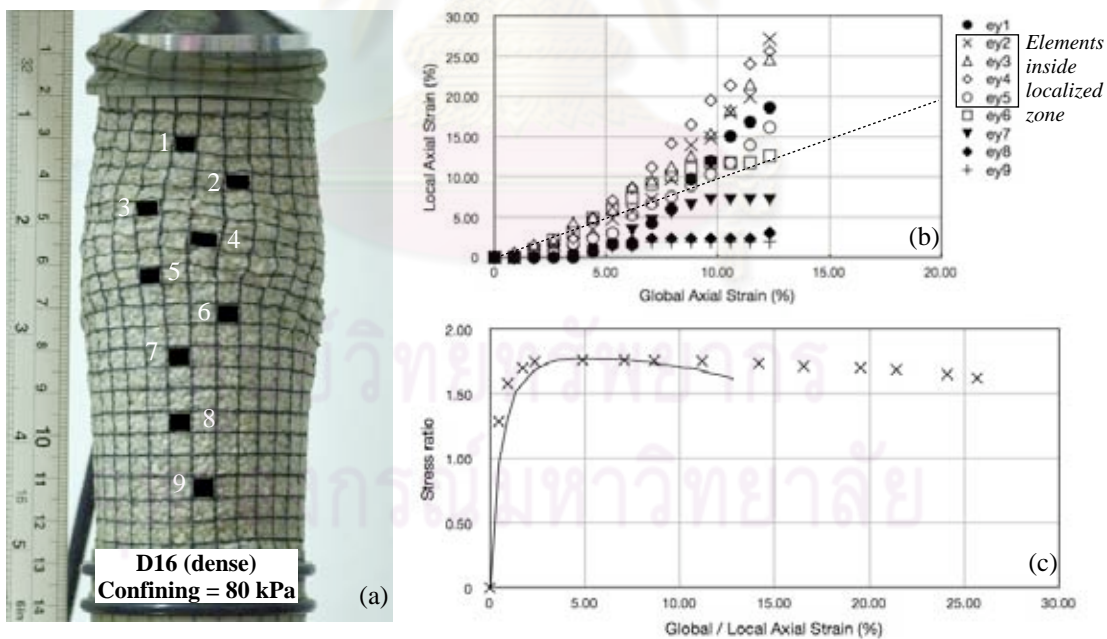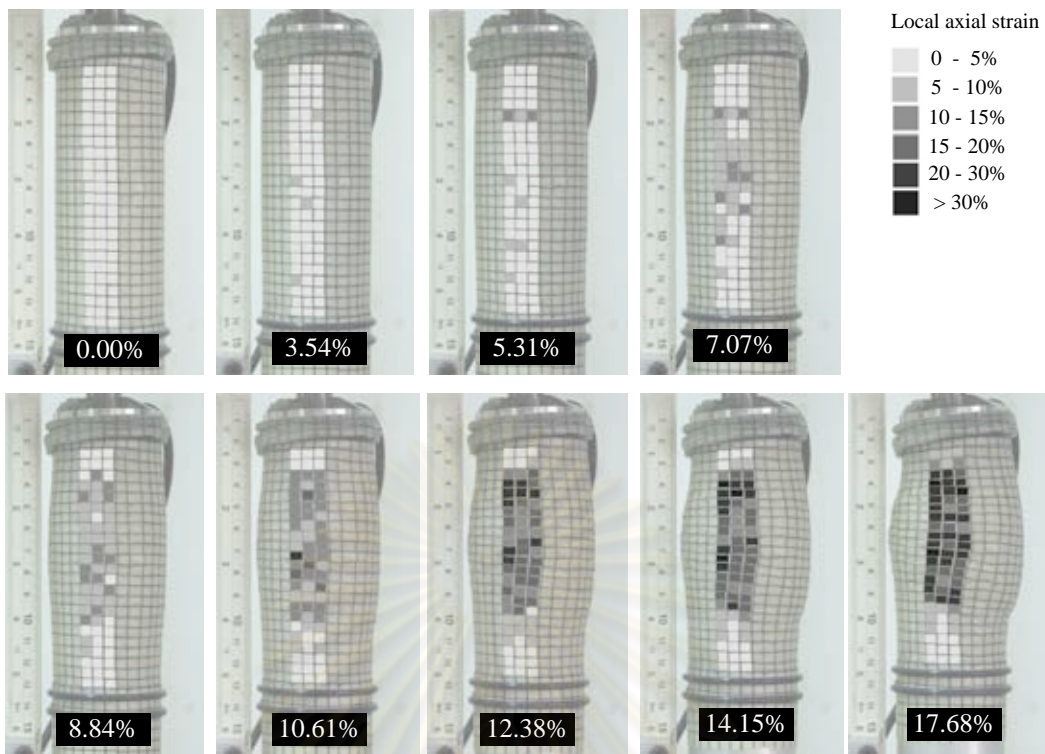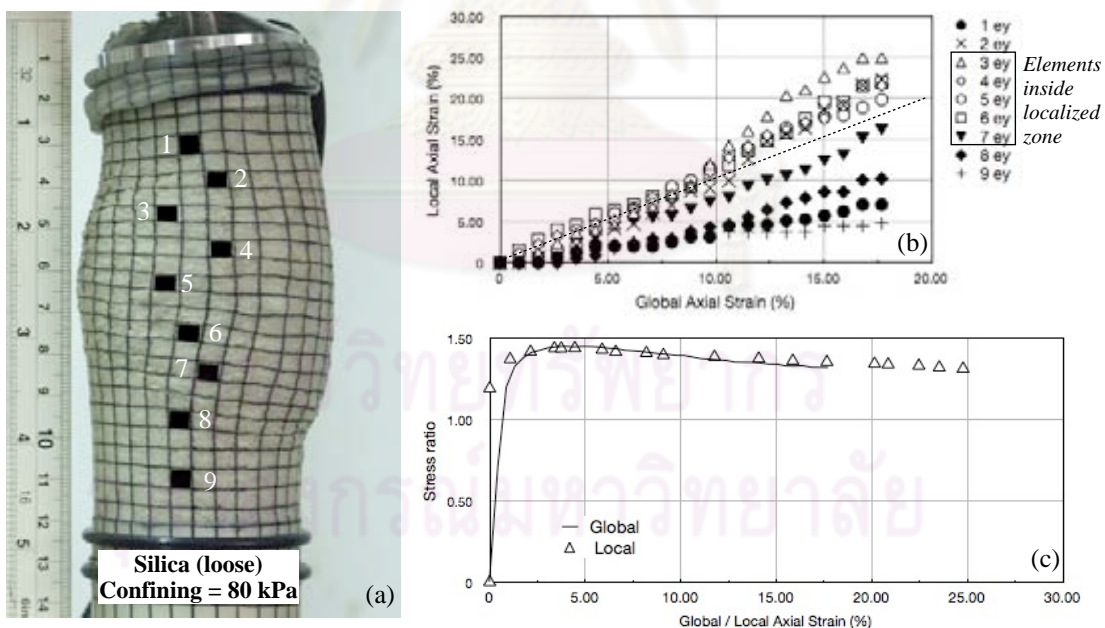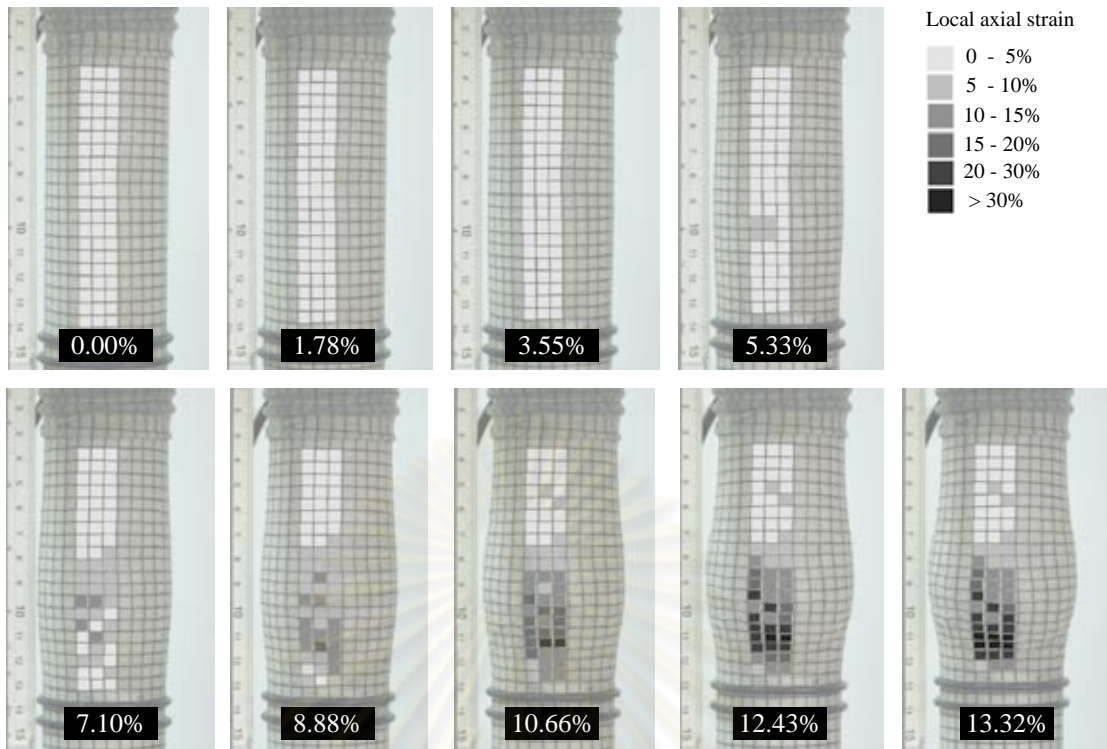Fig. 4.44 shows the evolution of local axial strain profile during axial compression loading of D16 sample in dense condition with confining pressure 25 kPa. The images of local strain profile show that the soil non-homogeneous deformation starts to occur at about 3.44% of global strain and zone of localization fully develops at 5.17% of global axial strain. Comparing to the previous sample of loose packing condition, it might be inferred that dense specimen delayed the strain non-uniformity inside the soil sample. Moreover zone of strain localization of dense specimen is comparatively narrower than loose specimen. Fig. 4.45 also displayed that local axial strain of the highest deformed elements inside the zone of localization have the strain value of nearly 3 times the global axial strain. This behavior confirms a higher deformation characteristic inside the localization zone. The figure also shows that the distribution of strain of local elements along the height of the sample is not uniform as in the loose specimen. The alteration of local strain value of some local elements, i.e. elements 1, 2 and 4, shifts rapidly especially after the onset of soil non-homogeneous (Fig. 4.45b). The stress ratio of the highest deformed local element almost moves along the same path with the global deformation (Fig. 4.45c). Fig 4.46 to 4.53 show the DIA results of D16 and Silica samples in loose and dense conditions with confining pressure of 80 kPa. The similar outcomes could also be attained for these types of samples and testing conditions.

Both observations, i.e. by shear wave velocity profile and DIA, could clarify some important characteristics of strain localization to some extent. Therefore, to explicitly explain the initiation and evolution of strain localization behavior, the pictures illustrating those results from the previous findings would be showed again in Fig. 4.54 to Fig. 4.59. Fig. 4.54 is the comparison results of the stress ratio, shear wave velocity and local strain profile of D16 sample in loose condition with confining pressure 25 kPa. Point a on the stress ratio curve corresponds to the second picture of local strain profile at 1.77% of global axial strain. If we look at the point of maximum V_s at 1.32% of global axial strain, we will see that after this point of $V_{s(max)}$ the onset

of strain non-uniformity inside the specimen will occur. This point of non-uniformity deformation can be confirmed by the appearance of some local elements exhibiting vertical strain to more than 5%. From these figures, it can also be noticed that at the point of maximum stress ratio (MSR) the zone of strain localization will be fully developed (point c).

Fig 4.55 shows the comparison results between stress ratio, shear wave velocity profile and local strain profile of D16 sample in dense condition with confining pressure 25 kPa. Point a on the stress ratio curve is at 3.44% of global strain, at this point some local elements response to non-homogeneous deformation, i.e. >5%, and occurs after the point of maximum shear wave velocity. Point b is the point where the zone of localization is fully progressed and occurs nearly the point of maximum stress ratio. These relevant consequences could be discerned for the tests on D16 sample with loose and dense packing conditions with confining pressure 80 kPa. (Fig. 4.56 and Fig.4.57). However, for Silica sand of loose and dense conditions with confining pressure 80 kPa, the behavior of strain localization from shear wave velocity profile and local strain profile by DIA is not corresponding to each other. Namely, V_s tends to decrease from its maximum value at the very beginning of the test, e.g. 0.88%. However, local strain profile by DIA do not show any non-uniformity deformation within the specimen at this value of global axial strain. The non-uniformity deformation, observing from DIA, starts at about 3.54% and 5.33% of global axial strain for loose and dense sample of Silica sand, respectively. Though DIA can be easily performed to study the strain localization but there are still some limitations and accuracies. On the other hand, shear wave propagation technique can still detect that point of non-uniformity within the soil specimen comprehensibly.
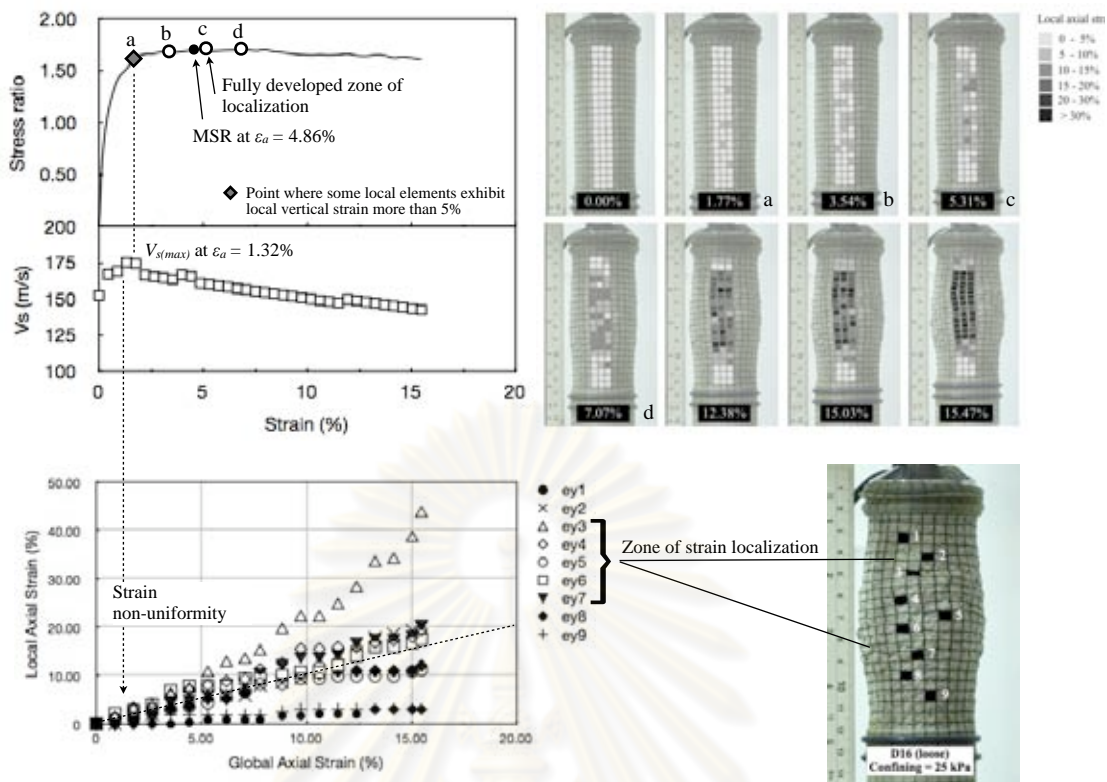
Fig. 4.54 The stress ratio, shear wave velocity and local strain profile of D16 sample in loose condition with confining pressure 25 kPa
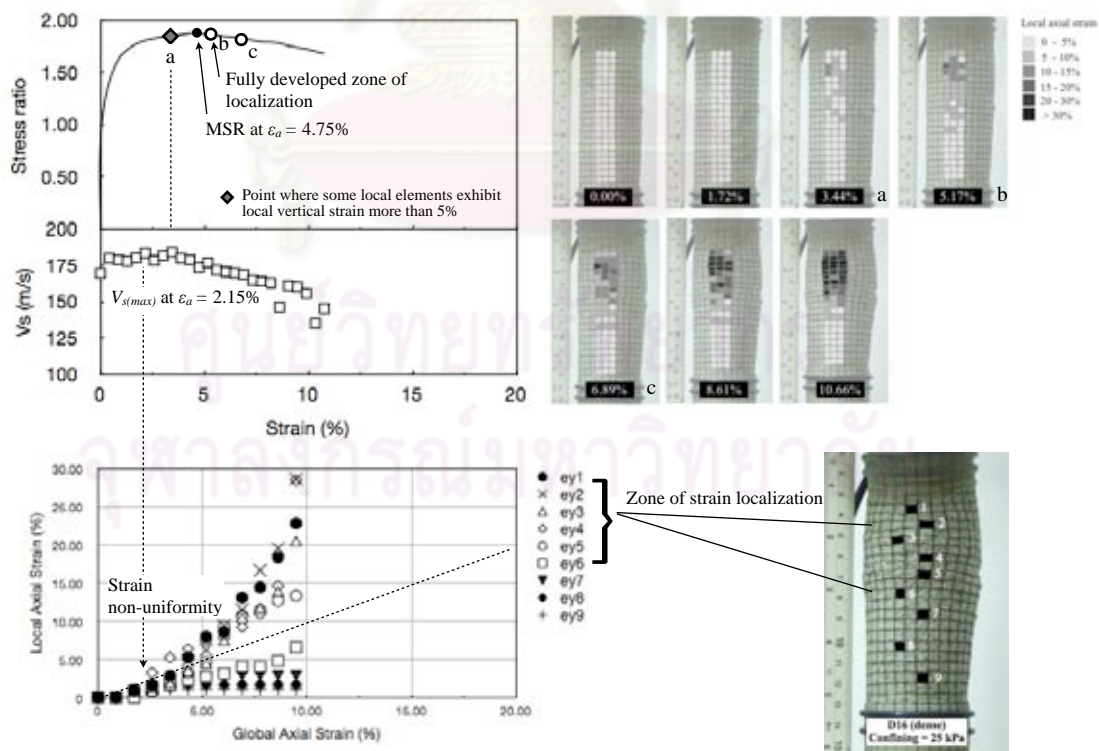
Fig. 4.55 The stress ratio, shear wave velocity and local strain profile of D16 sample in dense condition with confining pressure 25 kPa
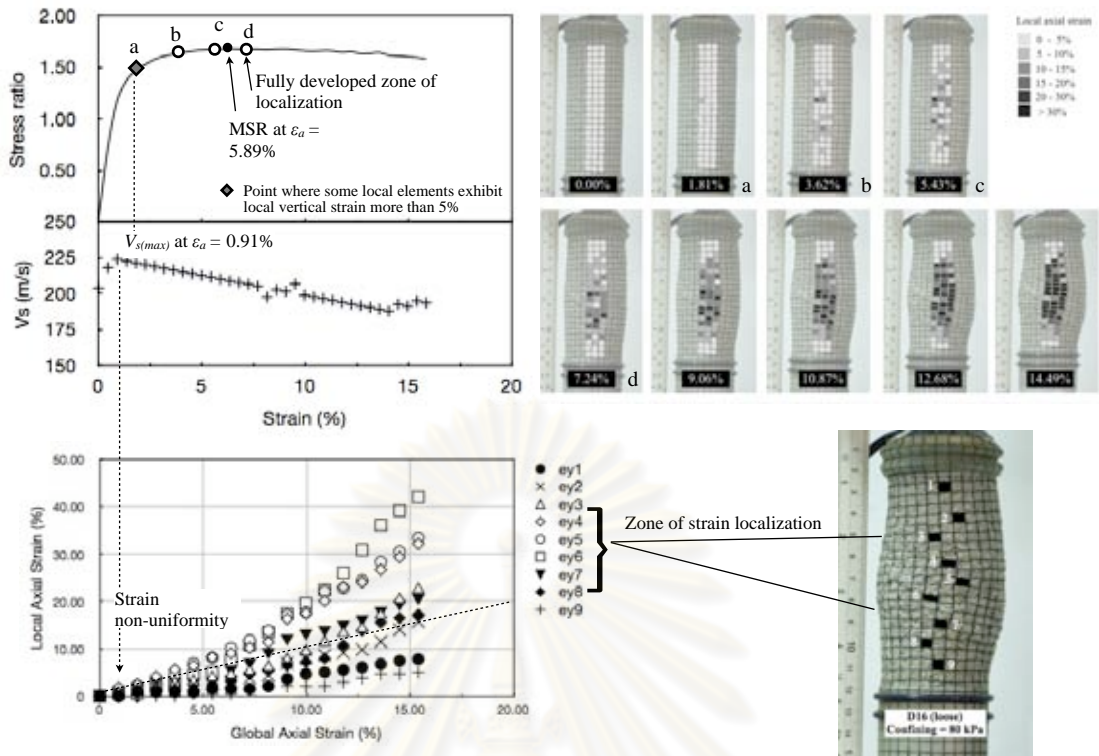
Fig. 4.56 The stress ratio, shear wave velocity and local strain profile of D16 sample in loose condition with confining pressure 80 kPa
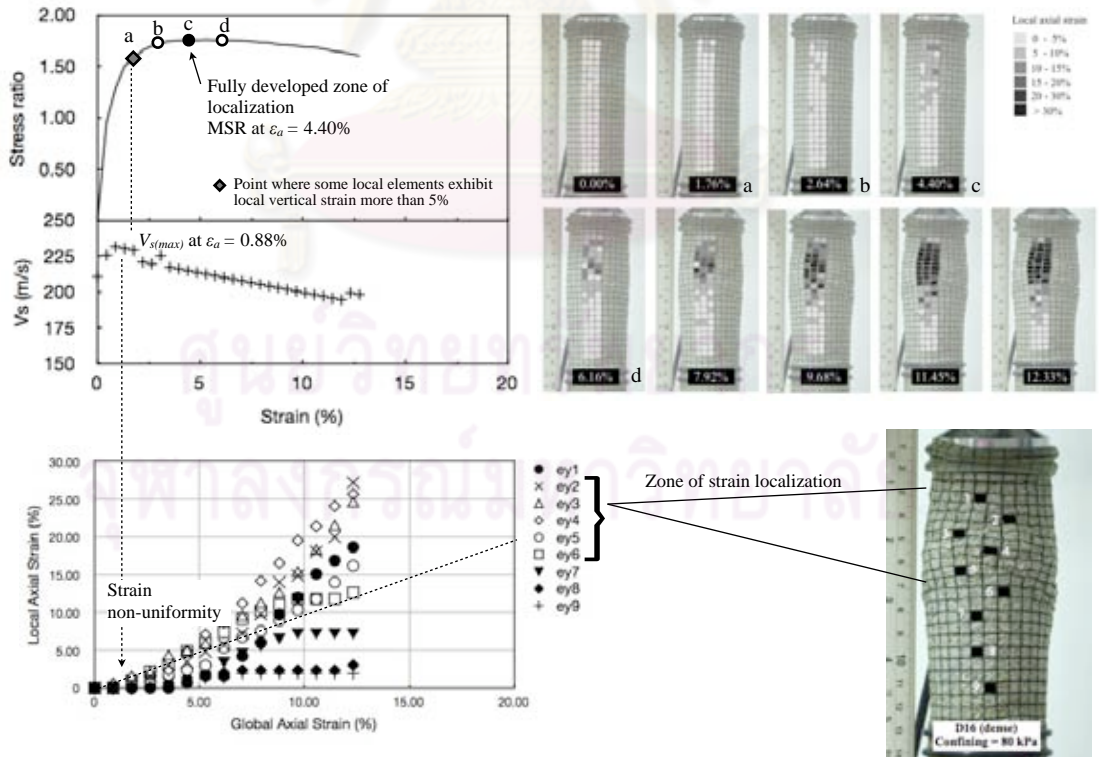
Fig. 4.57 The stress ratio, shear wave velocity and local strain profile of D16 sample in dense condition with confining pressure 80 kPa
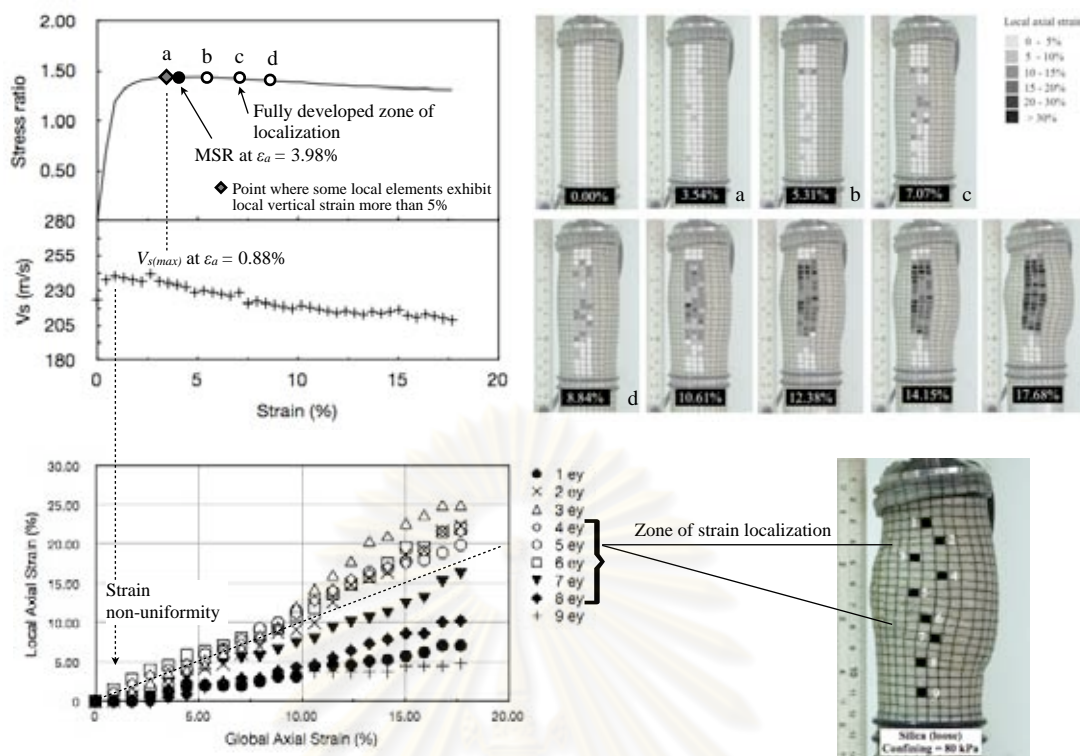
Fig. 4.58 The stress ratio, shear wave velocity and local strain profile of Silica sample in loose condition with confining pressure 80 kPa
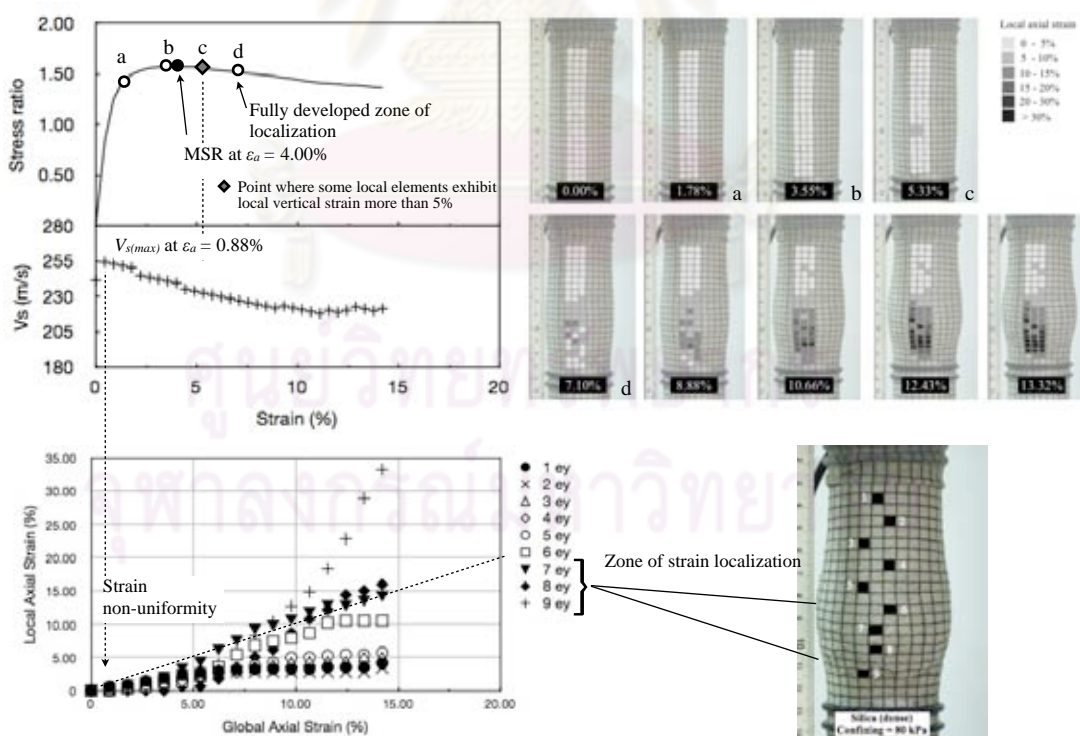
Fig. 4.59 The stress ratio, shear wave velocity and local strain profile of Silica sample in dense condition with confining pressure 80 kPa

CHAPTER V

Conclusions and Recommendations

5.1 Conclusions

The investigation of strain localization of sandy soil samples by using shear wave propagation technique and the Digital Image Analysis (DIA) were performed in the modified triaxial compression test in many packing conditions of sands, i.e. loose and dense state. Local and Silica sands of various grain sizes and shapes were employed in the study. The main results of the study are as follows;

● Shear wave velocity increases as the isotropic confining pressure increases both in loose and dense conditions. The dense samples give slightly higher shear wave velocity than the loose sample at the same confining pressure.

● The propagation of shear wave velocity inside the soils depends primarily on the initial stress state, i.e. packing condition, confining pressure, mechanical response, i.e. contact effects, void ratio coordination number, fabric change as well as the loading history.

● Under shearing stage, the shear wave velocity also increases at the very beginning part of the test. However, at the stress ratio nearly or exceed 1.5, the shear wave velocity tends to decline from its maximum value. Moreover, from the corresponding local strain profile, it can also be seen that the non-uniformity deformation of sample will take place at this point of the reduction of shear wave velocity. We may imply that the onset of strain localization starts from this point.

● At the maximum stress ratio there is no remarkable change of the shear wave velocity. However, the plots of local strain profile show that the strain localization will be fully developed at this stage.

● The formation of strain localization in dense sample exhibits into the narrower zone than in loose sample. In addition, the onset of strain localization in dense sample occurs slower than in loose sample.

5.2 Recommendations for Future Research

● Due to some difficulties in the travel time determination between transmitting and receiving bender elements, a prospective researcher should select a suitable technique to minimize an error of shear wave velocity calculation, i.e. the cross-correlation method.

● The Digital Image Analysis (DIA) of surface membrane of specimen might be clearly observed in plane strain test than in triaxial test because zone of shear band in plane strain test is rather uniform and unique.

● The correlation between void ratio and shear wave velocity before, during and after failure might be clearly established by employing the impregnation technique of tested specimen.

● The local strain profile of the testing sample should be analyzed by the digital image analysis software in order to get more accuracy results.

REFERENCES

Adhikary, D.P. and Dyskin A.V. 1997. A Cosserat continuum model for layered materials. Computers and Geotechnics. 20(1): 15-45.

Agarwal, T.K. and Ishibashi, I. 1991. Multi-Directional wave velocity by piezoelectric crystals, Proceedings of Recent Advances in Instrumentation, Data Acquisition and Testing in Soil Dynamics (GSP 29). ASCE: 102-117. Florida. October 20-24, 1991.

Aifantis, E.C. 1984. On the microstructural origin of certain inelastic models. Journal of Engineering Materials and Technology. 106(4): 326-330. ASME.

Aifantis, E.C. 1987. The physics of plastic deformation. International Journal of Plasticity. 3: 211-247.

Alshibli, K.A. 1995. Localized deformations in granular materials. Ph.D Dissertation, University of Colorado at Boulder, Colorado.

Alshibli, K.A. and Sture S. 1999. Sand Shear Band Thickness Measurement by Digital Image Techniques. Journal of Computing in Civil Engineering. 13(2): 103-109. ASCE.

Alshibli, K.A. and Sture S. 2000. Shear Band Formation in Plane Strain Experiments of Sand. Journal of Geotechnical and Geoenvironmental Engineering. 126 (6): 495-503. ASCE.

Alshibli, K.A., Sture, S., Costes, N.C., Frank, M.L., Lankton, M.R., Batiste, S.N., and Swanson, R.A. 2000. Assessment of localized deformations in sand using X - Ray computed tomography, Geotechnical Testing Journal. 23(3): 274-299.

Alshibli, K.A., Batiste, S.N., and Sture, S. 2003. Strain Localization in Sand: Plane Strain versus Triaxial Compression. Journal of Geotechnical and Geoenvironmental Engineering. (129)6: 483-494. ASCE.

Arroyo, M., Muir Wood, D., and Greening, P.D. 2003. Source near-field effects and pulse tests in soil samples. Géotechnique. 53(3): 337-345.

Arroyo, M., Muir Wood, D., Greening, P.D., Medina, L., and Rio, J. 2006. Effects of sample size on bender-based axial G_0 measurements. Géotechnique. 56(1): 39-52.

Arthur, J., Dunstan, T., Al-ani, Q., and Assadi A. 1977. Plastic deformation and failure in granular media. Géotechnique. 27(1): 53-74.

Arthur, J. and Dunstan, T. 1982. Rupture layers in granular media. in Vermeer P.A. and Luger H.J. (Eds). Proceedings of IUTAM Conference Deformation and Failures of Granular Materials, 453-459. Rotterdam, The Netherlands: Balkema.

Arulnathan, R., Boulanger, R.W., and Riemer, M.F. 1998. Analysis of bender element test. Geotechnical Testing Journal. 21(2): 120–131.

Bardet, J.P. 1990. A comprehensive review of strain localization in elastoplastic soils. Computer and Geotechnics. (10)3: 163-188.

Bates, C.R. 1989. Dynamic soil property measurements during triaxial testing. Géotechnique. 39(4): 712-726.

Batiste, S.N., Alshibli, K.A., Sture S. and Lankton, M. 2004. Shear band characterization of triaxial sand specimens using computed tomography. Geotechnical Testing Journal. 27(6): 568-579.

Bauer, E. 1996. Calibration of a comprehensive hypoplastic model for granular materials. Soils and Foundations. 36(1): 13-26.

Bauer, E. 1999. Analysis of shear band bifurcation with a hypolastic model for a pressure and density sensitive granular material. Mechanics of Materials. 31: 597-609.

Bellotti, R., Jamiolkowski, M., Lo Presti, D. C. F., and O'Neill, D.A. 1996. Anisotropy of small strain stiffness in Ticino sand. Géotechnique. 46(1): 115-131.

Benallal, A. and Comi C. 2003. Perturbation growth and localization in fluid-saturated inelastic porous media under quasi-static loadings. Journal of the Mechanics and Physics of Solids. 51: 851-899.

Bésuelle, P., Desrues, J., and Rained S. 2000. Experimental characterisation of the localization phenomenon inside a vosges sandstone in a triaxial cell. International Journal of Rock Mechanics and Mining Sciences. 37: 1223-37.

Blewett, J., Blewett, I. J., and Woodward, P. K. 1999. Measurement of shear-wave velocity using phase-sensitive detection techniques. Canadian Geotechnical Journal. 36(5): 934-939.

Brignoli, E.G.M., Gotti, M., and Stokoe, K.H., II. 1996. Measurement of shear waves in laboratory specimens by means of piezoelectric transducers. <u>Geotechnical Testing Journal</u>. 19(4): 384-397.

Brocanelli, D. and Rinaldi, V. 1998. Measurement of Low-Strain Material Damping and Wave Velocity with Bender Elements in the Frequency Domain. <u>Canadian Geotechnical Journal</u>. 35(6): 1032-1040.

Butterfield, R., Harkness, R.M., and Andrews, K.Z. 1970. A stereo-photogrammetric method for measuring displacements fields. <u>Géotechnique</u>. 20(3):308-314.

Cascante, G. and Santamarina, J.C. 1996. Interparticle Contact Behavior and Wave Propagation. <u>Journal of Geotechnical Engineering</u>. (122)10: 831-839. ASCE.

Chambon, R., Crochepeyre S., and Desrues J. 2000. Localization criteria for nonlinear constitutive equations of geomaterials. <u>Mechanics of Cohesive-Frictional Materials</u>. 5: 561-582.

Chambon, R., Caillerie, D., and Matsuchima, T. 2001. Plastic continuum with microstructure, local second gradient theories for geomaterials: Localization studies. <u>International Journal of Solids and Structures</u>. 38: 8503-8527.

Chau, K.T. 1992. Non-normality and bifurcation in a compressible pressure-sensitive circular cylinder under axisymmetric tension and compression. <u>Journal of Solids Structures</u>. 29(7): 801-824.

Cheng, S.Y., Ariaratnam, S.T., and Dubey, R.N. 1971. Axisymmetric bifurcation in an elastic-plastic cylinder under axial load and lateral hydrostatic pressure. <u>Quaterly of Applied Mathematics</u>. 29: 41-51.

Desrues, J., Lanier, J., and Stutter P. 1985. Localization of the deformation in tests on sand sample. <u>Engineering Fracture Mechanics</u>. 21: 909-921.

Desrues, J. and Chambon R. 1989. Shear band analysis for granular materials: the question of incremental nonlinearity. <u>Ingenieur Archiv</u>. 59: 187-196.

Desrues, J. and Hammad, W. 1989. Shear band dependency on mean stress level in sand. in Dembicki, E., Gudehus, G., and Sicker, Z. (Eds). 2nd <u>International Workshop on Numerical Methods for Localization and Bifurcation of Granular Bodies</u>, 57-67. Technical University of Gdansk: Gdansk, Poland.

Desrues, J. 1990. Shear Band Initiation in Granular Materials: Experimentation and Theory. Geomaterials: Constitutive Equations and Modeling. 283-310. Elsevier: Routledge, UK.

Desrues, J., Chambon, R., Mokni, M., and Mazerolle F. 1996. Void ratio evolution inside shear bands in triaxial sand specimens studied by computed tomography. Géotechnique. 46(3): 529-546.

Desrues, J. 1998. Localization Patterns in ductile and brittle geomaterials. in Material Instabilities in Solids, René de Borst and Erik van der Giessen (Eds). Wiley-Interscience-Europe. 137-158

Desrues, J. and Chambon R. 2002. Shear bands analysis and shear moduli calibration. International Journal of Solids and Structures. 39(13-14), 3757-3776.

Desrues, J. and Viggiani G. 2004. Strain localization in sand: an overview of the experimental results obtained in Grenoble using stereophotogrammetry. International Journal for Numerical and Analytical Methods in Geomechanics. 28(4): 279-321.

Desrues, J. 2004. Tracking strain localization in geomaterials using computerized tomography. in Omani, J. and Obara, Y. (Eds). Proceedings of the International Workshop on X-ray CT for Geomaterials, 15-41. International Workshop on X-ray CT for Geomaterials, November 6-7, 2003. Kumamoto, Japan. Balkema.

Dyvik, R. and Madshus, C. 1985. Laboratory measurement of G_{max} using bender element. Proceedings of ASCE Annual Convention: Advance in the Art of Testing Soils under Cyclic Conditions, 186 – 96.89 (SM1): 33-65. Detroit.

Ehlers, W. and Volk, W. 1997. On shear band localization phenomena of liquid-saturated granular elastoplastic porous solid materials accounting for fluid viscosity and micropolar solid rotations. Mechanics of cohesive-frictional materials. 2: 301-320.

Ehlers, W. and Volk, W. 1998. On theoretical and numerical methods in the theory of porous media based on polar and non-polar elastoplastic solid materials. International Journal of Solids and Structures. 35 (34-35): 4597-4617.

Finno, R., Harris, W., Mooney, M., and Vagina G. 1996. Strain localization and undrained steady state of sands. Journal of Geotechnical Engineering. 122(6): 462-473. ASCE.

Finno, R., Harris, W., Mooney, M., and Vagina G. 1997. Shear bands in plane strain compression of loose sand. Géotechnique 47(1): 149-165.

Frost J.D. and Deh-Jeng Jang. 2000. Evolution of Sand Microstructure during Shear. Journal of Geotechnical and Geoenvironmental Engineering. (126)2: 116-130. ASCE.

Gajo, A., Fedel, A., and Mongiovi, L. 1997. Experimental analysis of the effects of fluid-solid coupling on the velocity of elastic waves in saturated porous media. Géotechnique, 47(5): 993-1008.

Han, C. and Vardoulakis I. 1991. Plane-strain compression experiments on water-saturated fine-grained sand. Géotechnique. 41(1): 49-78.

Hardin, B.O. and Richart, F.E. 1963. Elastic Wave Velocities in Granular Soils. Journal of Soil Mechanics and Foundations Division. (89)SM1: 33-65. ASCE.

Hardin, B.O. and Drnevich, V.P. 1972. Shear modulus and damping in soils: measurements and parameter effects. Journal of Soil Mechanics and Foundations Division. Terzaghi Leture, 98(6): 603-624.

Hicher, P.Y., Wahyudi, H., and Tessier, D. 1994. Microstructural analysis of strain localisation in clay. Computers and Geotechnics. 16: 205-222.

Huang, W., Nubel, K., and Bauer, E., 2002. Polar extension of a hypoplastic model for granular materials with shear localization. Mechanics of Materials. 34(9): 563-576.

Huang, W. and Bauer, E. 2003. Numerical investigations of shear localization in a micro-polar hypoplastic material. International Journal for Numerical and Analytical Methods in Geomechanics. 27(4): 325-352.

Ikeda, K., Murota, K., Yamakawa, Y., and Yanagisawa, E. 1997. Mode switching and recursive bifurcation in granular materials." Journal of the Mechanics and Physics of Solids. 45(11/12): 1929-1953.

Ishihara, K. 1996. Soil Behaviour in Earthquake Geotechnics. Oxford University Press. 360 pages.

Iwasaki, T., Tatsuoka, F., and Takagi, Y. 1978. Shear moduli of sands under cyclic torsional shear loading. Soils and Foundations. 18(1): 39-56.

Jovicic, V., Coop, M.R., and Simic, M. 1996. Objective criteria for determining G_{max} from bender element tests. Géotechnique. 46(2): 357-362.

Kanatani, K.I. 1979. A Micropolar continuum theory for the flow of granular materials. International Journal of Engineering Science. 17: 419-432.

Kawaguchi, T., Mitachi, T., and Shibuya, S. 2001. Evaluation of shear wave travel time in laboratory bender element test. Proceedings of the 15th International Conference on Soil Mechanics and Geotechnical Engineering, 155-158. Istanbul.

Kumar, J., and Madhusudhan, B. N. 2010 A note on the measurement of travel times using bender and extender elements. Soil Dynamics and Earthquake Engineering. 30(2010): 630–634.

Lade, P.V. and Duncan, J.M. 1973. Cubical triaxial tests on cohesionless soil. Journal of Soil Mechanics and Foundations Division. 99(SM10): 793-812. ASCE.

Lade, P.V. 2002. Instability, shear banding and failure in granular materials. International Journal of Solids and Structures. 39: 3337-3357.

Lam, W.K. and Tatsuoka, F. 1988. Triaxial compression and extension strength of sand affected by strength anisotropy and sample slenderness. Advance in Triaxial Testing of Soil and Rock, 655-666. ASTM STP 977. Philadelphia.

Lawrence, F.V. 1963. Propagation of Ultrasonic Waves Through Sand. Research Report R63-08. Massachusetts Institute of Technology: Boston.

Lawrence, F.V. 1965. Ultrasonic Shear Wave Velocity in Sand and Clay, Research Report R65-05. Massachusetts Institute of Technology: Boston.

Lee, K. 1970. Comparison of plane strain and triaxial tests on sand. Journal of Soil Mechanics and Foundations Division. 96(3): 901-923. ASCE.

Lee J.S. and Santamarina J.C. 2005. Bender Elements: Performance and Signal Interpretation. Journal of Geotechnical and Geoenvironmental Engineering. 131(9): 1063-1070.

Leong, E.C., Yeo, S.H., and Rahardjo, H. 2005. Measuring shear wave velocity using bender elements. Geotechnical Testing Journal. 28(5): 488-498.

Marachi, N., Duncan, J., Chan, C., and Seed, H. 1981. Plane-strain testing of sand.'' Laboratory shear strength of soils, ASTM STP 740, R. N. Yong, and F. C. Townsend, eds., ASTM, 294-302.

Minsu Cha and Gye-Chun Cho. 2007. Shear strength estimation of sandy soils using shear wave velocity. Geotechnical Testing Journal. 30(6): 484-495.

Mokni, M. and Desrues J. 1999. Strain localisation measurements in undrained plane- strain biaxial tests on Hostun RF sand. Mechanics of Cohesive-Frictional Materials. 4: 419-441.

Mooney, M.A. 1996. An experimental study of strain localization and the mechanical behavior of sand. Ph.D Thesis, Northwestern University, Evanston, Illinois.

Mühlhaus, H.-B. and Vardoulakis, I. 1987. The thickness of shear bands in granular materials. Géotechnique. 37: 271-283.

Mühlhaus, H.-B. and Hornby, P. 2001. Energy and averages in the mechanics of granular materials. Tectonophysics. 335: 63-80.

Nakai, T. and Matsuoka, H. 1983. Shear behavior of sand and clay under three-dimensional stress condition. Soils and Foundations. 23(2): 26-47.

Oda, M. 1972b. The Mechanism Fabric Changes during Compressional Deformation on Sand. Soils and Foundations. 12(2): 1-18.

Oda, M., Iwashita, I., and Kazama, H. 1996. Micro-structure developed in shear band of dense granular soils and its computer simulation - mechanisms of dilatancy and failure. IUTAM symposium on Mechanics of Granular and Porous Materials. UK 96: 353-364.

Oda, M., Kazama, H., and Konishi, J. 1998. Effects of induced anisotropy on the development of shear bands in granular materials. Mechanics of Materials. 28: 103-111.

Oda, M. and Kazama, H. 1998. Microstructure of shear bands and its relation to the mechanisms of dilatancy and failure of dense granular soils. Géotechnique. 48(4): 465-481.

Oda, M. and Iwashita, I. 1999. Mechanics of Granular Materials: An Introduction. A. A. Balkema: The Netherlands.

Oka, F., Jiang, M., and Higo, Y. 2001. Gradient dependent viscoplastic constitutive models and strain localization analysis of water saturated cohesive soil. Computer Methods and Advances in Geomechanics, 519-524.

Parry R.H.G. 1995. Mohr Circles, Stress Paths and Geotechnics, E & FN SPON, 230 pages

Pasternak, E. and Mühlhaus, H.-B. 2001. Cosserat continuum modeling of granulate materials. Computational Mechanics – New Frontiers for New Millennium, 1189-1194.

Pasternak, E. and Mühlhaus, H.-B. 2002. Large deformation Cosserat continuum modeling of granulate materials. Proceedings of the third Australasian Congress on Applied Mechanics, Applied Mechanics: Progress and Applications, 389-396.

Pennington, D.S., Nash, D.F.T., and Lings, M.L. 2001. Horizontally mounted bender elements for measuring anisotropic shear moduli in Triaxial clay specimens. Geotechnical Testing Journal. 24(2): 133-144.

Peters, J., Lade, P., and Bro, A. 1988. Shear band formation in triaxial and plane strain tests. in Donaghe, R., Chaney, R., and Silver, M. (Eds). Advanced Triaxial Testing of Soil and Rock, 604-627. ASTM, STP 977.

Rechenmacher, A.L. and Finno, R.J. 2004. Digital image correlation to evaluate shear banding in dilative sands. Geotechnical Testing Journal. 27(1): 13-22.

Rained S., Faber D., Frédéric M., Geraud Y., and Later H.J. 1989. Analysis of the internal structure of rocks and characterization of mechanical deformation by a non-destructive method: X-ray tomodensitometry. Tectonophysics. 159(1-2): 149-159.

Reades, D.W. and Green, G.E. 1976. Independent stress control and triaxial extension tests on sand. Géotechnique. 26(4): 551-576.

Richart, F.E., Hall, J.R., and Woods, R.D. 1970. Vibrations of Soils and Foundations. Prentice-Hall, Englewood Cliffs, N.J.

Ristinmaa, M. and Vecchi, M. 1996. Use of couple-stress theory in elasto-plasticity. Computer Method in Applied Mechanics and Engineering. 136: 205-224.

Roesler, S.K. 1979. Anisotropic shear modulus due to stress anisotropy. Journal of Soil Mechanics and Foundations Division. 105(7): 871-880.

Roger, V., Desrues, J., and Vagina, G. 1998. Experiments on strain localisation in dense sand under isotropic conditions. Localisation and Bifurcation Theory for Soils and Rocks, 239-248. 4th Workshop on Localization and Bifurcation Theory for Soils and Rocks, 28 September - 2 October 1997, Gifu, Japan.

Roscoe, K.H., Schofield A.N., and Thurairajah A. 1963. An evaluation of test data for selecting a yield criterion for soils. Laboratory Shear Testing of Soils. STP No. 3. ASTM: Philadelphia, PA.

Roscoe, K.H. 1970. The influence of strains in soil mechanics. Géotechnique. 20(2): 129-170.

Rowe, P.W. 1962. The stress-dilatancy relation for static equilibrium of an assembly of particles in contact. Proceedings of the Royal Society of London, series A, Mathematical and Physical Sciences (1934-1990). Volume 269 Number 1339.

Saada, A.S., Liang, L., Figueroa, J.L., and Cope, C.T. 1999. Bifurcation and shear band propagation in sands. Géotechnique. 49(3): 367-385.

Sachan, A. and Penumadu, D. 2007. Strain localization in solid cylindrical clay specimens using Digital Image Analysis (DIA) technique. Soils and Foundations. 47(1): 67-78.

Sanchez-Salinero, I., Roesset, J.M., and Stokoe, K.H. 1986. Analytical studies of body wave propagation and attenuation. Report GR 86-15. Civil Engineering Department, University of Texas at Austin, TX.

Santamarina, J.C. and Fam, M.A. 1997. Interpretation of bender element tests (Discussion). Géotechnique, 47(4): 873-877.

Santamarina J.C., Klein K.A., and Fam, M.A. 2001. Soils and Waves: Particulate Materials Behaviour, Characterisation and Process Monitoring. J. Wiley & Sons, 508 pages.

Santamarina, J.C. and Cascante, G. 1996. Stress anisotropy and wave propagation - A micromechanical view. Canadian Geotechnical Journal. 33(5): 770-782.

Schrefler, B., Sanavia, L., and Majorcan C. 1996. A multiphase medium model for localization and post localisation simulation in geomaterials. Mechanics of Cohesive-Frictional Materials. 1: 95-114.

Shi, M.X., Huang, Y., and Hwang, K.C. 2000. Plastic flow localization in mechanism-based strain gradient plasticity. International Journal of Mechanical Sciences. 42: 2115-2131.

Shirley, D. J. 1978. An improved shear wave transducer. Journal of Acoustic Society of America. 63(5), 1643-1645.

Stokoe, K.H. II, Hwang, S.K., Lee, J.N.K., and Andrus, R.D. 1995. Effects of various parameters on the stiffness and damping of soils at small to medium strains. in Shibuya et al. (Eds). Proceedings of the International Symposium on Pre-failure Deformation of Geomaterials. 2: 785-816.

Sulem, J. and Vardoulakis, I. 1990. Bifurcation analysis of the triaxial test on rock specimens: A theorietical model for shape and size effect. Acta Mechanica. 83: 195-212.

Tamagnini, C., Viggiani, G., and Chambon, R. 2000. A review of two different approaches to hypoplasticity. in Kolymbas, D. (Ed.) Constitutive Modeling of Granular Materials, 107-145. Springer: Berlin.

Tamagnini, C., Viggiani, G., and Chambon, R. 2001. Some remarks on shear band analysis in hypoplasticity. in Mühlhaus, Dyskin and Pasternak (Eds). 5th International Workshop on Localisation and Bifurcation Theory in Geomechanics, 85-93. Balkema Publisher.

Tan, S. and Fwa, T. 1991. Influence of voids on density measurements of granular materials using gamma radiation techniques. Geotechnical Testing journal. 14(3): 257-265.

Tatsuoka, F., Sakamoto, M., Kawamura, T., and Fukushima S. 1986. Strength and deformation characteristics of sand in plane strain compression at extremely low pressures. Soils and Foundations. 26(1): 65-84.

Tatsuoka, F., Nakamura, T., Huang, C., and Tani K. 1990. Strength anisotropy and shear band direction in plane strain test of sand. Soils and Foundations. 30(1): 35-54.

Teachavorasinskun, S. and Akkarakun, T. 2004. Paths of elastic shear modulus of clays," Géotechnique. 54(5): 331-333.

Teachavorasinskun, S. and Amornwithayalax, T. 2002. Elastic shear modulus of Bangkok clay during undrained triaxial compression. Géotechnique. 52(7): 537-540.

Tejchman, J. and Bauer E. 1996. Numerical Simulation of Shear Band Formation with a Polar Hypoplastic Constitutive Model. Computers and Geotechnics. 19(3): 221-244.

Tejchman, J. and Wu, W. 1996. Numerical simulation of shear band formation with a hypoplastic constitutive model. Computers and Geotechnics. 18(1): 71-84.

Tejchman, J. and Gudehus, G. 2001. Shearing of a narrow granular layer with polar quantities. International Journal for Numerical and Analytical Methods in Geomechanics. 25: 1-28.

Tejchman, J. and Poland, G. 2001. Patterns of shear zones in granular bodies within a polar hypoplastic continuum. Acta mechanica. 1-24.

Vardoulakis, I. 1977. Scherfugenbildung in Sandkörpern als Verzweigungsproblem. Ph.D Thesis (Nr. 77), Institute for Soil and Rock Mechanics, University of Karlsruhe.

Vardoulakis, I., Goldscheider, M., and Gudehus, G. 1978. Formation of shear bands in sand bodies as a bifurcation problem. International Journal for Numerical and Analytical Methods in Geomechanics. 2(2): 99-128.

Vardoulakis, I. 1979. Bifurcation analysis of the triaxial test on sand samples. Acta mechanica. 32: 35-54.

Vardoulakis, I. 1980. Shear band inclination and shear modulus of sand in biaxial tests. International Journal for Numerical and Analytical Methods in Geomechanics. 4: 103-119.

Vardoulakis, I. 1981. Constitutive properties of dry sand observable in the triaxial test. Acta mechanica. 38: 219-239.

Vardoulakis, I. 1983. Rigid granular plasticity model and bifurcation in the triaxial test. Acta mechanica, 49: 57-79.

Vardoulakis, I. and Graf B. 1985. Calibration of constitutive models for granular materials using data from biaxial experiments. Géotechnique. 35(3): 299-317.

Vardoulakis, I. 1989. Shear-band and liquefaction in granular materials on the basis of Cosserat continuum theory. Ingenieur-Archiv. 59: 106-113.

Vardoulakis, I. and Aifantis, E.C. 1989. Gradient dependent dilatancy and its implications in shear banding and liquefaction. Ingenieur-Archiv. 59: 197-208.

Vardoulakis, I. and Aifantis, E.C. 1991. A gradient flow theory of plasticity for granular materials. Acta mechanica. 87: 197-217.

Vardoulakis, I. and Sulem, J. 1995. Bifurcation Analysis in Geomechanics. Blackie Academic and Professional: Chapman & Hall, 462 pages.

Vardoulakis, I. 1996a. Deformation of water-saturated sand: I. Uniform undrained deformation and shear banding. Géotechnique. 46(3): 441-456.

Vardoulakis, I. 1996b. Deformation of water-saturated sand: II. Effect of pore water flow and shear banding. Géotechnique. 46(3): 457-472.

Vermeer P.A. 1982. A simple shear band analysis using compliances. in Vermeer P.A. and Luger H.J. (Eds). Proceedings of IUTAM Conference Deformation and Failures of Granular Materials, 493-499. Rotterdam, The Netherlands: Balkema.

Viggiani, G., Küntz, M., and Desrues, J. 2001. An experimental investigation of the relationships between grain size distribution and shear banding in sand. Continuous and Discontinuous Modeling of Cohesive-Frictional Materials. Springer: Lecture notes in physics, Vol. 568.

Viggiani, G. and Atkinson, J.H. 1995. Interpretation of bender element tests. Géotechnique. 45(1): 149-154.

Vinegar H.J., De Waal J.A., and Wellington S.L. 1991. CT Studies of Brittle Failure in Castlegate Sandstone. International Journal of Rock Mechanics and Mining Science & Geomechanics Abstracts. 28(5): 441-448.

Yamamuro, J.A. and Lade, P.V. 1995. Strain localization in extension tests on granular materials. Journal of Engineering Mechanics. 121(7), 828-836. ASCE.

Yang, F., Chong, A.C.M., Lam, D.C.C., and Tong, P. 2002. Couple stress based strain gradient theory for elasticity. International Journal of Solids and Structures. 39: 2731-2743.

Zbib, H.M. and Aifantis, E.C. 1988. On the structure and width of shear bands. Scripta Metallurgica. 22(5): 703-708.

BIOGRAPHY

Pulpong Pongvithayapanu was born in 1975 in Kanchanaburi Province. He obtained his Bachelor degree program in civil engineering from Sirindhorn International Institute of Technology (SIIT), Thammasat University in 1999. He had worked at Italian-Thai Development public company limited for 6 months before pursuing in the Master degree program in civil engineering at SIIT, TU in 2002. During his Master study, he had gotten the SIIT partial scholarship and worked as a teaching and research assistant to the department of civil engineering. After graduated, he had become a lecturer at South-East Asia University for 5 years and then moved to Kasetsart University, Si Racha campus in 2007. In 2006, he attained the graduate school of civil engineering at Chulalongkorn University with scholarship supported by the Commission on Higher Education, Ministry of Education under Faculty Development Scholarship Program with the collaboration of AUN/SEED-Net. In May 2009 to March 2010, he had joined the Geotechnical Engineering Division, Faculty of Civil Engineering, Graduate School of Science and Engineering, Yamaguchi University, Japan, as a foreign researcher under the supervision of Professor Masayuki Hyodo.